Max-Planck-Institut
für Meteorologie

MAX-PLANCK-GESELLSCHAFT

International Max Planck Research School
on Earth System Modelling

Modeling of mineral dust in the Southern Hemisphere with focus on Antarctica for interglacial and glacial climate conditions

Natalia Sudarchikova

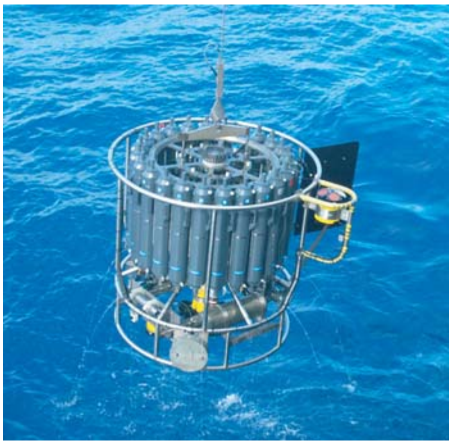

Berichte zur Erdsystemforschung

120
2012

Reports on Earth System Science

Hinweis

Die Berichte zur Erdsystemforschung werden vom Max-Planck-Institut für Meteorologie in Hamburg in unregelmäßiger Abfolge herausgegeben.

Sie enthalten wissenschaftliche und technische Beiträge, inklusive Dissertationen.

Die Beiträge geben nicht notwendigerweise die Auffassung des Instituts wieder.

Die "Berichte zur Erdsystemforschung" führen die vorherigen Reihen "Reports" und "Examensarbeiten" weiter.

Notice

The Reports on Earth System Science are published by the Max Planck Institute for Meteorology in Hamburg. They appear in irregular intervals.

They contain scientific and technical contributions, including Ph. D. theses.

The Reports do not necessarily reflect the opinion of the Institute.

The "Reports on Earth System Science" continue the former "Reports" and "Examensarbeiten" of the Max Planck Institute.

Anschrift / Address

Max-Planck-Institut für Meteorologie
Bundesstrasse 53
20146 Hamburg
Deutschland

Tel.: +49-(0)40-4 11 73-0
Fax: +49-(0)40-4 11 73-298
Web: www.mpimet.mpg.de

Layout:

Bettina Diallo, PR & Grafik

Titelfotos:
vorne:
Christian Klepp - Jochem Marotzke - Christian Klepp
hinten:
Clotilde Dubois - Christian Klepp - Katsumasa Tanaka

Berichte zur Erdsystemforschung
120
2012

Modeling of mineral dust in the Southern Hemisphere with focus on Antarctica for interglacial and glacial climate conditions

Natalia Sudarchikova

aus Tomsk, Russian Federation

Hamburg 2012

Reports on Earth System Science
120
2012

ISSN 1614-1199

Natalia Sudarchikova
Max-Planck-Institut für Meteorologie
Bundesstrasse 53
20146 Hamburg

Als Dissertation angenommen
vom Department Geowissenschaften der Universität Hamburg

auf Grund der Gutachten von
Prof. Dr. Hartmut Grassl
und
Dr. Uwe Mikolajewicz

Hamburg, den 10. Juli 2012
Prof. Dr. Jürgen Oßenbrügge
Leiter des Departments für Geowissenschaften

ISSN 1614-1199

Modeling of mineral dust in the Southern Hemisphere with focus on Antarctica for interglacial and glacial climate conditions

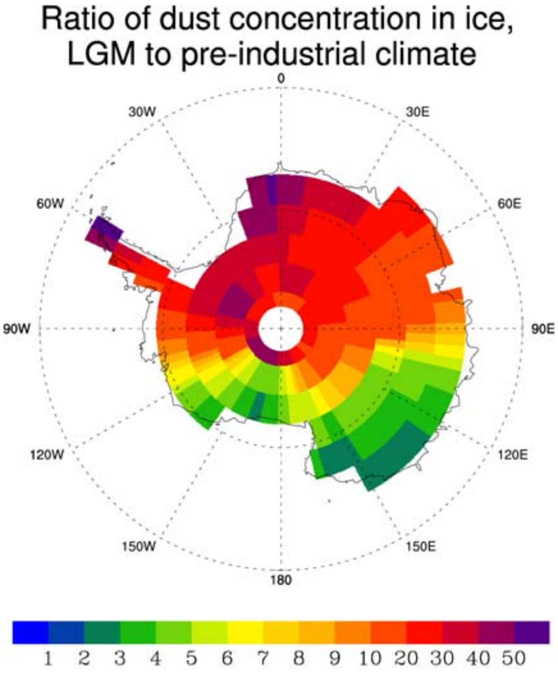

Natalia Sudarchikova

Hamburg 2012

Abstract

Mineral dust is an active aerosol component of the Earth's climate system. Dust can influence climate by changing the radiative properties of the atmosphere directly and through modifying cloud properties. Mineral dust also plays an important role in ocean uptake of carbon dioxide being a source of iron, which is an important nutrient for phytoplankton growth.

In this study, the response of the dust cycle to insolation induced climate changes is investigated. The study was carried out using the global aerosol/climate model ECHAM5-HAM. The dust cycle in the Southern Hemisphere, with a particular focus on the Antarctic region, has been analyzed for four interglacial and one glacial time-slices. The 20-year time-slices are the pre-industrial control (CTRL), mid-Holocene (6,000 years BP), Eemian (126,000 years BP), last glacial inception (115,000 years BP) and Last Glacial Maximum (LGM) (21,000 years BP) time intervals. This study is a first attempt to simulate past interglacial dust cycles.

In all past interglacial time-slices, the modeled dust deposition in Antarctica is higher than in the pre-industrial CTRL simulation. The largest increase of dust deposition in Antarctica was simulated for the LGM period.

The contribution of different processes, such as emission, transport and precipitation to the total dust deposition in Antarctica for different time-slices was analyzed. In the mid-Holocene and Eemian, two thirds of the increase in dust deposition relative to the CTRL simulation is due to enhanced Southern Hemisphere dust emissions and approximately one third is due to slightly increased transport efficiency towards Antarctica during austral spring (SON) and summer (DJF). The moderate change of dust deposition in Antarctica in the last glacial inception period is a result of slightly stronger poleward transport efficiency compared to the pre-industrial. In the LGM simulation, dust deposition over Antarctica is substantially increased due to 2.6 times higher Southern Hemisphere dust emissions, 2 times stronger transport and 30% weaker precipitation over the Southern Ocean.

The seasonal cycle of dust concentration in Antarctic ice shows a maximum during SON for the interglacial time-slices, whereas in the LGM the timing of maximal dust concentration in ice depends on the region.

Atmospheric transport towards Antarctica has similar seasonality for both interglacial and glacial time-slices, with maximal transport efficiency in JJA and minimal in DJF. Poleward atmospheric transport is more active in the LGM compared to the interglacial time-slices. In general, the seasonal timing of atmospheric transport efficiency towards Antarctica is not in phase with Southern Hemisphere dust emissions. This is valid for all considered time-slices. Synoptic scale eddy fluxes are significant for the transport of dust towards Antarctica.

Contents

Chapter 1

Introduction

Soil dust is a type of mineral aerosol, and comprises one component of the total atmospheric aerosol loading (Kohfeld and Tegen, 2007). Atmospheric dust consists of soil particles which are emitted from the ground into the atmosphere during strong surface wind events. Soil dust particles generally consist of a mixture of minerals, including, e.g. quartz, feldspars, gypsum and calcite, clay minerals rich in elements such as aluminum, and oxides and hydroxides rich in elements such as iron (Harrison et al., 2001; Kohfeld and Tegen, 2007). A compilation by Claquin et al. (1999) indicates that quartz is the most abundant mineral in the silt size fraction of the soil (particles in the size range of 2-50 μm diameter), and illite is the most abundant clay mineral (particles in the size range $< 2\ \mu m$ diameter). The mineral composition of dust changes depends on the source region. Mineralogy of emitted dust can be modified due to the decrease in grain size accompanied by differential deposition of some mineral species, with increasing distance of transport (e.g. Prospero et al., 1981; Sokolik and Toon, 1999). The chemical properties of dust can change during atmospheric transport when dust surfaces become coated with soluble sulfate and nitrate species (Kohfeld and Tegen, 2007).

Desert dust plays an important role in the climate system (Fig.1.1). Models suggest that dust is one of the main contributors to the global aerosol burden (Textor et al., 2006). For example, at present, the total dust load accounts for 60% of the aerosol dry mass (Textor et al., 2007). Dust can influence climate directly, by changing the radiative properties of the atmosphere through the scattering and absorption of incoming solar and outgoing terrestrial radiation (e.g. Sokolik et al., 2001; Tegen, 2003; Balkanski et al., 2007). Dust can either increase or decrease planetary albedo, depending on both the single scattering albedo of the dust particle as well as the albedo of the underlying surface. For example, dust over optically "dark" regions, such as oceans or forests, can have a cooling effect at the surface and warming effect in the upper atmosphere (e.g. Tegen et al., 1996; Harrison et al., 2001). On the other hand, dust can increase the absorption of solar radiation over high reflective regions such as ice sheets, snow, or even desert surfaces (Kohfeld and Tegen, 2007). Dust also can influence climate indirectly, by acting as ice nuclei (Sassen et al., 2003) and modifying cloud properties which, in turn, can impact both the radiative balance of the Earth and the hydrological cycle (Arimoto, 2001).

The deposition of desert dust to the ocean is an important source of iron in high-nutrient-low-chlorophyll regions (Mahowald et al., 2009), because crustal materials of desert dust contain 3.5% iron and about 700 ppm phosphorus (Mahowald et al., 2011). This iron contribution may be crucial for the ocean uptake of atmospheric CO_2 through its role as an important nutrient for phytoplankton growth (e.g Martin et al., 1990; Jickells et al., 2005; Wolff et al., 2006; Mahowald et al., 2008). Mineral aerosols have even been implicated as the cause of some of the 80 ppm change in carbon dioxide between glacial and interglacial time periods, due to their biogeochemical interactions (e.g., Martin, 1990; Broecker and Henderson, 1998; Watson et al., 2000). In addition, dust can act to fertilize tropical forests over long time periods (e.g. Okin et al., 2004). Mineral dust can also impact atmospheric chemistry via heterogeneous reactions and changes in photolysis rates (e.g. Dentener et al., 1996).

Thus, mineral dust can affect climate, and climate influences the mobilization and transport of dust. Such climatic parameters as aridity, vegetation cover, winds, and precipitation control the dust cycle and are changed on geological timescales, which implies the change in dust emissions, transport and deposition.

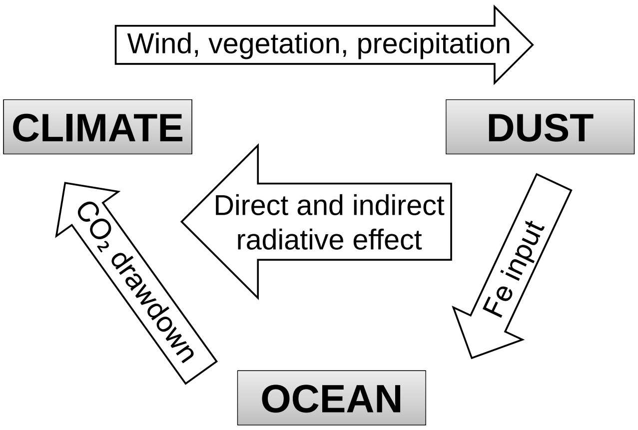

Figure 1.1— An illustration of the dust/climate interaction.

Global Quaternary records of dust suggest that different climatic periods are accompanied by a large variation in dust fluxes. A well-established data base of globally distributed dust deposition fluxes for present day and Last Glacial Maximum (LGM) climate is available from the "Dust Indicators and Records of Terrestrial and Marine Palaeoenvironments" project (DIRTMAP, Kohfeld and Harrison, 2001). The data set is based on ice core measurements, marine sediment core, marine sediment traps and terrestrial loess accumulation records. Polar ice cores represent the only direct archive for the deposition of aeolian dust particles in the past, with mineral dust being transported over long-distances from desert regions to the polar ice sheets. While the total dust deposition is a first order measure of dust mobilization, and therefore also for climate conditions in the dust source regions, particle size distributions allow for a quantification of transport efficiency. Ice core records from Greenland and Antarctica, spanning several climatic cycles, show that aeolian deposition rates at high latitudes were 2-20 times larger during glacial than interglacial periods (e.g. Petit et al., 1990, 1999; EPICA Community Members, 2006; Lambert et al., 2008). Marine sediment records suggest 3-4 times higher dust deposition globally during glacial times compared to interglacial periods, though the increase in atmospheric dust loading was not spatially uniform (Rea, 1994).

The large changes in dust emissions and transport seen from the paleo-dust record may reflect a variety of processes (according to Kohfeld and Harrison, 2001; Maher et al., 2010):

a) changes in the areal extent of source regions, erosion of exposed continental shelves, deflation from periglacial deposits;

b) changes in wind speed and gustiness over source regions or atmospheric transport of dust;

c) changes in the residence time of dust in the atmosphere, and/or variations in the relative contributions of dry settling or rainout of dust over a given region;

d) altered wind patterns linking sources to the deposition areas.

Similarly, changes in mineralogy could reflect:

(a) changes in the source region;

(b) shifts in atmospheric transport from the source regions to the dust deposition site;

(c) changes in the mineralogical composition of the source region resulting from changes in weathering.

Through the study of paleoclimate, we can identify mechanisms by which different parts of the climate system, one of which is mineral dust, respond to insolation-induced climate changes. Better understanding of paleoclimatic changes is a necessary condition for more reliable forecast projections of possible future scenarios of the climate change. Most paleorecords of dust properties provide only patchy and discrete information both in time and space. This patchiness complicates any global assessment of the spatial and temporal variability in the emissions, the atmospheric burden, transport, and deposition of dust. One way to examine the relative contributions of the possible factors contributing to past changes in dust deposition is to use a forward modeling approach, in which process-based models can be used to predict the response of the dust cycle to simulated climate changes.

Simulations of the dust cycle of past time-slices can give additional insight into past climates, and they also represent a critical test for the models, since these simulations can be validated against independent paleo data. One additional aspect is that the simulation of the marine carbon cycle of past time-slices requires adequate dust deposition values as input.

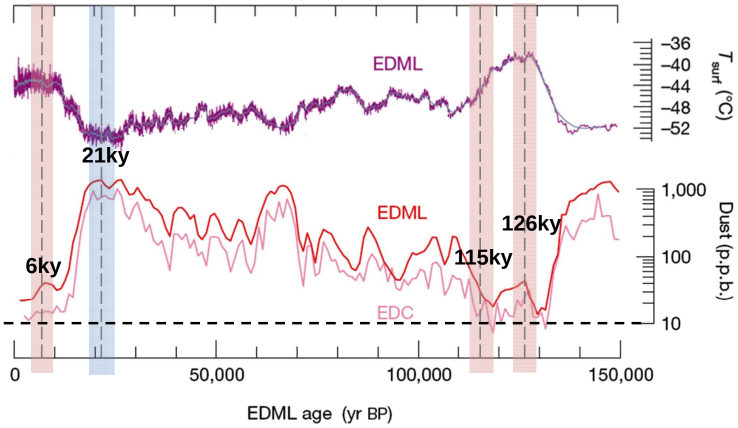

Figure 1.2— Mineral dust records in Antarctic ice cores (EPICA Community Members, 2006). EDML - EPICA Dronning Maud Land (75S, 004E); EDC - EPICA Dome C (75S, 123E).

To account for the impact of different orbital parameters and other boundary conditions on mechanisms responsible for the change in the dust cycle, four interglacial time-slices as well as one glacial period were studied (Fig.1.2). The interglacial time-slices are the mid-Holocene (6,000 years BP), the last glacial inception (115,000 years BP) and the Eemian (126,000 years BP). Glacial time interval is the Last Glacial Maximum (LGM) (21,000 years BP). The current interglacial is called the Holocene which started about 11.6 kyr ago. The Eemian is an interglacial period which lasted from 130 ± 1 to 116 ± 1 kyr BP. The dust cycle during the interglacial time intervals (except for present day) has not been the subject of many studies. Thus, no broad precompiled data sets of dust deposition exist. The only model study I know of is a transient EMIC simulation (Bauer and Ganopolski, 2010), where the role of aeolian dust for the evolution of the past four glacial cycles was analyzed. For the LGM however, a good precompiled data set of dust deposition exists (DIRTMAP, Kohfeld and Harrison, 2001) and this time-slice has been simulated in several other studies (e.g. Werner et al., 2002; Mahowald et al., 2006; Li et al., 2010). This study is a first attempt to predict past interglacial dust cycles.

The main changes in climate forcing between different paleo runs (apart from greenhouse gas concentrations and topography changes in the LGM) are the changes in orbital parameters of the Earth, calculated after Berger (1978). Orbital parameters influence the total, spatial, and temporal distribution of incoming solar radiation. These parameters are the eccentricity, the obliquity and longitude of perihelion. The orbital parameters vary on periods of approximately 19 kyr and 23 kyr for the precession of the vernal equinox, 41 kyr for the obliquity and 100 kyr for the eccentricity. The orbital cycles were named Milankovich cycles, after a Serbian mathematician, Milutin Milankovitch, who explained how these orbital cycles cause the advance and retreat of the polar ice caps. However, the first scientists to link orbital cycles to climate were Adhemar (1842) and Croll (1875). In the mid-Holocene and Eemian perihelion occurs in September and July respectively instead of January as it is in the current climate and obliquity is enhanced. Increased insolation in boreal summer leads to an increase of seasonality in the Northern Hemisphere, while it is reduced in the Southern Hemisphere. During the Eemian the eccentricity of the Earth's orbit around the sun was larger than in the mid-Holocene which leads to more pronounced insolation change in the Eemian. Eemian and mid-Holocene temperatures are higher at high latitudes and colder at low latitudes, compared to pre-industrial climate. The African summer monsoons are more intense.

The most recent glacial period started about 115 kyr BP, in response to orbital forcing. Reduced summer insolation at the high latitudes in the Northern Hemisphere, enables winter snow to persist all year and to accumulate, resulting in the build up of the Northern Hemisphere ice sheets.

The LGM is characterized by a colder and drier climate conditions. The LGM dust cycle was analyzed in several previous modeling studies.

Werner et al. (2002) reported that one third of the simulated increase in the total global dust emission flux at the LGM is related to source-region changes, while two thirds are caused by global wind speed changes over modern dust emission regions. They simulated a 2.2-fold increase in dust emission flux in the LGM compared to the present. In the study of Mahowald et al. (1999), a change in vegetation and an increase in dust source areas are an important factors in determining the observed large increases in dust deposition in polar regions. They simulated an increase by a factor of 3 in the total dust emissions for the LGM. They suggested increased LGM dust deposition in Antarctica by a factor of 2-10 and Patagonia as a major source of dust in Antarctica, consistent with observations. Mahowald et al. (2006) also showed that dust emissions in the LGM respond strongly to vegetation changes. They simulated a 2.2-fold increase in dust emission flux for the LGM. In an additional simulation, which includes glaciogenic dust sources in the LGM, dust emissions increased from 2.2 to 3.3 times the current climate. Thus, in the LGM approximately one third of the dust originated from glaciogenic sources. Albani et al. (2011) suggested that South America is the dominant source for dust deposited in Antarctica in the LGM. They showed a more marked transport pathway with a dust plume connecting Patagonia to the Antarctic Continent/Western Antarctica, characterized by a southward displacement of air masses. In the study of Li et al. (2010), source expansion due to the reduction in the continental vegetation and lowering of the sea level, contributes to most of the increase of dust transported to Antarctica during the LGM. The lowering of the sea level exposed large areas of continental shelves for dust mobilization, and this turned out to be more important than the reduction in the continental vegetation.

In the current study state-of-the art global atmosphere-aerosol model ECHAM5-HAM was used in order to investigate the dust cycle in the Southern Hemisphere with a particular focus on the Antarctic region. The quantitative contribution of different processes such as emission, transport and precipitation on dust deposition in Antarctica in different climate conditions was analyzed.

The main questions addressed in this work are:

- How do mineral dust emissions change in different climate conditions?
- Which processes are responsible for the changes of Southern Hemisphere dust emissions?
- How does dust deposition over Antarctica changes in the different time-slices?
- What is the contribution of different processes, such as emission, transport and precipitation to dust deposition in Antarctica in the different time-slices?
- How does atmospheric transport towards Antarctica changes in the different time-slices?
- How does synoptic scale eddy fluxes influence transport of dust to Antarctica in different time-slices?
- Altitude of atmospheric transport of dust towards Antarctica in interglacial and glacial time-slices.
- What are the dust source regions for dust deposition in Antarctica in different time-slices?
- Does seasonality of dust concentration in the Antarctic ice changes in different time-slices?
- How well can the model simulate the dust cycle in different climate conditions?

This study has focused on dust transport from the Southern Hemisphere dust sources to the Antarctic continent. To this end, an analysis method has been developed that describes dust emission in the Southern Hemisphere, its poleward transport, loss due to precipitation over the ocean south of 40°S and final deposition in Antarctica. The transport parameter has been derived in terms of the frequency of air mass transport trajectories originating in the free troposphere over the Southern Hemisphere dust sources at 800 hPa and 500 hPa and reaching Antarctica. Using this method, seasonal variations of dust deposition between time-slices as well as differences between time-slices, can be qualitatively explained.

This thesis is organized as follows: In Chapter 2 a short description of aerosol-climate model ECHAM5-HAM is presented. In Chapter 3 the simulation of the dust cycle for the pre-industrial climate conditions is analyzed. The influence of different orbital parameters on the dust cycle are analyzed in Chapter 4 with the example of three past interglacial time-slices, which are the mid-Holocene, the Eemian and the last glacial inception. The interglacial time-slices are followed by one glacial time-slice, which is the LGM, as a reference simulation to check the model performance because aeolian deposition rates for the LGM are known with some confidence. The model validation and discussion are the subjects of Chapters 5 and 6. Chapter 7 concludes the main findings and gives an outlook to future research.

Chapter 2

Model description

2.1 The ECHAM5-HAM global climate aerosol model

For the current study the Atmospheric General Circulation Model (AGCM) ECHAM5-HAM is used. The climate model ECHAM5 is the fifth generation model developed from the spectral weather prediction model of European Center for Medium Range Weather Forecasts (ECMWF) at the Max Planck Institute for Meteorology, Hamburg (Roeckner et al., 2003).

The ECHAM5 model consists of a spectral dynamical core based on the primitive equations and a comprehensive set of physical parameterizations. The prognostic variables are temperature, vorticity, divergence, logarithm of the surface pressure, and the mass mixing ratios of water vapor, cloud liquid water and cloud ice. Temperature, vorticity, divergence and logarithm of the surface pressure are represented in the horizontal by a truncated series of spherical harmonics. The water vapor, cloud liquid water, cloud ice and optianal trace components are transported using a flux form semi-Lagrangian transport scheme (Lin and Rood, 1996) on a Gaussian grid. The physical parameterizations within the ECHAM5 model are formulated in grid point space as well. They include long-wave radiation, shortwave radiation, gravity wave drag, the planetary boundary layer, cumulus convection, stratiform cloud formation, precipitation formation, land-surface processes, etc.

The ECHAM5 model has been extended to the global climate aerosol model ECHAM5-HAM by development of an aerosol module HAM by Stier et al. (2005), allowing long-term, centennial to millennial scale, depending on the model resolution, transient climate simulations to increase the understanding of the role of aerosols in the climate system. The aerosol populations in HAM are described as superposition of seven modes with log-normal size distribution. For each mode, the aerosol size-distribution, composition, mass and number concentration are prognostic variables. The size distribution is characterized by the three moments: aerosol number, median radius and the standard deviation. According to the dry particle diameter the seven modes are divided into four size classes: $0.001 - 0.01\mu m$ - nucleation mode, $0.01 - 0.1\mu m$ - Aitken mode, $0.1 - 1\mu m$ - accumulation mode and $> 1\mu m$ - coarse mode. Four of the seven modes are termed 'soluble', which means, in the context of this model, that the mode may take up water. Soluble modes are regarded as internal mixture of insoluble and soluble compounds, and cover all size classes. Insoluble modes do not take up water, are regarded as external mixture of compounds with no or low water-solubility and cover Aitken, accumulation and coarse modes. The modelled aerosol species are sulfate, black carbon, organic carbon, sea salt and mineral dust. Mineral dust covers accumulation and coarse modes (both soluble and insoluble). The emissions of dust, sea salt and oceanic dimethyl sulfide (DMS) are calculated online. Terrestrial biogenic DMS emissions are prescribed. For all other compounds, emission strength, distribution, and height are based on the AEROCOM emission inventory for the aerosol model inter-comparison experiment B representative for the year 2000 (Dentener et al., 2006).

In the current study the model resolution T31L19 is used. Horizontal resolution T31 means triangular truncation of spherical harmonics series at wave number 31 ($\backsim 3.75^\circ \times 3.75^\circ$ spatial resolution on a latitude-longitude grid). In the vertical, the atmosphere is divided into 19 hybrid sigma-pressure levels (L19) reaching up to the pressure level of 10 hPa. The prognostic model equations are solved using a leapfrog time integration scheme with a time-step of 40 minutes. Below a synopsis of the main model features related to the current study is given.

2.2 Dust emissions

For the emission of mineral dust, two optional schemes have been implemented into HAM: the scheme of Tegen et al. (2002) and the scheme of Balkanski et al. (2004). In this study the scheme of Tegen et al. (2002) is used. The scheme is coupled online, i.e. it calculates the emission of mineral dust depending on the ECHAM5 wind speed and hydrological parameters. Freshly emitted dust is assumed insoluble. Tegen et al. (2002) derived preferential dust source areas from an explicit simulation of paleological lakes (see details in section 2.2.5). In addition, lower dust emissions can occur in other non-vegetated regions. The emission flux is then calculated from 192 internal dust size-classes and the explicit formulation of the saltation process folowing Marticorena and Bergametti (1995). For the implementation of the Tegen et al. (2002) scheme into ECHAM5-HAM, Stier et al. (2005) fitted a multi-annual global mean of the emission size classes grouped into 24 bins with a superposition of three log-normal size-distributions. Considering the short life-time and the negligible contribution of the super-coarse mode to the radiative effect, they neglect the super-coarse mode emissions and separate the dust emission into the insoluble accumulation and coarse modes with mass-median radii of 0.37 μm and 1.75 μm and standard deviations of 1.59 and 2.00, respectively.

2.2.1 Physical approach

This section is followed by Marticorena and Bergametti (1995). Dust production in arid zones is connected to aeolian transport of soil grains. The particle motion initiated by wind is controlled by the forces acting on them. For a particle at rest, these forces are the weight, the interparticle cohesion forces, and the wind shear stress on the surface. The first two are size dependent; the last one depends on the transfer of the wind energy to the erodible surface, which is controlled by the presence of roughness elements on the surface. All together determine the minimum threshold friction velocity, U_t^*, required to initiate particle motion (the friction velocity being defined as the square root of the ratio of surface stress to air density).

Once the particle is in motion, its path depends on the budget between its weight acting downward and the opposing aerodynamic drag.

The particles with size below 60 μm, or desert dust, are small enough to be transported upward by turbulent eddies, sometimes very far from the sources. This movement is called *"suspension"*.

Soil grains in the range of 60 to 2000 μm can be lifted from the surface at a height of some tens of centimeters; but as the drag is not sufficient to exceed the weight, they are carried downwind back to the surface. Such trajectories define a motion called *"saltation"*. The maximum height of the saltation layer is of the order of 1 m.

The total amount of material in movement is located near the surface in the saltation layer. It is represented by the vertically integrated horizontal flux G. The fine suspended particles constitute the dust flux, which is referred to as the vertical flux F. The vertical flux is generally estimated from the horizontal flux.

2.2.2 Parameterization of the threshold friction velocity

Marticorena and Bergametti (1995) associate the appropriate threshold wind friction velocity U_t^* to each soil grain size. They found an approximate semi-empirical expression of the threshold friction velocity U_t^* as a function only of the particle diameter D_p. Terrestrial conditions with air density $\rho_a = 0.00123\ gcm^{-3}$ and particle density $\rho_p = 2.65\ gcm^{-3}$ were assumed. The relation of the friction Reynolds number B to the particle diameter D_p in the folowing form was used:

$$B = aD_p^x + b, \tag{2.1}$$

with a = 1331, b = 0.38, and x = 1.56.

The threshold friction velocity for
$0.03 < B < 10$ is

$$U_t^*(D_p) = \frac{0.129K}{\left(1.928(aD_p^x + b)^{0.092} - 1\right)^{0.5}} \tag{2.2}$$

where

$$K = \left(\frac{\rho_p g D_p}{\rho_a}\right)^{0.5}\left(1 + \frac{0.006}{\rho_p g D_p^{2.5}}\right), \tag{2.3}$$

for B > 10,

$$U_t^*(D_p) = 0.129K\left[1 - 0.0858exp(-0.0617((aD_p^x + b) - 10))\right] \tag{2.4}$$

In HAM, application of a scaling factor to the threshold friction velocity has been found to be necessary in order to obtain reasonable dust emissions. In this study, after several numerical experiments, the value of the scaling factor has been changed from 0.79 to 0.86 providing better results for T31 resolution with the new vegetation map.

2.2.3 Parameterization of horizontal flux

The horizontal flux depends on the wind friction velocity and on the size of the soil particles. Following Marticorena and Bergametti (1995), the relative contribution of each size range to the total horizontal flux is assumed to be proportional to the basal surface area of that range as a fraction of the total basal particle surface area. They assume that the dust-emitting soil type can be characterised as the sum of a set of lognormal size distributions. In HAM, for each soil type, we use a set of four lognormal modes, and for each we prescribe (i) the mass fraction (ii) the median particle diameter (iii) the geometric standard deviation.

Tegen et al. (2002) give the horizontal flux as:

$$G = \frac{\rho_a}{g}(U^*)^3 \cdot \sum_i \left[\left(1 + \frac{U_t^*(Dp_i)}{U^*}\right)\left(1 - \frac{(U_t^*(Dp_i))^2}{(U^*)^2}\right) \cdot s_i\right] \, for\, U^* \geq U_t^*, \tag{2.5}$$

where ρ_a $(kg\, m^{-3})$ is the air density, g $(m\, s^{-2})$ is the gravitational constant, U^* $(m\, s^{-1})$ is the surface wind stress, U_t^* $(m\, s^{-1})$ is the threshold friction velocity (as a function of mean diameter Dp_i), and s_i is the relative surface area covered by each size fraction i.

2.2.4 Parameterization of vertical flux

The dust flux, also called vertical flux, is composed of the finest particles in suspension from the saltation layer which can be transported long-range. It represents the mass of fine particles passing through a horizontal unit area per unit time. The suspension-saltation boundary is controlled by the ratio of the threshold friction velocity and the terminal velocity of the particles. The terminal velocity is defined by the equilibrium of the particle weight and the wind drag and so depends on the particle diameter and density. The value of the particle diameter for saltation-suspension boundary is about 50-60 μm (Greeley and Iversen, 1985; Marticorena and Bergametti, 1995). Moreover, particles with a diameter lower than this limit involve very high threshold friction velocities due to the strong cohesion forces linking them to each other. Thus the movement of these fine particles is not initiated directly by the wind friction on the erodible surface and requires sandblasting or bombardment processes to disrupt the aggregates and produce dust particles that will be set in suspension (e.g. Shao et al., 1993). Since dust production requires saltation as an intermediate process, the vertical flux (F) is generally derived from the horizontal flux (G).

The vertical dust particle flux F is predicted as follows Tegen et al. (2002):

$$F = \alpha \cdot A_{eff} \cdot G \cdot (1 - A_{snow}) \cdot I_0, \tag{2.6}$$

where A_{eff} is effective surface for dust emissions, A_{snow} is snow covered area, $A_{snow} = min[1, (C/0.015\,m)]$, where C is snow depth (in meters); I_0 is 0 when upper-layer soil moisture is at field capacity and 1 otherwise; A_{eff} depends on the vegetation cover and is presented in more detail in section 2.2.6.

2.2.5 Preferential dust source areas

Originally, Tegen et al. (2002) derived preferential dust source areas from an explicit simulation of the extent of paleolake beds across the globe. They specified the extent of these lakes using a high-resolution water routing and storage model, HYDRA (Coe, 1998). The difference between the simulated maximum areas of lakes and the actual present-day areas of lakes is assumed to indicate the extent of paleolake deposits formed under wetter climate conditions at some time in the recent geological past. These exposed paleolake areas are then used as preferential source areas for dust emission, provided they meet the additional criterion for dust deflation imposed by vegetation, soil moisture conditions, and wind strength.

In this study another method, which is described in Ginoux et al. (2001) is used. The origin of clay minerals at the Earth's surface is, in the majority of cases, a process of weathering of rocks to form alluvium (stream deposited sediments) (Velde, 1992). Because there are no data on the global distribution of alluvium over the land surface, the potential location of accumulated sediments has been determined by comparing the elevation of any 1°×1° grid point with its surrounding hydrological basin (Ginoux et al., 2001). The complex contours of each basin have been simplified by assuming a constant area of 10° × 10°, based on the fact that most hydrological basin have a size of roughly 10° in the arid regions.

Ginoux et al. (2001) assume that a basin with pronounced topographic variations contains large amounts of sediments which are accumulated essentially in the valleys and depressions, and over a relatively flat basin the amount of alluvium is homogeneously distributed. They introduce a source function S, which is the fraction of alluvium available for wind erosion, as follows:

$$S = \left(\frac{z_{max} - z_i}{z_{max} - z_{min}} \right)^5, \tag{2.7}$$

where S is the probability to have accumulated sediments in the grid cell i of altitude z_i, and z_{max} and z_{min} are the maximum and minimum elevations in the surrounding 10° × 10° topography, respectively. It is not intended to calculate the exact amount of alluvium but rather to define the most probable locations of sediment. To increase the topographic contrast of these locations and to obtain the best fit with the sources identified by Prospero et al. (2000), the relative altitude has been taken at the fifth power. Only land surface with bare soil is considered as possible dust sources. We identify the bare soil surface from the vegetation data set derived by using the dynamical vegetation model LPJ (Smith et al., 2001).

2.2.6 Vegetation type and cover

In the current study, the method to determine potential dust sources is based on the aproach presented in Tegen et al. (2002) with some modifications.

The effective surface A_{eff} for dust emission is calculated as

$$A_{eff} = 1 - (FPAR(max_{ann}) \cdot f_{shrub} + FPAR(max_{ann} \cdot f_{grass}) \cdot \frac{1}{0.25}, \tag{2.8}$$

where f_{shrub} and f_{grass} are the relative contribution for coverage with shrub or grass vegetation for each biome type (here f_{shrub} is 1 for shrub-dominated vegetation and f_{grass} is 1 for grass-dominated biomes; for other biome types fshrub and fgrass are 0). The factor 1/0.25 is the slope in the linear relationship between dust emission and (fraction of absorbed photosynthetically active radiation) FPAR, when assuming a limit of FPAR = 0.25 for dust emissions and assuming a linear relationship between the fraction of unvegetated area per gridcell and dust emission.

The dust source area is 0 when the annual maximum fraction of absorbed photosynthetically active radiation (FPAR) is > 0.25 and increases linearly to a maximum at FPAR = 0. Tegen et al. (2002) derived FPAR from monthly retrievals of the normalized difference vegetation index (NDVI) from the advanced very high resolution radiometer (AVHRR) satellite instrument (Braswell et al., 1997) (available for the years 1982 to 1993 at 0.5 ° horizontal resolution) using the empirical relationship FPAR = $1.222 \cdot (NDVI/0.559 - 0.1566)$ (Knorr and Heimann, 1995). Negative values are set to zero.

Since we investigate paleo climate and there are no FPAR data available we assume that FPAR is equal to vegetation ratio. Thus, the potential dust sources are defined as regions with annual maximum vegetation cover fraction less than or equal to 25%. Vegetation information was obtained from the dynamical vegetation model LPJ. We also use maximum of vegetation cover as factor for both shrub- and grass-dominated vegetation in order to compensate for a slight underestimation of vegetation cover fraction by the LPJ model and assuming that even in autumn and winter time, when grass is dring up the roots still suppress the emission of soil particles. In Tegen et al. (2002), for grass-dominated biomes, the monthly mean FPAR values were used.

2.3 Tracer advection

The flux form semi-Lagrangian scheme employed in ECHAM5 for passive tracer transport has been introduced by Lin and Rood (1996). This type of advection scheme combines typical features of Eulerian flux form schemes (i.e. exact mass conservation to machine precision) with the unconditional stability for all Courant numbers typical for standard (non-conservative) semi-Lagrangian schemes (Roeckner et al., 2003). For Courant numbers smaller than one, the Lin-Rood schemes reverts to a multidimensional flux form scheme which takes properly into account transverse fluxes, such as those developed by Colella, LeVeque, Leonard and others (for references see Lin and Rood, 1996).

The Lin and Rood scheme satisfies some fundamental requirements for a tracer advection algorithm (Roeckner et al., 2003):

- mass conservation: by construction, since it is formulated in flux form;
- consistency with the discretization of the continuity equation;
- monotonicity of the 1D advection schemes;
- preservation of linear tracer correlations.

2.4 Sink processes

2.4.1 Dry deposition

The net surface fluxes, calculated by subtracting the dry deposition fluxes from the respective emission fluxes, provide the lower boundary conditions for the implicit vertical diffusion scheme of ECHAM5. The dry deposition flux F_d is calculated as the product of the surface layer concentration and the dry deposition velocity v_d:

$$F_d = C\rho_a v_d, \tag{2.9}$$

where C is the tracer mass or number mixing ratio and ρ_a is the air density. The dry deposition velocities are calculated based on a serial resistance approach. For gases, v_d is calculated from the aerodynamic, quasi-laminar boundary layer, and surface resistance according to the “big leaf ”concept (Ganzeveld and Lelieveld, 1995; Ganzeveld et al., 1998) for the ECHAM5 fractional surface cover types (snow/ice, bare soil, vegetation, wet skin, water and sea ice) of each grid box. The surface resistances are generally prescribed except for some specific resistances, e.g. the SO_2 soil resistance as a function of soil pH, relative humidity, surface temperature, and the canopy resistance. The latter is calculated from ECHAM5’s stomatal resistance and a monthly mean Leaf Area Index (LAI), in our case obtained from the dynamical vegetation model LPJ.

For aerosols Stier et al. (2005) have implemented the dry deposition velocity model that has previously been applied to develop a sulfate aerosol dry deposition parameterisation (Ganzeveld et al., 1998). In contrast to using prescribed sulfate mass size distributions, which were used to develop the sulfate aerosol dry deposition parameterisation, HAM uses the explicitly calculated modal number and mass parameters to calculate the aerosol dry deposition velocity as a function of particle radius, density, turbulence, and surface cover properties. The dry deposition model calculates the bare soil and snow/ice aerosol dry deposition velocities according to Slinn (1976), over water according to Slinn and Slinn (1980), whereas the vegetation and wet skin aerosol dry deposition velocities are calculated according to Slinn (1982) and Gallagher et al. (2002). Over water, the effect of whitecaps in enhancing aerosol dry deposition according to Hummelshoj et al. (1992) is taken into account.

2.4.2 Sedimentation

Sedimentation of the aerosol particles is calculated throughout the atmospheric column. The calculation of the sedimentation velocity is based on the Stokes velocity:

$$v_s = \frac{2}{9}\frac{r^2 \rho g C_c}{\mu} \tag{2.10}$$

with the Cunningham slip-flow correction factor C_c accounting for non-continuum effects (e.g. Seinfeld and Pandis, 1998):

$$C_c = 1 + \frac{\lambda}{r}[1.257 + 0.4exp - \frac{1.1r}{\lambda}] \tag{2.11}$$

Here v_s is the sedimentation velocity, r is the number or mass median radius, ρ is the particle density, g is the gravitational acceleration, μ is the gas viscosity, and λ is the mean free path of air. To satisfy the Courant-Friedrich-Lewy stability criterion, the sedimentation velocity is limited to $v_s < \frac{\Delta z}{\Delta t}$, where Δz is the layer thickness and Δt is the model timestep.

2.4.3 Wet deposition

The fraction of scavenged tracers is calculated from the in-cloud content utilising the precipitation formation rate of the ECHAM5 cloud scheme (Stier et al., 2005). For gases, the partitioning between the air and the cloud water is calculated based on Henrys law (e.g. Seinfeld and Pandis, 1998) whilst for aerosols it is prescribed in the form of a size- and composition-dependent scavenging parameter R. R is defined as the fraction of the tracer in the cloudy part of the grid box that is embedded in the cloud liquid/ice water. Values of R for stratiform clouds follow measurements of interstitial and in-cloud aerosol contents of Henning et al.(2004), with slight modifications, and for ice clouds are based on Feichter et al.(2004). Assuming higher supersaturations and therefore activation into lower size-ranges, Stier et al. (2005) increase R in convective clouds for the soluble modes, which they assume to be potential cloud condensation nuclei. The prescribed values of R are lower for ice clouds than for liquid and mixed clouds (see details in Stier et al., 2005). For the scavenging by stratiform clouds, the local rate of change of tracer i is calculated as:

$$\frac{\Delta C_i}{\Delta t} = \frac{R_i C_i f^{cl}}{C_{wat}} \left(\frac{Q^{liq}}{f^{liq}} + \frac{Q^{ice}}{f^{ice}}\right), \tag{2.12}$$

where C_i , C_{wat} are mixing ratios of the tracer i and total cloud water, respectively. f^{cl} is the cloud fraction, f^{liq} and f^{ice} are the liquid- and ice fraction of the cloud water. Q^{liq} and Q^{ice} are the respective sum of conversion rates of cloud liquid water and cloud ice to precipitation, via the processes auto-conversion, aggregation, and accretion.

Convective scavenging is coupled with the mass flux scheme of the convective tracer transport. In addition to the local change of the tracer tendency, the convective tracer fluxes have to be adjusted by the wet deposition. In convective updrafts the tracer mixing ratios are associated with the liquid- and ice-phase proportionally to the presence of the respective phase:

$$C_i^{liq} = C_i f^{liq} \qquad C_i^{ice} = C_i f^{ice} \tag{2.13}$$

The change in tracer mixing ratio is calculated as

$$\Delta C_i = \Delta C_i^{liq} + \Delta C_i^{ice} = C_i^{liq} R_i E^{liq} + C_i^{ice} R_i E^{ice} \tag{2.14}$$

where R_i is the scavenging parameter and E^{liq} and E^{ice} are the fractions of updraft liquid water and updraft ice water that are converted into precipitation during one timestep.

From the local ΔC_i for each layer k the local grid-box mean deposition flux $\overline{F_i^{dep}}$ and the grid-box mean tendency $\overline{\frac{\Delta C_i}{\Delta t}}$ are calculated:

$$\overline{F_i^{dep}} = \Delta C_i \overline{F^{up}} \qquad \overline{\frac{\Delta C_i}{\Delta t}} = \overline{F_i^{dep} \frac{g}{\Delta p}} \tag{2.15}$$

Here $\overline{F^{up}}$ is the grid-box mean updraft mass flux. The local deposition flux is integrated from the model top to the respective layer k:

$$\overline{F_i^{dep}}^{int} = \sum_{top}^{k} \overline{F_i^{dep}} \tag{2.16}$$

The mean updraft tracer flux $\overline{F_i^{up}}$ for tracer i is recalculated based on the updated updraft tracer mixing ratios:

$$\overline{F_i^{up}} = (C_i - \Delta C_i)\overline{F^{up}} \tag{2.17}$$

A non-negligible fraction of precipitation re-evaporates before it reaches the ground. Re-evaporation acts on the integrated tracer deposition flux $\overline{F_i^{dep}}^{int}$ proportionally to the evaporation of precipitation:

$$\Delta \overline{F_i^{dep}}^{int} = \overline{F_i^{dep}}^{int} f^{evap} \tag{2.18}$$

$$\frac{\overline{\Delta C_i}}{\Delta t} = \Delta \overline{F_i^{dep}}^{int} \frac{g}{\Delta p} \tag{2.19}$$

where f^{evap} is the evaporating fraction of precipitation, Δp is the layer thickness in pressure units, and g is the gravitational acceleration.

For aerosols, below-cloud scavenging is calculated from the ECHAM5 water- and ice- precipitation fluxes with prescribed size-dependent collection efficiencies R_i^r and R_i^s from Seinfeld and Pandis (1998) for rain and snow, normalised by the respective precipitation rate

$$\frac{\overline{\Delta C_i}}{\Delta t} = C_i^{amb} f^{precip} (R_i^r F^r + R_i^s F^s) \tag{2.20}$$

where C_i^{amb} is the mass mixing ratio of the ambient cloud free air, f^{precip} is the effective grid-box fraction affected by precipitation, and F^r and F^s are the fluxes of rain and snow, respectively. f^{precip} is estimated in the stratiform scheme by the assumption of maximum overlap of the cloudy parts of the grid box and for the convective scheme from the estimated updraft area.

Changes in wet deposition scheme as described in Stier et al. (2005) have been introduced following Verheggen et al. (2007). They investigated the response of the activated fraction to temperature and/or ice fraction in order to evaluate the effect of ice and liquid phases coexisting.

The activated fraction of aerosol particles (F_i) decreases with increasing cloud ice mass fraction and with decreasing temperature from 0 to −25°C. This is consistent with the Wegener-Bergeron-Findeisen (WBF) process taking place in natural mixed-phase clouds: liquid droplets evaporate in the presence of ice crystals, because of the lower vapor pressure over ice, which leads to an evaporation of liquid droplets. This in turn leads to a decrease in activated fraction, since the number of ice crystals is much less than the number of liquid droplets had been before their evaporation. The presence of ice coulds also prevents more particles from activating, because the lower vapor pressure over ice preferentially drives the water vapor to the ice phase. This is indistinguishable from the WBF process and also leads to a lower activated fraction. Additional reasons for the low activated fraction at low temperature may be the low water vapor concentration, which causes the supersaturation to decrease faster.

We scale scavenging parameter for the mixed phase clouds parameterization according to Verheggen et al. (2007):

$$F_i(D_p > 100nm) = 0.031 + 0.93/(1 + exp(-(T + 3.64)/3.42)), \tag{2.21}$$

where T is temperature in °C.

Chapter 3

Pre-industrial control simulation

3.1 Experimental setup

In order to investigate the natural variability of mineral dust, simulations for different modeled paleo climate conditions need to be compared with simulations for the non-anthropogenic pre-industrial climate. To make such comparison consistent, the input information for all the experiments has to be obtained in a similar way. One of the main input drivers for dust modeling is vegetation cover. A 20-year pre-industrial climate control simulation with modeled vegetation after 5 years of spin up was performed. Hereafter the abbreviation ”CTRL” is used for this simulation. In order to analyse how well the modeled pre-industrial vegetation cover captures the main arid regions, a second simulation for the pre-industrial conditions with vegetation derived from satellite observations was performed and named ”PreVeg”. The main results from the PreVeg simulation and the differences with the CTRL run are discussed in section 3.3.

Following the Paleoclimate Modelling Intercomparison Project (PMIP2) protocol ($http : //pmip2.lsce.ipsl.fr/$, Braconnot et al., 2007), orbital parameters and greenhouse gas concentrations were prescribed with the pre-industrial values (eccentricity 0.016724, obliquity 23.446, longitude of perihelion 282.04, CO_2 280 ppm, CH_4 0.76 ppm, N_2O 0.27 ppm). Topography, sea level and continental ice-sheets were assumed to be similar to the present state.

Sea surface temperature (SST), sea ice concentration and surface background albedo were obtained from the long-term simulation with the coupled atmosphere ocean dynamical vegetation model ECHAM5/MPIOM/LPJ. Sea surface temperatures were corrected for the systematic error of the coupled run by adding the SST differences between observed and simulated SSTs for the pre-industrial (similar to Arpe et al., 2010). SST varies monthly and there is no change from year to year.

Vegetation information was obtained from the dynamical vegetation model LPJ (Guy Schurgers, personal communication, 2009). This model was driven with monthly mean temperature, precipitation and shortwave radiation data derived from the coupled atmosphere ocean dynamical vegetation model ECHAM5/MPIOM/LPJ for the pre-industrial climate. The maximum annual vegetation cover fraction was used instead of the monthly mean values (Fig.3.1) in order to compensate for a slight underestimation of the vegetation cover fraction by the LPJ model and assuming that dry plant roots and leaves protect the soil particles from mobilization in cold or dry seasons. Thus, the effect of seasonal changes in vegetation on dust emissions was not considered. Dust source areas were defined as grid boxes where vegetation cover is less than or equal to 25% (Tegen et al., 2002). Soil type information was prescribed according to present values. Other important parameters that influence dust mobilization, such as wind speed, soil moisture and snow cover, were calculated on-line.

Emissions of certain aerosol and precursor gases were prescribed according to the pre-industrial values based on the Aerosol Comparisons between Observations and Models project (AeroCom) (Dentener et al., 2006). Those are anthropogenic emissions, which consider contributions by sulfur, mainly in the form of sulfur dioxide (SO_2), particulate organic matter (POM) and black carbon (BC) from large scale wildfires (partly natural), bio fuel burning and fossil fuel burning. For the pre-industrial interval, contributions from wildfires and biofuel emissions are reduced by scaling back according to changes in population, crop production and wood consumption; fossil fuel emissions are zero (Dentener et al., 2006). Sea salt emissions are calculated on-line. These other aerosol species mix with dust particles, which affects the dust life cycle (Stier et al., 2006)

3.2 Simulation of the dust cycle for pre-industrial climate conditions with modeled vegetation

3.2.1 Global dust budget

The 20-year mean dust budget for the pre-industrial CTRL and PreVeg simulations are shown in Table 3.1. For the intercomparison, results from 7 different global dust models were used. The models simulated the pre-industrial dust cycle in the frame of the the AeroCom project (*http : //aerocom.met.no*). AeroCom models were nudged to year 2000 meteorology and aerosol emissions, except for natural emissions (e.g. dust, sea-salt), have been prescribed to the pre-industrial values as described in the previous section. Here, only the results from the CTRL run are described. The main results from the PreVeg simulation and the differences with the CTRL run are discussed in section 3.3.

Table 3.1— Global mass budget for the pre-industrial CTRL and PreVeg simulations

	CTRL	PreVeg	AeroCom
Emissions, $[Tg/yr]$			
Total	1540 (100%)	1375 (100%)	1570-1700
Sahara	559 (36%)	528 (38%)	
Southern Hemisphere	62 (4%)	225 (16%)	
Australia	60 (3.9%)	215 (15.6%)	
South America	1 (0.06%)	8 (0.6%)	
Southern Africa	1.2 (0.08%)	1 (0.07%)	
Deposition, $[Tg/yr]$			
Total deposition	1539 (100%)	1375 (100%)	
Wet deposition	643 (42%)	600 (44%)	168-758
Dry deposition	214 (14%)	184 (13%)	
Sedimentation	682 (44%)	591 (43%)	$(962 - 1507)^*$
Load, Tg	19.7	16.5	5.9-29.1
Lifetime, days	4.7	4.4	1.3-7.0

* - dry deposition plus sedimentation.

The simulated atmospheric burden and lifetime of mineral dust in the CTRL run are 19.7 Tg and 4.7 days respectively and lie within the range given by the AeroCom pre-industrial simulations. Dry deposition plus sedimentation in the CTRL simulation is slightly underestimated compared to AeroCom models, while wet deposition lies close to the high end of the AeroCom model simulations.

3.2.2 Dust emission

Mineral dust emissions depend on the vegetation cover fraction, 10 meter wind speed, soil moisture, snow cover as well as topography, surface roughness and soil types. The spatial patterns of dust emissions reflect the geographical distribution of arid and semi-arid areas (Fig.3.1).

The total dust emission in the CTRL simulation is 1540 Tg/yr. This value is in fairly good agreement with the total dust emissions from the pre-industrial AeroCom model simulations which lie between 1570 and 1700 Tg/yr. Simulated global dust emissions are dominated by the Northern Hemisphere dust sources, with large scale dust emissions from the Saharan and Asian arid regions. This is consistent with observations (e.g. Prospero et al., 2002) and other modeling studies (e.g. Huneeus et al., 2011). The main sources for dust deposition in Antarctica are located in the Southern Hemisphere. The Southern Hemisphere dust sources are South America, southern Africa and Australia. In order to evaluate the emission fluxes from each of the Southern Hemisphere dust sources in the CTRL simulation, the results from the ensemble of 14 state-of-the-art AeroCom models (AeroCom median) simulated for current climate conditions were used (for more details see Huneeus et al., 2011). The corresponding information from the AeroCom pre-industrial simulations is not available. In the CTRL simulation the Southern Hemisphere dust emissions are dominated by the Australian dust source. Dust emissions from Australia yield 60 Tg/yr, which is consistent with the study by Werner et al. (2002), and slightly higher than the AeroCom Median (Huneeus et al., 2011). Simulated emissions from southern Africa and South America are rather small and yield 1.2 and 1.0 Tg/yr respectively. Both of these values are underestimated compared to the AeroCom median value. This is a consequence of the prescribed vegetation map.

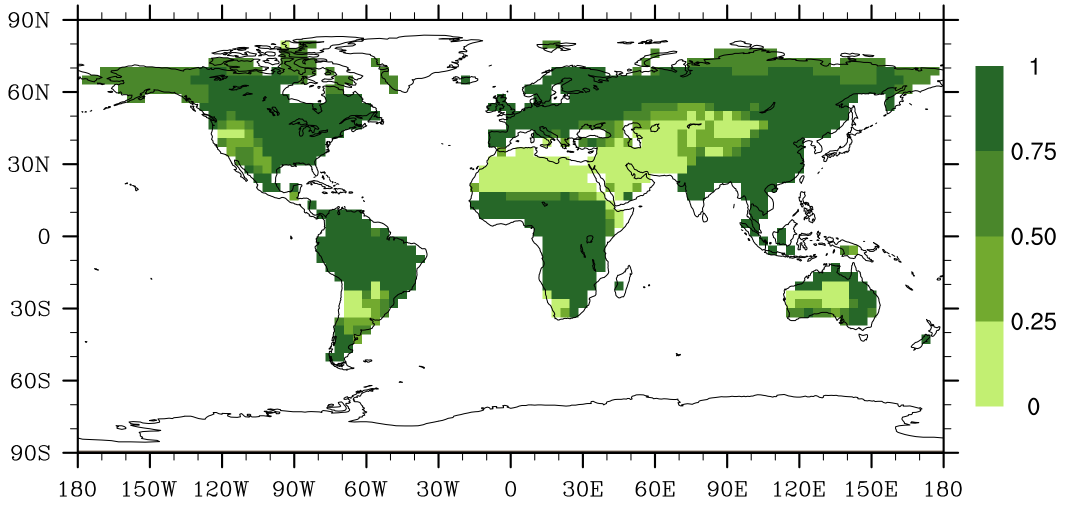

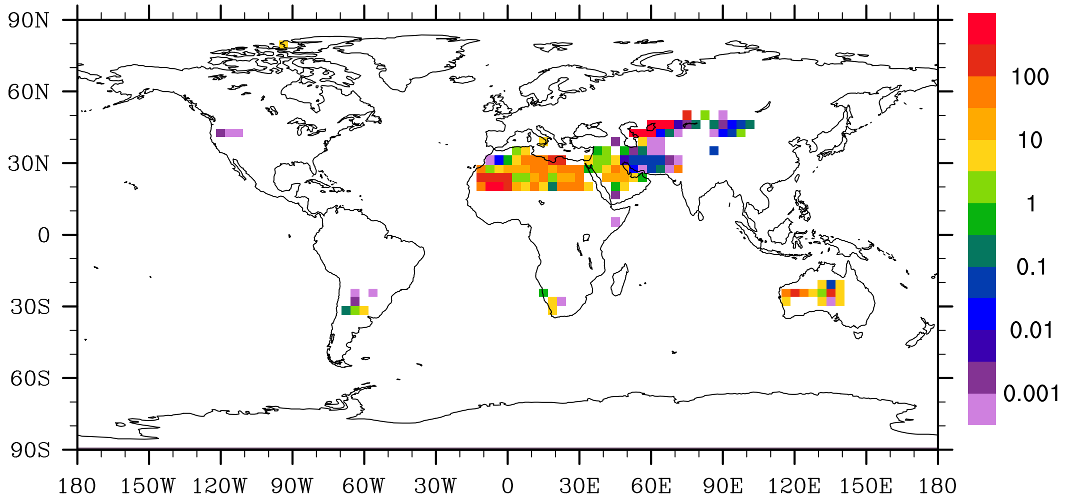

Figure 3.1— Annual maximum vegetation cover fraction obtained from the LPJ model (top) and mean dust emission flux $[g/m^2/yr]$ for the CTRL simulation (bottom).

Dust emissions as a function of wind speed and soil moisture

In order to examine the relation of dust emissions and wind speed, the distribution of dust emission mass flux as a function of wind speed over each of the Southern Hemisphere sources, was analyzed (Fig.3.2, left column).

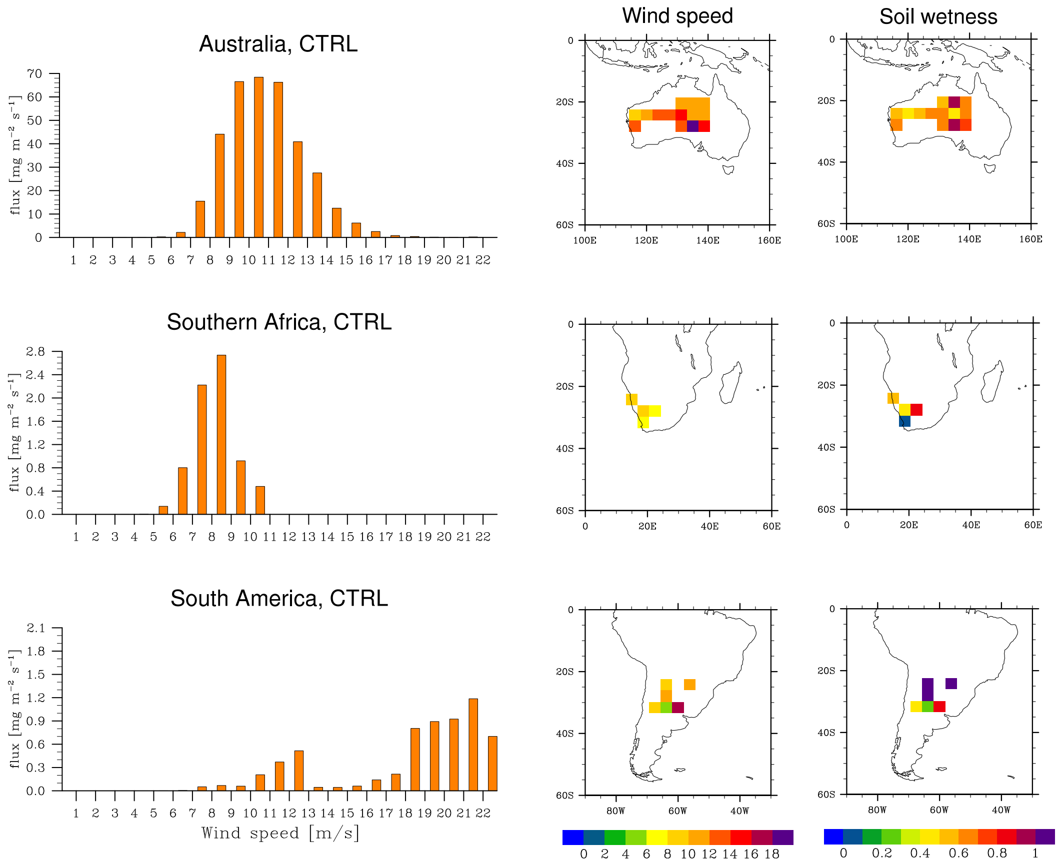

Figure 3.2— Distribution of the dust emission mass flux as a function of wind speed over the Australian, south African and South American dust sources (left column). The computation is based on 6 hour data for wind bins defined as 0-1, 1-2, 2-3, ... [m/s] for 20 years of the CTRL simulation. Typical wind speed [m/s] (middle column) and soil wetness [m] (right column) during dust emissions for different Southern Hemisphere source regions.

In Australia, maximum dust emissions are mobilized at wind speeds between 9-12 m/s. In southern Africa lower wind speed (7-9 m/s) is needed to lift up the dust particles. The distribution of South American emissions has two pronounced peaks at 11-13 and 18-23 m/s and differs significantly from the other Southern Hemisphere dust sources. The explanation of the two modal distribution of dust emissions in South America can be derived from the maps shown in the bottom row of Fig.3.2. The calculated typical wind speed during dust emissions shows high values in particularly one grid box at the east coast of South America $\sim 30°S, 60°W$.

The soil wetness at this grid point is relatively high, nevertheless dust emissions are also quite strong. The influence of soil moisture on the threshold friction velocity is such that the more moist the soil, the higher the wind speed needed to lift the dust particles. This explaines, why high wind speeds are required to lift up the dust particles from the ground. The reason for the occurrence of higher wind speeds in this grid point is the substantially lower topographic roughness length compared to the other grid points of the dust source area.

Seasonal variability of Southern Hemisphere dust emissions

The seasonal variability of Southern Hemisphere dust emissions affects the seasonality of dust deposition in Antarctica. In this section the seasonality of dust emissions from each of the Southern Hemisphere dust sources is analyzed (Fig.3.3, top) in terms of the probability density function (PDF) of wind speed over these sources (Fig.3.3, bottom). The changes of soil moisture within the year are small in arid and semi-arid areas and therefore are not considered.

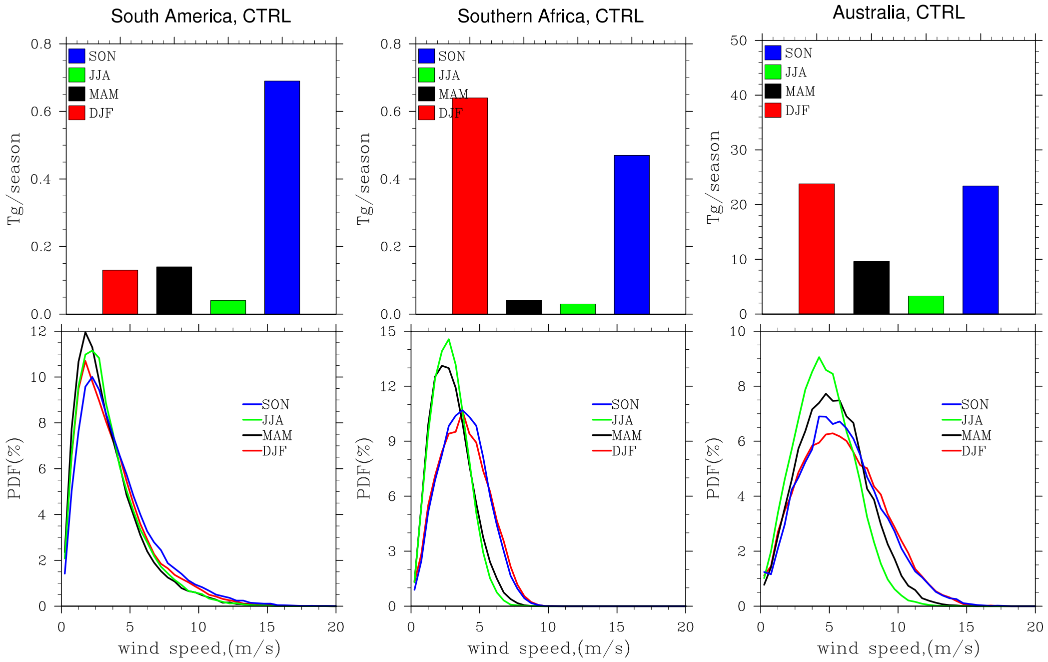

Figure 3.3— Seasonal cycle of dust emissions for the South American, south African and Australian dust sources (top) for the CTRL simulation. Note that scales are different. Seasonal cycle of probability density function of wind speed over corresponding dust sources (bottom).

Simulated dust emissions are in broad agreement with the PDF of wind speed, showing maximal mobilization in the seasons with the highest wind speed. These are austral summer (DJF) and spring (SON), the seasons with maximal land-ocean temperature gradient. Emissions from each of the Southern Hemisphere dust source from the CTRL run are compared with satellite observations of the global distribution of major dust sources following Prospero et al. (2002). Simulated dust emissions from Australia start to increase in October and reach their maximum in November-December, showing equally high emissions in SON and DJF. This is in general agreement with satellite observations, suggesting start of Australian dust mobilization in September-October and its maximum in December-February. Observations from southern Africa show maximum emissions in August-October, while the modeled emissions are maximal in November-January. The modeled seasonal cycle of South American dust emissions is in general agreement with observations and shows maximum activity in October-November. In contrast to the other Southern Hemisphere dust sources, relatively weak South American dust emissions in DJF compared to SON is explained by year-round regionally high soil moisture (Fig.3.2) and the lower probability of high wind speed in DJF compared to SON (Fig.3.3). Frequent high wind speeds in SON exceed the threshold friction velocity for moist soil and this is reflected in a peak in emissions in this season, while in all other seasons the wind speed is not high enough to pick up a significant amount of dust.

3.2.3 Dust deposition

In this section, the contribution of different deposition processes to the total deposition of mineral dust in Antarctica is discussed. Mineral dust can be removed from the atmosphere by wet and/or dry deposition processes. Wet deposition is the fraction of dust that is removed during precipitation events, while dry removal occurs from gravitational settling (sedimentation) and/or turbulent fluxes (dry deposition). Note that sedimentation and dry deposition remove particles only from the lowest model level, whereas wet deposition removes them from all levels between (and including) the precipitating clouds and the ground. An important difference between wet and dry removal processes is the way in which they vary with distance from the dust source. Sedimentation and dry deposition are strongest near the source, while wet removal becomes effective once the particles are transported into more moist regions.

Table 3.2— Dust deposition over Antarctica for the CTRL simulation

Deposition, $[Tg/yr]$	CTRL
Antarctica	
Total deposition	0.053 (100%)
Wet deposition	0.0477 (90.0%)
Dry deposition	0.0005 (0.9%)
Sedimentation	0.0048 (9.1%)

The dominant sink process of mineral dust in Antarctica is wet deposition (Table 3.2), which is in agreement with observational based estimates made for a coastal site in Antarctica (e.g. Wolff et al., 1998). However the model overestimates wet deposition in the interior of Antarctica, showing that it is still a main sink process, similar to previous model studies (e.g. Albani et al., 2011). In contrast, observations suggest dry deposition is the dominant sink process in high-latitude polar regions at inland sites (e.g. Legrand and Mayewski, 1997). Comparison of modeled and observed snow accumulation in Antarctic interior sites shows that the model overestimates precipitation over the Antarctic inland by a factor of about 1.5-2.5. This results in an overestimation of wet deposition of dust in the Antarctic interior. Another feature of the spatial distribution of wet deposition of dust in Antarctica is that wet deposition is higher in the western part of the continent than in the eastern part (Fig.3.4). This is due to the fact that West Antarctica gets somewhat more precipitation than East Antarctica (e.g. Schwerdtfeger, 1984). The seasonal cycle of dust deposition over Antarctica is described in section 3.2.5.

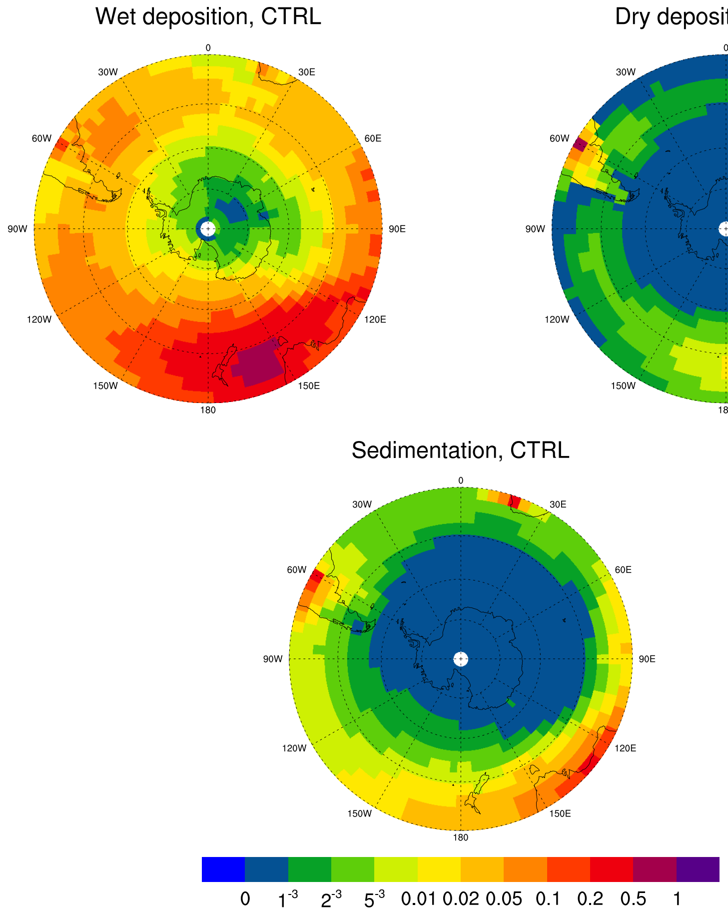

Figure 3.4— Annual mean wet deposition, dry deposition and sedimentation fluxes ($\mu g/m^2$) in the Southern Hemisphere for the CTRL simulation.

3.2.4 Dust concentration

The goal of this section is to examine the features of the modeled atmospheric dust concentration over different parts of the Southern Ocean, ranging from the dust source regions to Antarctica. To this end, vertical profiles of the annual mean dust concentration over the Southern Ocean divided into sectors from 0 to 30°, from 30 to 60° and south of 60° S and over Antarctica are analyzed (Fig. 3.5). Also the large-scale cloud cover and the fraction of gridbox occupied by updrafts, as an indication of the fraction of convective clouds in the gridbox, which is not explicitly diagnosed by the model, are shown.

Once dust is transported away from the source, the magnitude of the dust concentration decreases significantly and vertical profiles show an increase with height from the surface up to a certain level of maximum concentration, and a subsequent decrease at higher altitudes. The level of maximum dust concentration over the Southern Ocean rises from pressure level of about 920 hPa (level 16) for low latitudes to 630 hPa (level 12) for high latitudes (Fig.3.5 a-c). For detailed analysis of the vertical profiles of dust concentration, the three dimensional distribution of wet scavenging would be needed, which is not available in the model. For this reason, cloud cover of stratiform clouds and cumulus convective clouds is considered in order to explain the vertical profiles of dust concentration.

Most of the Southern Hemisphere dust sources are located at low latitudes. The main contribution to the freshly emitted dust mass close to the source regions is due to coarse particles. The maximum dust concentration over the Southern Ocean at low latitudes (on about 920 hPa, level 16) (Fig.3.5 a) is within the boundary layer, which typically extends up to about 870 hPa (level 15) (not shown). Thus, the boundary layer confines most of the particles, with a comparatively small mass escaping into the free troposphere.

The further the dust is transported away from the sources, the fewer coarse particles remain in the atmosphere. In mid-latitudes, the layer of maximal dust concentration rises up to about 800 hPa (level 14) (Fig.3.5 b), which is above both the boundary layer and the level of maximal large-scale cloud cover, which act as a removal mechanism for the dust particles.

As a result of the heavy cloud bands around the Antarctic continent, the vertical level of maximum dust concentration over the ocean rises significantly with increasing latitude, as more and more particles are removed from within and below clouds, while the magnitude of dust concentration shows a corresponding decrease (Fig.3.5 c). The maximum dust concentration level in high latitudes lies between two stratiform cloud layers, on about 630 hPa (level 12).

The dust concentration over Antarctica increases from the lowest model level up to about 740 hPa (level 16) and decreases upward from about 700 hPa (level 15). In Antarctica, a small amount of solar energy is absorbed by the surface and this, combined with the greater emissivity of the surface (compared to the atmosphere) induces a temperature inversion over the continent. Thus temperature inversion layer hinders the penetration of dust particles from free atmosphere into the surface

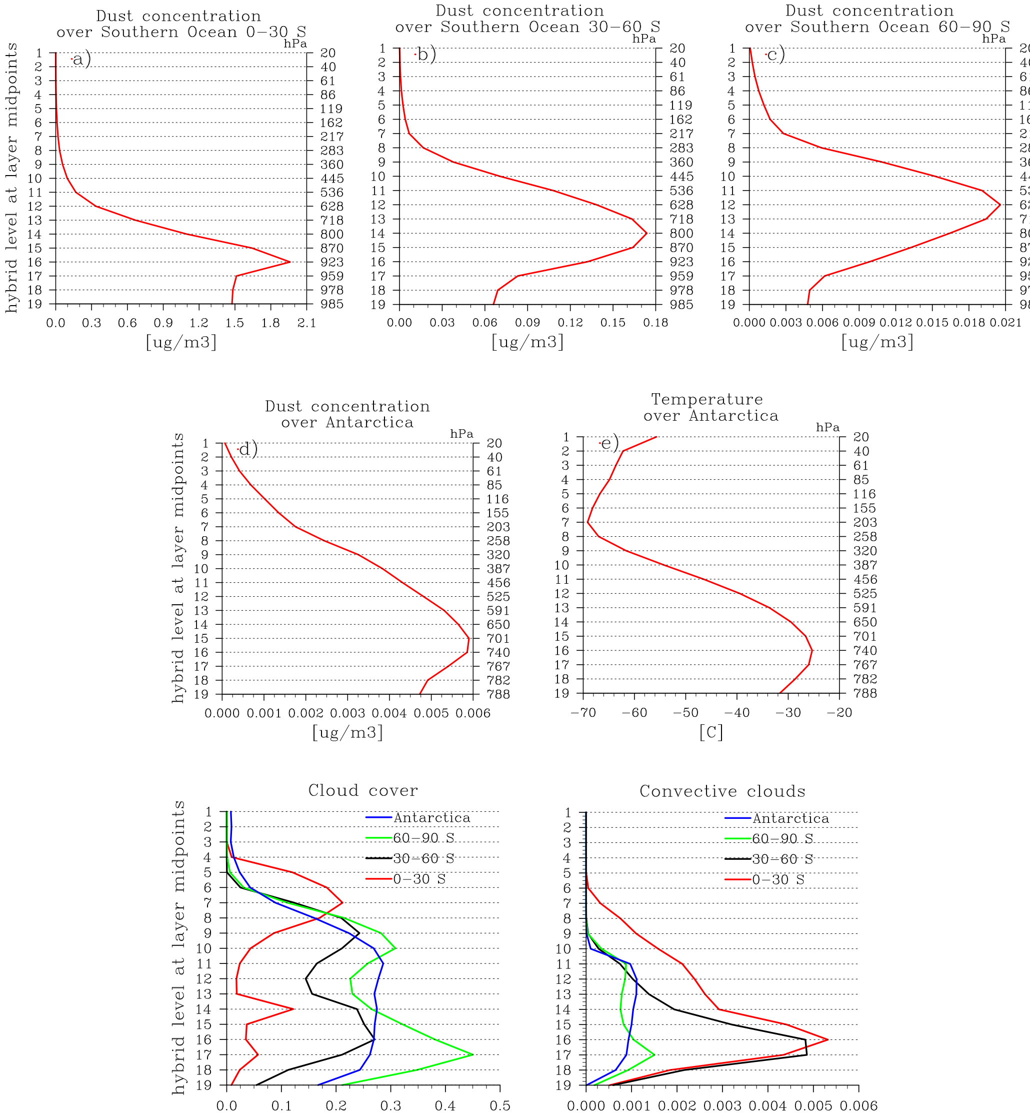

Figure 3.5— Vertical distribution of mean dust concentration [$\mu g/m^3$] for the CTRL simulation over the Southern Ocean from $0-30°$ (a), $30-60°$ (b), south of $60°$ south (c) and over Antarctica (d) and temperature profile over Antarctica (e), large-scale cloud cover (f) and the fraction of gridbox occupied by updrafts (g).

layer.

The seasonal zonal mean dust concentration over the Southern Hemisphere (Fig.3.6) reflects the seasonality of dust emissions. The dust concentration over Antarctica is maximal in SON.

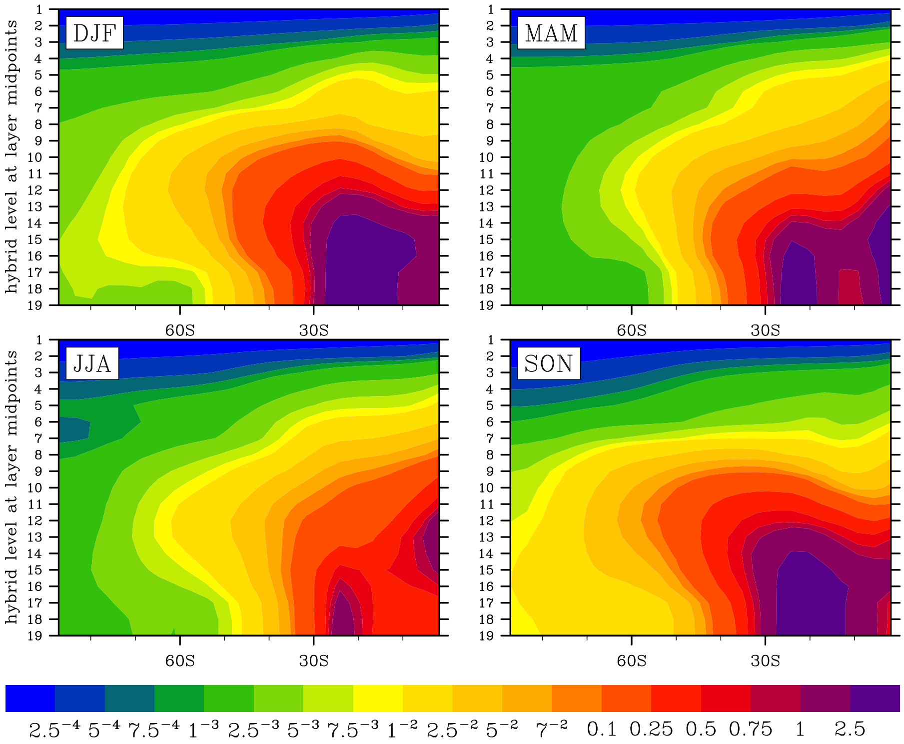

Figure 3.6— Vertical distribution of dust concentration $[\mu g/m^3]$ for the CTRL simulation for the Southern Hemisphere, seasonal mean.

3.2.5 Processes influencing dust deposition in Antarctica

The amount of mineral dust deposited depends on the amount of emissions and on the transport and removal of particles along the transportation path. One of the possibilities to describe the atmospheric transport is by means of air mass trajectories. Air mass trajectories from the Southern Hemisphere dust sources to Antarctica were calculated. To calculate trajectories, 6 hourly data of the meridional, zonal and vertical components of wind from 20 years of simulation were used. Trajectories were calculated once per day. We considered trajectories originating over the Southern Hemisphere dust sources at pressure levels of 800 hPa and 500 hPa that reached Antarctica within 10 days. The three-dimensional passive tracer trajectories were calculated based on bilinear velocities interpolation. The 500 hPa and 800 hPa pressure levels have been chosen in order to analyze the atmospheric dust transport in the low and middle troposphere. According to Krinner et al. (2010), there are two types of tropospheric tracer transport towards the interior of the Antarctic continent. The first type is fast, low-level advection enhanced by cyclonic systems off the Antarctic coast. The second type is advection via mass convergence in the middle troposphere above Antarctica. For example, SON trajectories originating over the Southern Hemisphere dust sources at 500 hPa and reacing Antarctica are shown in Fig.3.7.

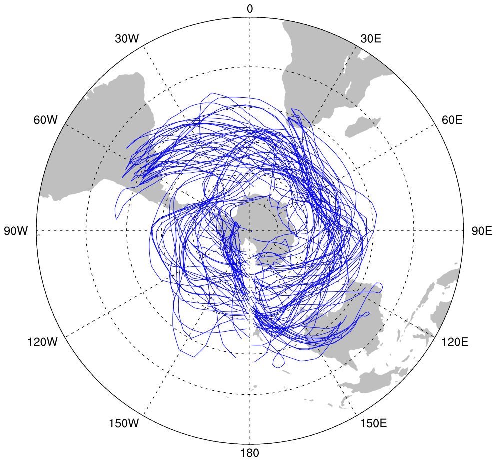

Figure 3.7— Ten day forward trajectories of air masses on 500 hPa originating over the South American, south African and Australian dust sources and reaching Antarctica. Note that only every 10-th trajectory is plotted.

The number of trajectories for the CTRL simulation originating at the heights of 800 hPa and 500 hPa over the Southern Hemisphere dust sources and reaching Antarctica within 10 days for different seasons, are shown in Table 3.3.

The atmospheric transport from the Southern Hemisphere dust sources towards

Table 3.3— Total number of trajectories originating at the height of 800 hPa and 500 hPa over Southern Hemisphere dust sources and reaching Antarctica within 10 days and total number of potential trajectories originating over Southern Hemisphere dust sources for the CTRL simulation.

	CTRL 800hPa	CTRL 500hPa
Number of trajectories originating over SH sources and reaching Antarctica		
DJF	979 (5.7%)	702 (10.3%)
MAM	4391 (25.6%)	2307 (33.9%)
JJA	8234 (48.0%)	2496 (36.7%)
SON	3565 (20.8%)	1301 (19.1%)
Σ	17169 (8.7%)*	6806 (3.5%)*
Total number of potential trajectories originating over SH sources	197100	197100

* - Percentage is calculated relative to the total number of potential trajectories originating over the Southern Hemisphere dust sources.

Antarctica is more active in winter (JJA) and minimal in summer (DJF) for both the low- and middle troposphere. The seasonality of transport is strongly pronounced in the low-level troposphere, while it is weaker in the middle troposphere. These results are similar to previous studies by Krinner et al. (2010), where the modeled radon-like tracer concentrations were analyzed. In that study, it has been shown that the tracer concentration near the Antarctic surface is maximal in winter and about 3 times lower in summer due to seasonal variations of the atmospheric transport between the source regions and Antarctica.

For the CTRL simulation, the number of trajectories in the low troposphere is higher than in the middle troposphere, by a factor of about 2.5. However, dust transport in the middle troposphere is more efficient because particles are less affected by wet removal than in the low tropospere.

The number of trajectories originating on low level and reaching Antarctica is about 8.7% of the total number of trajectories originating over Southern Hemisphere dust sources at that level. The trajectories that originated at pressure level of 800 hPa and reaching Antarctica originate mainly over the Australian source, while the 500 hPa trajectories reaching Antarctica mostly originate over South America. The percentage of trajectories originating over different dust sources to the total number of trajectories remains similar to that for trajectories entering the Antarctic continent. However, Li et al. (2008) suggest that over the Southern Ocean and Antarctica, the maximum concentration of dust originating from the Australian source is located in the upper troposphere. Dust originating from the South American source is concentrated mostly in the low troposphere. The reason for this disagreement may lie in the different dust source locations in South America. In Li et al. (2008)

the Patagonian source is located further southward compared to the Pampas region (about $30 - 35°$ S, $60 - 65°$ W) in our simulation. Driven by strong westerly winds, Patagonian dust is transportred in the boundary layer before being lifted into the free troposphere by low pressure systems (Li et al., 2008; Gasso et al., 2010). The Puna-Altiplano Plateau is located at higher altitude and dust from this source could more easily reach the free troposhere.

The impact of various processes, such as emissions, transport and precipitation on dust deposition in Antarctica is estimated and shown schematically in Fig.3.8. Muliplying the Southern Hemisphere dust emissions with the number of trajectories leading to Antarctica defines a quantity, which we will call dust transport efficiency (in arbitrary units). This gives some idea about both, how much dust is emitted and how often dust is transported to Antarctica.

For the CTRL simulation, Southern Hemisphere dust emissions are strongest in DJF and SON, but due to weaker transport in DJF compared to SON, the deposition over Antarctica in DJF is almost 3 times lower compared to the deposition in SON. The influence of precipitation can be seen in MAM, when relatively strong dust transport efficiency is affected by high (seasonal maximum) precipitation over the Southern Ocean, which results in seasonal minimum deposition in Antarctica. In JJA, the combination of a weak dust transport efficiency, together with high precipitation, causes relatively low dust deposition in Antarctica.

In the CTRL simulation the dust deposition on the Antarctic plateau is maximal in spring (SON) and relatively low in other seasons. A similar result was shown in Albani et al. (2011). Observations suggest a different seasonal cycle of dust deposition at different sites in Antarctica. The recorded annual cycle of dust deposition at Law Dome shows spring (SON) and autumn (MAM) maximum (Burn-Nunes et al., 2011), while observations by Edwards et al. (1998) at the same site suggest a spring/summer maxima. In our simulation dust deposition at Law Dome shows a maximum during spring/summer. Observations at James Ross Island station show a maximum dust deposition in late winter (McConnell et al., 2007), which is close to the simulated spring maximum at that site. Similarly, the simulated maximum dust deposition at the Berkner Island site is in spring, while observations show a spring/summer maximum (Bory et al., 2010).

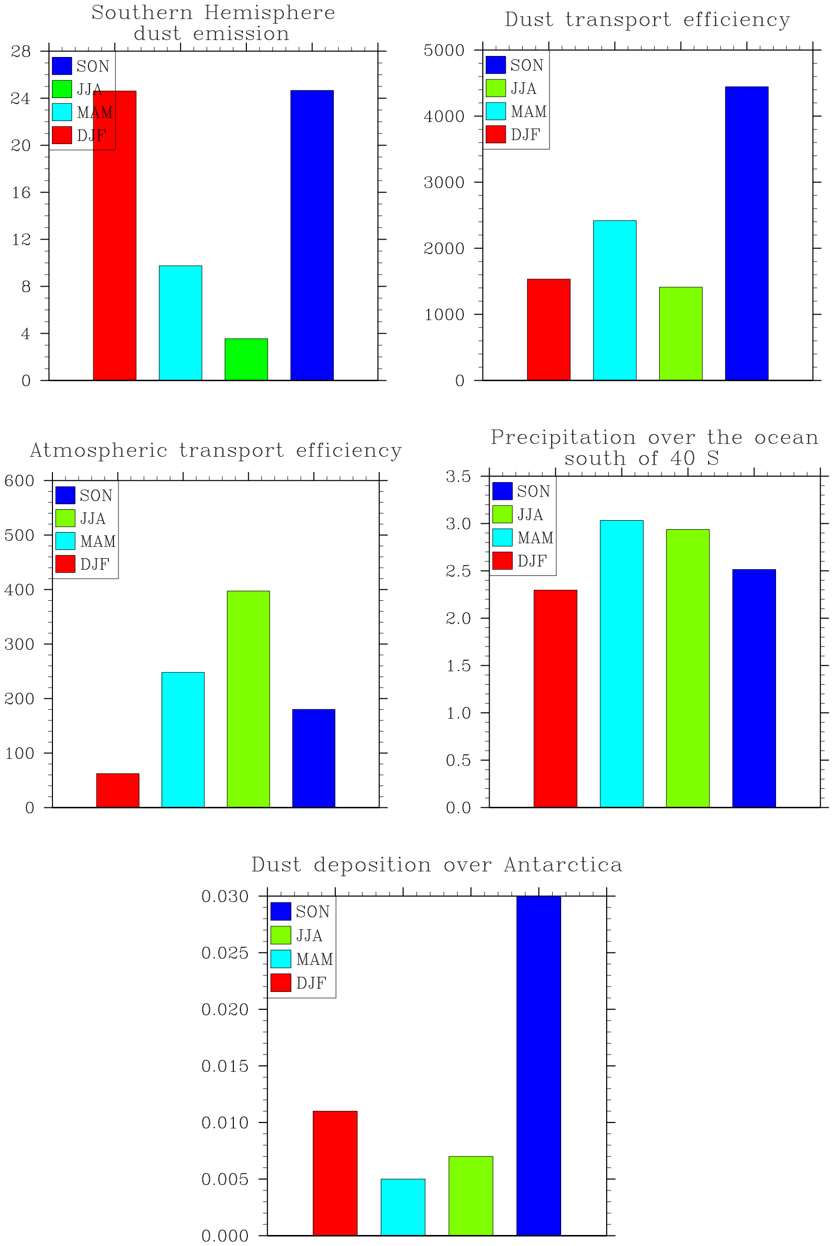

Figure 3.8— Impact of Southern Hemisphere dust emission $[Tg/season]$ (top left), atmospheric transport efficiency $[trajectories\, per\; season]$ (central left), the dust transport efficiency $[arbitrary\, units]$ (top right), precipitation over the ocean south of $40°$S $[mm/day]$ (central right) on dust deposition in Antarctica $[Tg/season]$ (bottom) for the CTRL simulation. Atmospheric transport efficiency is a sum of number of trajectories per season originated at 500 hPa and 800 hPa from a single dust source grid box and reached Antarctica within 10 days.

3.2.6 Atmospheric transport towards Antarctica

In this section, the atmospheric transport is investigated in greater detail. In particular the roles of mean polar transport and transport by turbulent eddies are examined. The vertical profiles of the meridional component of the mean wind (v) for the Southern Hemisphere for different seasons are shown in Fig. 3.9. It can be seen that the mean meridional wind is poleward in mid-latitudes in the low troposphere and in high latitudes in the middle troposphere.

The polar high pressure system leads to a large scale low level divergence over Antarctica. Near the surface, strong katabatic winds occur, which yield very strong equatorward transport, especially in austral winter (JJA.) This is in agreement with the studies by Parish and Cassano (2003) and Parish and Bromwich (2006), where it has been shown that katabatic winds are especially strong during the winter period as a consequence of continent cooling. As the contitent cools, drainage flow intensify and northward low-level mass fluxes from Antarctica increase. Summertime winds cannot be expected to contain a significant katabatic component, due to enhanced solar heating of the ice slopes.

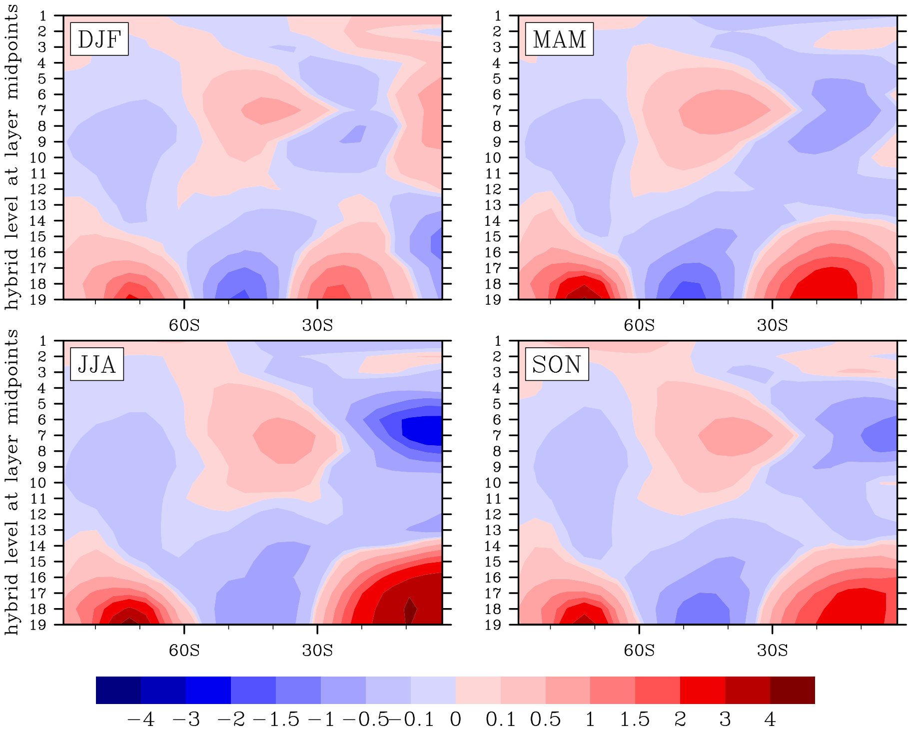

Figure 3.9— Seasonal mean zonal average meridional component of wind (V), $[m/s]$ over the Southern Hemisphere for the CTRL simulation. Blue color indicates a poleward wind, red indicates an equatorward wind. The x-axis shows latitudes, the y-axis shows hybrid model levels.

To analyze mean meridional dust flux (Fig.3.10), 6 hourly mean meridional winds (Fig.3.9) are multiplied by 6 hourly instantaneous dust concentrations (Fig.3.6). The most effective dust transport towards Antarctica is at pressure levels of about 500 hPa (levels 10-12, depending on latitude). It also can be seen that the near-surface equatorward dust flux over high southern latitudes is confined much closer to the surface than the meridional wind. Since the dust concentration cannot change sign, this must be due to a negative correlation between dust concentration and meridional wind. This leads to the question of how the synoptic scale eddies and other short-term processes, (e.g. diurnal cycles) influence the total transport.

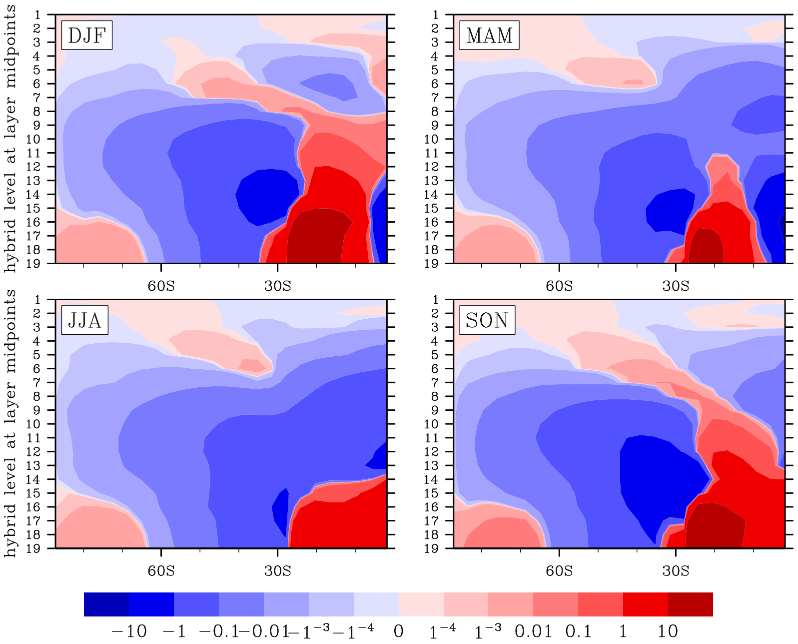

Figure 3.10— Seasonal mean zonal average meridional dust flux $[\mu g/m^2/s]$ over the Southern Hemisphere for the CTRL simulation.

In Fig.3.11, the influence of eddy fluxes and other short-term processes has been approximately estimated by taking the difference between the time mean of the product of 6 hourly values of dust concentration and meridional wind and the product of time means of these quantities. Note that the 6-hourly model output step is much too long to resolve turbulent processes in the atmosphere, which have a characteristic timescale of at most one hour (Stull, 1988), but is still short enough to resolve, for example, diurnal cycles and cyclone activities.

It can be seen that, except for some near-surface values in DJF and MAM, the short timescale processes contribute to the poleward transport of dust. A stronger than average southward wind (negative anomaly) brings, in general, more dust than the surroundings to which it is transported (positive concentration anomaly). The

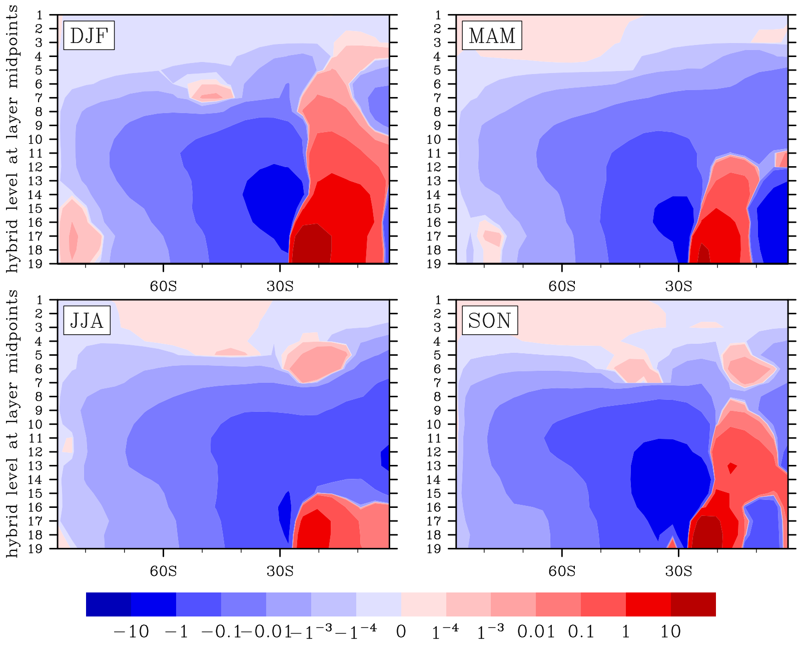

Figure 3.11— Seasonal mean zonal average synoptic scale eddy flux ($\overline{V \cdot DU} - \overline{V} \cdot \overline{DU}$) over the Southern Hemisphere for the CTRL simulation.

product of these two is therefore a negative (poleward) dust flux anomaly. This means that synoptic scale eddy fluxes generally increase dust transport to Antarctica. In DJF, the temperature gradient between the Antarctic continent and the Southern Ocean reduces due to more solar energy received over Antarctica, which results in less stable equatorward movement of air. This leads to a relative increase of the synoptic scale eddy flux component of the relatively weak katabatic wind in DJF and MAM. In contrast, in other seasons the katabatic wind is almost constantly present (transport of air is stable) due to the strong temperature gradient between land and ocean and the synoptic scale eddy flux transport is substantially weaker.

For a more complete understanding, shorter time interval output and a model with a better spatial resolution would be needed. However, it can be stated that short-term processes, on the order of one day or less, are also important for the transport of dust at high southern latitudes.

3.3 Simulation of the dust cycle for pre-industrial climate conditions with satellite derived vegetation

In this section, the differences between the CTRL simulation with modeled vegetation and the PreVeg simulation with a vegetation fraction obtained from satellite data are discussed. This analysis is done in order to check how well the simulated pre-industrial vegetation cover captures the main arid regions and how the differences in vegetation cover between the modelled pre-industrial and the observed present vegetation could affect the simulated dust cycle, especially the dust deposition over Antarctic region.

For the PreVeg simulation, the monthly mean global vegetation cover fraction and leaf area index, allocated by Hagemann et al. (1999) as typical parameter values to major ecosystem classes obtained from satellite observations, were used. The distribution of major ecosystem classes, based on advanced very high resolution radiometer (AVHRR) satellite data, covering April 1992 to March 1993, were provided by the United States Geological Survey. The 1 km resolution AVHRR data set was acquired by the National Oceanic and Atmospheric Administration's (NOAA) Television Infrared Observation Satellite (TIROS). The vegetation fraction and the leaf area index data were impoved by using photosynthetic absorbed radiation (FPAR) derived by Knorr (1997, 1998) from data of Berthelot et al. (1994) based on NOAA/AVHRR data at 0.5 degree resolution.

The annual mean vegetation cover fraction derived from the satellite observations, as well as the annual vegetation maximum (to be consistent with the CTRL simulation) and mean dust emission flux are shown in Fig.3.12.

Due to different vegetation maps, the contribution of different dust sources to the total dust emission flux in the PreVeg simulation differs from that in the CTRL simulation (Table 3.1). (For the global distribution of dust emissions in the CTRL simulation see Fig.3.1). Southern Hemisphere dust emissions in the PreVeg simulation are higher by a factor of 3.6 compared to the CTRL simulation due to increased emissions from Australia. The modeled seasonality of Australian dust emissions in the PreVeg simulation (Fig.3.3) is similar to the CTRL run (Fig.3.3) with slightly amplified emissions in DJF compared to SON. This is a consequence of the seasonal variability of vegetation cover in PreVeg in contrast to the annual maximum vegetation in CTRL. Thus, the seasonality of dust emissions from Australian source in PreVeg is in better agreement with observations (Prospero et al., 2002), suggesting start of Australian dust activity in September-October and its maximum in December-February, whereas the CTRL simulation shows equally high emissions in SON and DJF. However, the model overestimates dust emissions from Australia in the PreVeg simulation in comparison to the AeroCom median value (Huneeus et al., 2011). According to Werner et al. (2002) the original ECHAM wind fields (non-corrected by e.g. ECMWF) result in too high emissions over Australia and Sahara, which in case for the CTRL simulation was compensated by the smaller source area extend in Australia. Note, that Werner et al. (2002) used ECHAM4 wind.

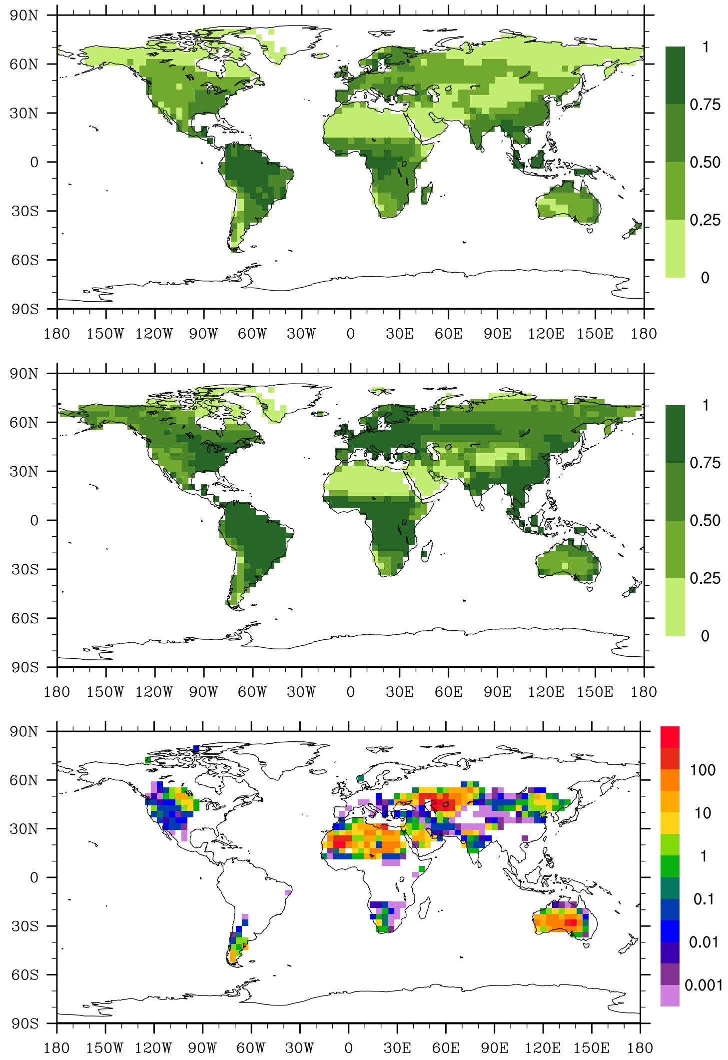

Figure 3.12— Annual mean and annual maximum vegetation cover fraction derived from satellite observations (top) and mean dust emission flux for the PreVeg simulation, $[g/m^2yr]$ (bottom). For a comparison with the CTRL simulation see Fig.3.1.

The dust source in South America in the PreVeg simulation extended significantly from Puna-Altiplano Plateau (about 20 – 30° S, 70° W) to Patagonia, while in the CTRL run, the Patagonian source is not captured by the model due to lack of arid areas in the southernmost part of the continent. However observations (Prospero et al., 2002) suggest the presence of an active dust source in the Patagonian region, although some of this area (Santa Cruz 46 – 48° S) has been linked to anthropogenic activities. The seasonal cycle of south American dust emissions in the PreVeg simulation (Fig.3.13) differs from the CTRL run (Fig.3.3). In the PreVeg simulation, South American dust emissions are maximal in DJF and minimal in

SON, while in the CTRL run, the peak of emissions occurs in SON. Observational records from different parts of Patagonia show different seasonal patterns, among which flux peaks are in DJF, MAM, JJA and in early spring (Gaiero et al., 2003). South American dust emissions in the PreVeg simulation yield 8 Tg/yr and are consistent with the AeroCom median estimate (Huneeus et al., 2011). The change of dust emissions from southern Africa in the PreVeg simulation compared to the CTRL run is negligible. The comparison of Southern Hemisphere dust emissions from two pre-industrial runs, shows better representation of South American emissions in the PreVeg simulation, however representation of Australian emissions is more realistic in CTRL.

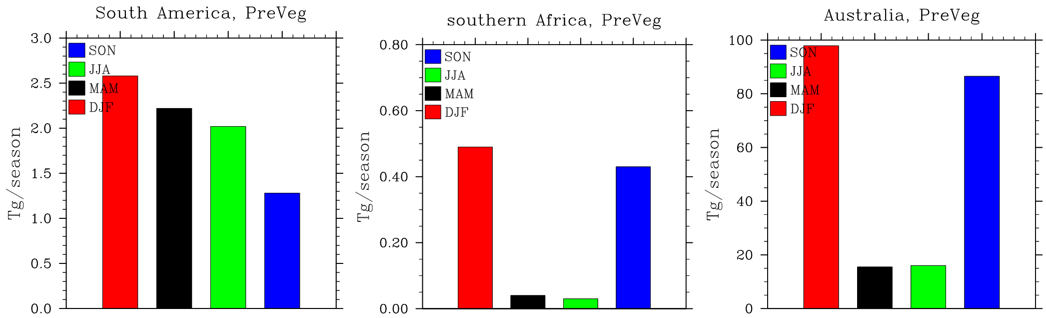

Figure 3.13— Seasonal cycle of dust emissions for South American, south African and Australian dust sources. Note that scales are different.

The seasonality of dust deposition in Antarctica is similar in the PreVeg and CTRL simulations with maximum deposition in SON (Fig.3.14). This is due to the dominant role of the Australian source in both runs with a similar seasonal cycle of emissions. Total dust deposition over Antarctica in the PreVeg simulation is about 6 times higher than in the CTRL run.

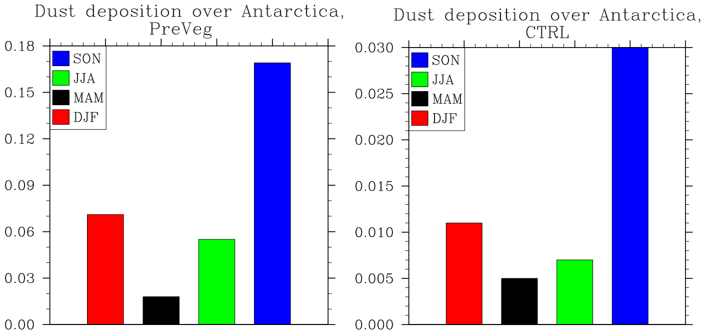

Figure 3.14— Seasonal distribution of mineral dust deposition over Antarctica for the PreVeg and CTRL simulations.

Chapter 4

Paleo time-slice simulations

> Among the longest astrophysical and astronomical cycles that might influence climate only those involving variations in the elements of the Earth's orbit have been found to be significantly related to the long-term climatic data deduced from the geological record.
>
> Berger 1988

4.1 Simulation of the dust cycle for interglacial climate conditions

This section is concerned with paleoclimate simulations in terms of dust emission, transport and deposition, and how these quantities vary between different paleoclimates. The reasons for the modeled differences are explored, and we seek explanations of these differences in terms of the orbital forcing of climate relevant to each time period, the resulting basic climate variables, such as winds and precipitation, as well as the boundary conditions that drive the model dust scheme.

The chapter is divided into two main parts: the first describes the interglacial time-slice simulations, and the second describes the simulation of a Last Glacial Maximum (LGM) time slice. Within each of these sections, first the prescribed radiative forcing is presented, followed by the resulting climate in terms of temperature, precipitation and atmospheric circulation. Next, the emission of dust in each time-slice is analyzed and assessed in terms of vegetation cover, the dust source area extent, soil moisture and wind speed distribution over the source areas. This is followed by an examination of the different removal processes. The atmospheric transport of dust towards Antarctica is also examined in detail.

4.1.1 Experimental setup

For the three last interglacial periods, 20-year paleo-slice simulations after 5 years of spin up were performed. These are paleo-slice simulations for the climate of the mid-Holocene (6,000 years BP, hereafter 6 kyr), the last glacial inception (115,000 years BP, hereafter 115 kyr) and the Eemian (126,000 years BP, hereafter 126 kyr).

The paleo-slice simulations for the past interglacial periods differ from the CTRL simulation in following characteristics:

1) Orbital parameters were modified following the PMIP2 protocol ($http : //pmip2.lsce.ipsl.fr$, Braconnot et al., 2007) and listed in Table 4.1.

2) Sea surface temperature (SST), sea ice concentration and surface background albedo were obtained for each paleo interval from long-term simulations by the coupled atmosphere-ocean-vegetation model ECHAM5/MPIOM/LPJ. Vegetation information was obtained from the dynamical vegetation model LPJ (see details in chapter 3.1). Greenhouse gas concentrations are kept similar to the pre-industrial conditions, except for CH_4, which was reduced by 0.1 [ppm] for 6 kyr following the PMIP2 protocol (Table 4.2).

Table 4.1— Orbital parameters for the CTRL, 6 kyr, 115 kyr, 126 kyr simulations derived from the PMIP2 protocol.

	CTRL	6 kyr	115 kyr	126 kyr
eccentricity	0.016724	0.018682	0.041421	0.03971
obliquity	23.446	24.105	22.404	23.928
day of perihelion	282.04	180.87	290.88	111.24

Table 4.2— Greenhouse gas concentrations for the CTRL, 6 kyr, 115 kyr, 126 kyr simulations derived from the PMIP2 protocol.

	CTRL	6 kyr	115 kyr	126 kyr
CO_2, [ppm]	280	280	280	280
CH_4, [ppm]	0.76	0.65	0.76	0.76
N_2O, [ppm]	0.27	0.27	0.27	0.27

Prescribed SST is lower by −0.07°C in 6 kyr, by −0.08°C in 115 kyr and by −0.13°C in 126 kyr compared to the pre-industrial global mean temperature.

4.1.2 Large-scale features of mean climate state

Insolation

The changes in the orbital parameters of the Earth modify the latitudinal and seasonal distribution of the incoming solar radiation at the top of the atmosphere (insolation), according to Berger (1987). These orbital parameters are the eccentricity, the obliquity and the longitude of perihelion.

Changes in obliquity (tilt) of the Earth's axis have an impact on seasonal contrasts, mostly in high latitudes, but not on the total amount of solar radiation received by the Earth. Variations in the Earth's axial tilt affect the strength of the latitudinal temperature gradient. For example, increased tilt has the effect of raising the annual receipt of solar energy at high latitudes, with a consequent reduction in the latitudinal temperature gradient (Roeckner et al., 2003).

Precession of the equinoxes and longitude of perihelion (the point at which the Earth passes closest to the Sun) associated with shifts in the position of solstices and equinoxes on the orbit relative to the perihelion occur and this modulates the intensity of the seasons. Due to the gravitational interaction of the Earth with other planets in the solar system, the perihelion moves in space with a consequent shifting, or precessing, of the elliptical orbit. This phenomenon is known as the precession of the equinoxes, and affects the intensity of the seasons, but not the total amount of solar energy received by the Earth.

Changes in eccentricity (or ellipticity) of the Earth's orbit modulate the distance between Sun and Earth and influence the seasonal distribution and total amount of solar radiation received at the top of the atmosphere.

The orbital parameters for the different time-slices are listed in Table 4.1. The date of perihelion is shifted from January for the pre-industrial time-interval to September in 6 kyr and to July in 126 kyr. This leads to a enhancement of the insolation seasonality in the Northern Hemisphere in 6 kyr with its maximal amplification occuring in 126 kyr time-slice compared to the CTRL simulation (Fig.4.1, left column). The seasonal cycle of incoming solar radiation in the Southern Hemisphere is reduced. For 6 kyr, the simulated mean insolation received by the Northern Hemisphere is 24 $W/m2$ (+5.4%) greater in July (summer) and 10 $W/m2$ (-4.6%) less in January compared to the pre-industrial value (similar to Joussaume et al., 1999). However for the Southern Hemisphere the solar radiation in January (summer) is decreased by 23 $W/m2$ (-4.9%), whereas it increases by 8 $W/m2$ (+3.6%) in July. For 126 kyr, the mean insolation received by the Northern Hemisphere is 46 $W/m2$ (+10%) greater in July and 20 $W/m2$ (-9%) less in January compared to the pre-industrial value. In the Southern Hemisphere the mean solar radiation in January decreases by 52 $W/m2$ (-11%) and it increases by 31 $W/m2$ (+15%) in July.

On the contrary, in 115 kyr the seasonality of insolation is reduced in the Northern Hemisphere and increased in the Southern Hemisphere compared to CTRL. This results from the perihelion occuring in January (which is similar to the pre-industrial)

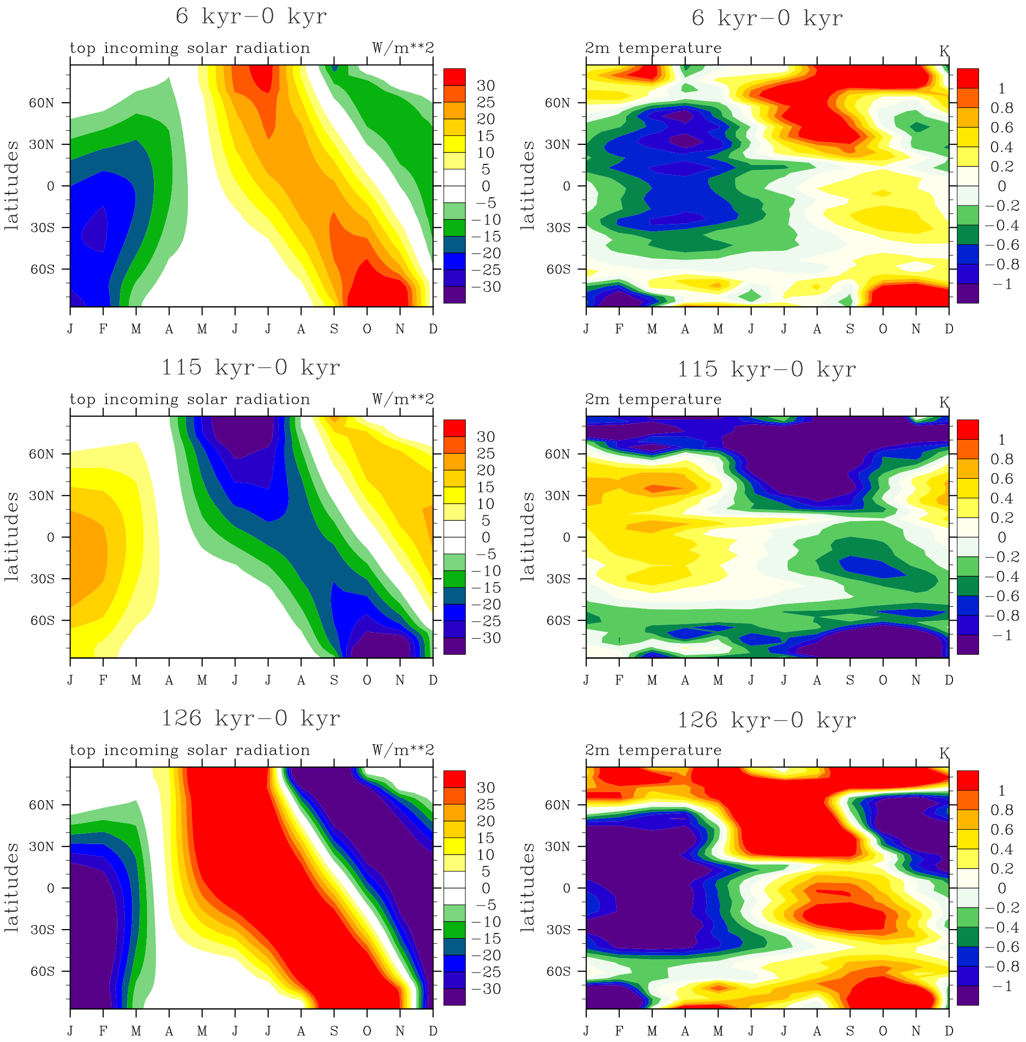

Figure 4.1— Difference of incoming solar radiation at top of the atmosphere [W/m^2] (left column) and 2m air temperature [$°C$] (right column) as a function of latitude and time of year between the 6 kyr, 115 kyr, 126 kyr and CTRL simulations.

and maximal increase in eccentricity compared to the pre-industrial or other interglacial time-slices. Additionally, the axial tilt of the Earth (obliquity) in 115 kyr is almost 1° lower, which affects high latitudes. For 115 kyr, the mean insolation received by the Northern Hemisphere is 24 $W/m2$ (-5.4%) less in July and 15 $W/m2$ (+6.6%) greater in January compared to the pre-industrial values. Whereas in the Southern Hemisphere the mean solar radiation in January increases by 21 $W/m2$ (+4.6%) and decreases by 7 $W/m2$ (-3.2%) in July.

The modeled global annual mean insolation change is about +0.01 $W/m2$ for 6 kyr, +0.24 $W/m2$ for 115 kyr and +0.22 $W/m2$ 126 kyr.

2m temperature

The insolation change induces a temperature response (Fig.4.1, right column). The latitudinal distribution of seasonal air temperature anomalies is generally consistent with the insolation anomalies, although in the Southern Hemisphere the temperature response is smaller than in the Northern Hemisphere due to the larger fraction of ocean and the associated larger heat capacity.

In concordance with the prescribed insolation changes, the simulated seasonal cycle of 2m temperature is increased in the Northern Hemisphere and decreased in the Southern Hemisphere for 6 kyr and 126 kyr compared to pre-industrial. In 6 kyr and 126 kyr the simulated near-surface air temperature in high northern latitudes are higher throughout the entire year compared to CTRL, with some exception in 6 kyr boreal spring (Fig.4.1, right column). This is caused mainly by the perihelion shift and by the greater axial tilt of the Earth. This leads to increased availability of solar energy at high northern latitudes during summer time. The ocean stores part of this energy, sea ice thickness is reduced (not shown) and the resulting enhanced heat release of the ocean in winter leads to the surface warming.

The modeled global 2m temperature over the continents is about $+0.6°C$ higher in austral summer in 6 kyr and $+2°C$ higher in 126 kyr, and about $-0.4°C$ lower in austral winter in 6 kyr and $-1°C$ lower in 126 kyr compared to the preindustrial values (App.A.1). In 6 kyr and 126 kyr, annual warming reaches a maximum over parts of North Africa between $20-30°N$ with about $+2°C$ for 6 kyr and about $+4°C$ for 126 kyr, whereas the cooling occurs further south, between $0-20°N$ and over north India (Fig.4.2). This cooling can be attributed to increased cloud cover and precipitation due to more active summer monsoon processes (App.B.1) (Joussaume et al., 1999; Braconnot et al., 2007). Summer warming reaches a maximum over some regions in Tibetan and Mongolian Plateaus, and North Africa of about $+3°C$ for 6 kyr and about $+7°C$ for 126 kyr (App.A.1). In the Southern Hemisphere: South America, southern Africa and Australia show maximal warming in SON by about $+2°C$ for 6 kyr and in JJA-SON by about $+3°C$ for 126 kyr compared to pre-industrial temperature, which is consistent with the change in radiative forcing.

The seasonal cycle of 2m air temperature for 115 kyr is slightly decreased in the Northern Hemisphere and slightly increased in the Southern Hemisphere (Fig.4.1, right column) compared to pre-industrial conditions with some regional exceptions. In JJA the regional warming occurs in the south of North Africa (App.A.1) due to a reduction of cloud cover resulting from a weakening of convective processes. The cooling at high latitudes of both hemispheres during the entire year can be explained by the perihelion shift and a lower axial tilt in 115 kyr, leading to a reduction of the seasonality in the polar regions. In the Arctic, sea ice cover and thickness increase, which causes a decrease of the heat exchange between the ocean and atmosphere over the entire year.

Modeled global mean 2m air temperature over the continents is about $-1°C$ lower in boreal summer and about $+0.5°C$ higher in boreal winter in 115 kyr compared to the pre-industrial values. Annual cooling reaches a maximum in the Barents Sea (by about $-5°C$) (Fig.4.2) as a consequence of extended sea ice cover. Cooling also occurs over the northern part of Eurasia and Greenland by about $-1.5°C$ and along the Antarctic continent by about $-1°C$. Annual warming of about $+2°C$ is depicted over south of North Africa between $10-20°N$ and over the India and part of Tibetan Plateau.

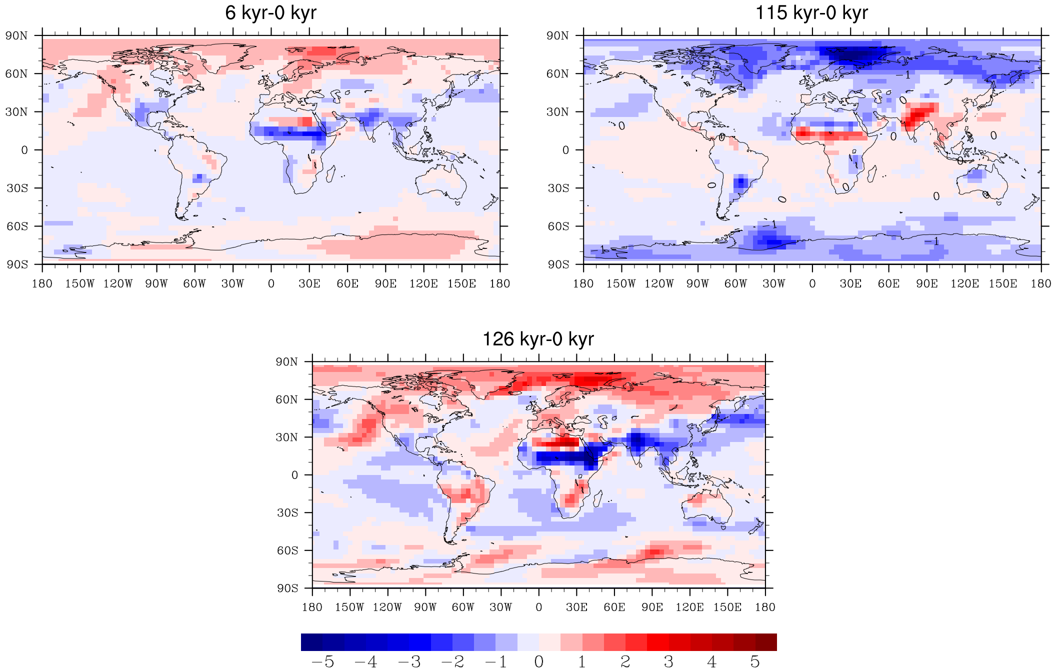

Figure 4.2— Difference of annual average 2m air temperature [$°C$] between the 6ky, 115ky, 126ky and CTRL simulations.

Precipitation

The summer warming in 6 kyr and 126 kyr over the Northern Hemisphere continents reached maximum in central Asia and North Africa compared to the pre-industrial conditions (App.A.1). The increased land-sea temperature contrast strengthens the low-level convergence and upward motion in the African-Asian monsoon region. This results in enhancement of the low-level moisturized wind and an increase in precipitation in Sahel, East Africa, southern Arabia, India and China (with amplification in 126 kyr) (App.B.1). In DJF in 6 kyr and 126 kyr, the Southern Hemisphere continents are cooler compared to the CTRL simulation. This leads to a weakening of convective activity and results in less precipitation in southern Africa, the north of South America, northern Australia and Indonesia (with amplification in 126 kyr). The increased seasonality of insolation in the Northern Hemisphere in 6 kyr and 126 kyr lead to a shift northward of intertropical Convergence Zone (ITCZ) and associated rainfall maximum (Fig.4.3, left column).

Oppositely, 115 kyr is characterized by a weakening of summer monsoons in the north of the Sahel region, northern Arabia and northern India (in African-Asian region) due to cooling over the continents and a reduction of the land-ocean temperatire gradient. While warming over the Southern Hemisphere continents in DJF increases convections and results in wetter conditions in southern Africa, South America and Australia. Intertropical Convergence Zone (ITCZ) and associated rainfall maxima move southward (Fig.4.3, left column).

Annual mean precipitation over the Antarctic continent is slightly higher in 6 kyr and 126 kyr and slightly weaker in 115 kyr (Fig.4.3, right column). However, a seasonal analysis shows less precipitation over Antarctica in JJA and SON in 6 kyr and 126 kyr (Fig.C.1).

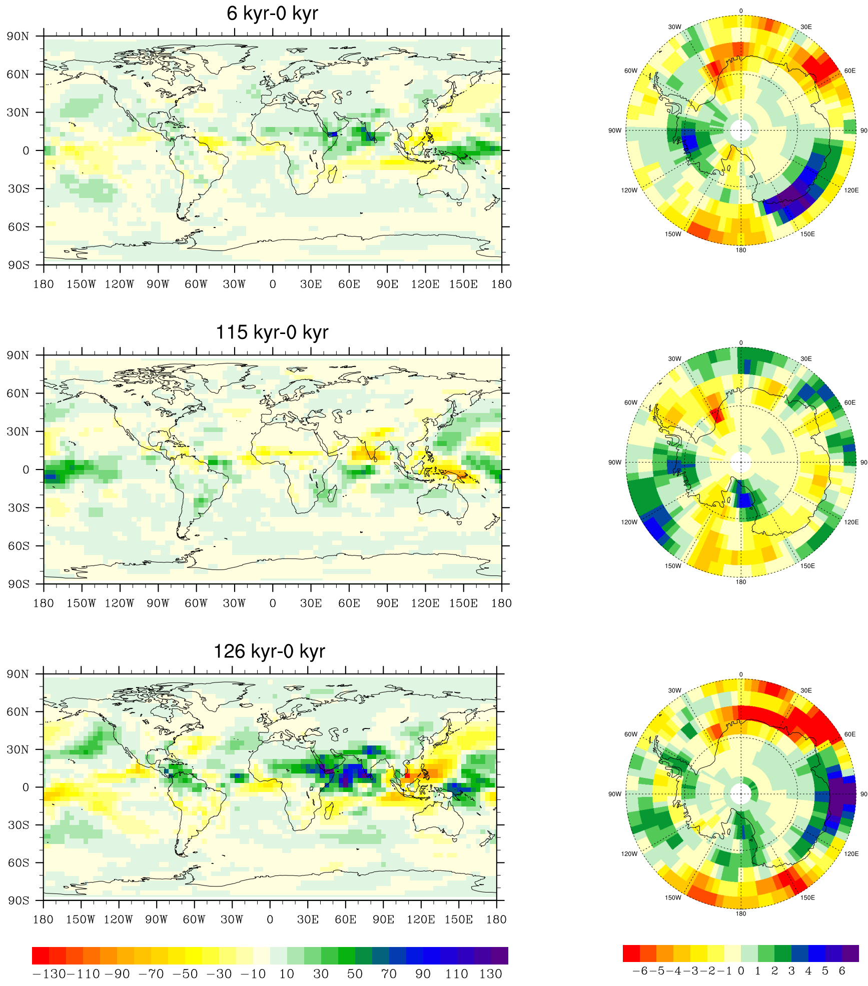

Figure 4.3— Difference of annual average global precipitation (left column) and precipitation over Antarctica (right column) $[mm/month]$ between the 6ky, 115ky, 126ky and CTRL simulations.

Circulation

Dust transport can be schematically divided into transport by the time-mean circulation and transport caused by nonlinear dependence of dust concentration and wind velocity, i.e. time-varying circulation. The latter is in high- and mid-latitudes dominated by synoptic variability. Time-varying transport we will call eddy transport. Fig.4.4 shows total transport of dust at pressure level of 500 hPa, consisted of both time-mean circulation and eddy transport. The time-mean circulation over the Southern Ocean in different time-slices is quite similar. Thus, eddy contribution to the transport towards Antarctica is significant. In 6 kyr, the modification of the southward transport pathways can be seen over the Weddell Sea (Fig.4.4). In 126 kyr, the main modification occurs in the Indian sector of the Southern Ocean.

The simulated cyclonic activity over the Southern Hemisphere for different time-slices is shown in Fig.4.5. In 6 kyr and 126 kyr, the annual average cyclonic activity is generally reduced over the Southern Ocean and shifted equatorward, except for the west of the Pacific sector. The main contribution to the annual reduction of cyclonic activity in both time-slices is a strong weakening of cyclones in MAM (App.D.1). In JJA cyclonic activity is somewhat enhanced with a clear equatorward shift. Annual cyclonic activity in 115 kyr shows a slight increase over most parts of the Southern Ocean and a slight poleward shift (Fig.4.5). These features of the atmospheric circulation are important for the transport of dust towards Antarctica, which will be discussed further in section 4.1.6.

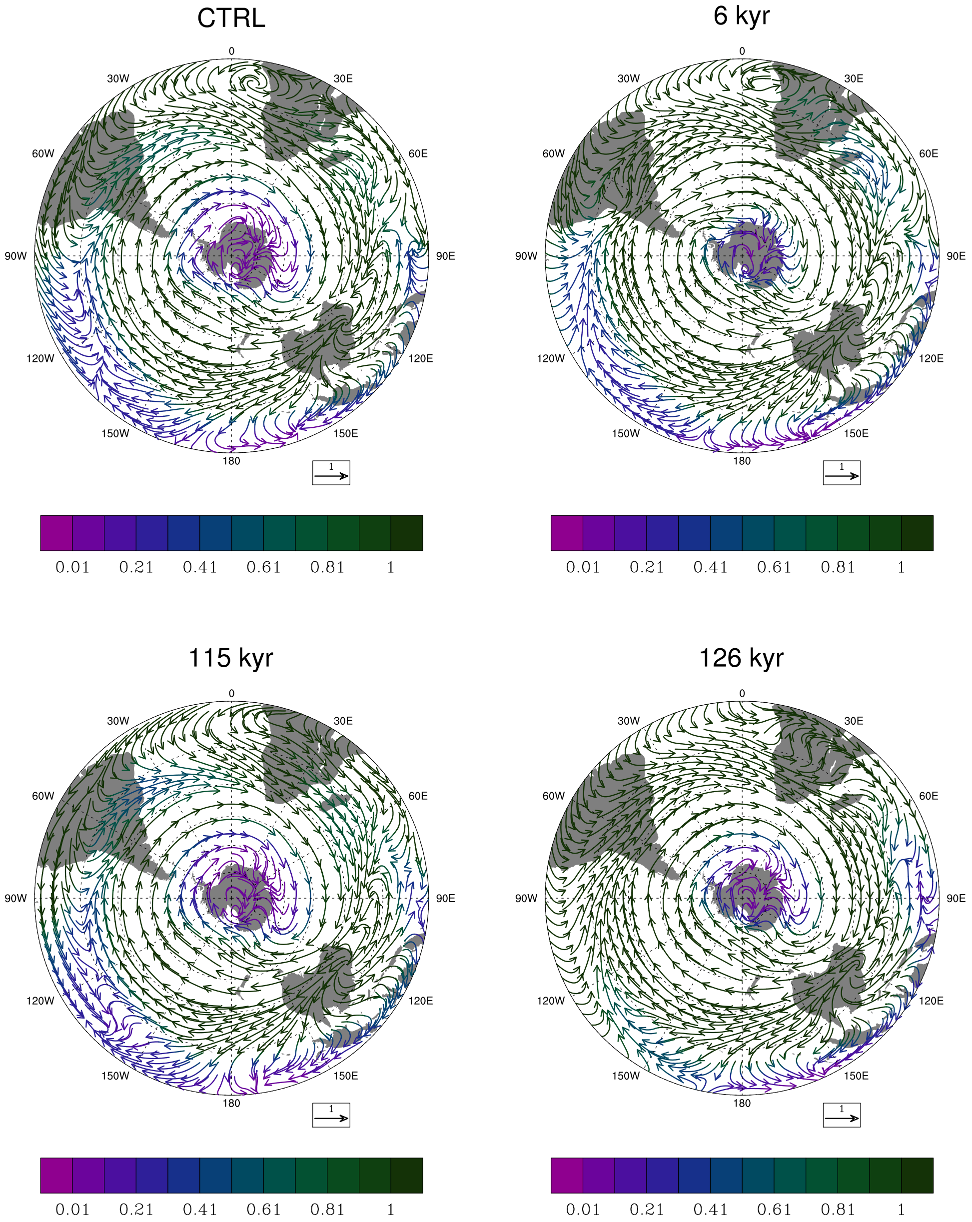

Figure 4.4— Mean dust transport at pressure level of 500 hPa for the interglacial time-slices.

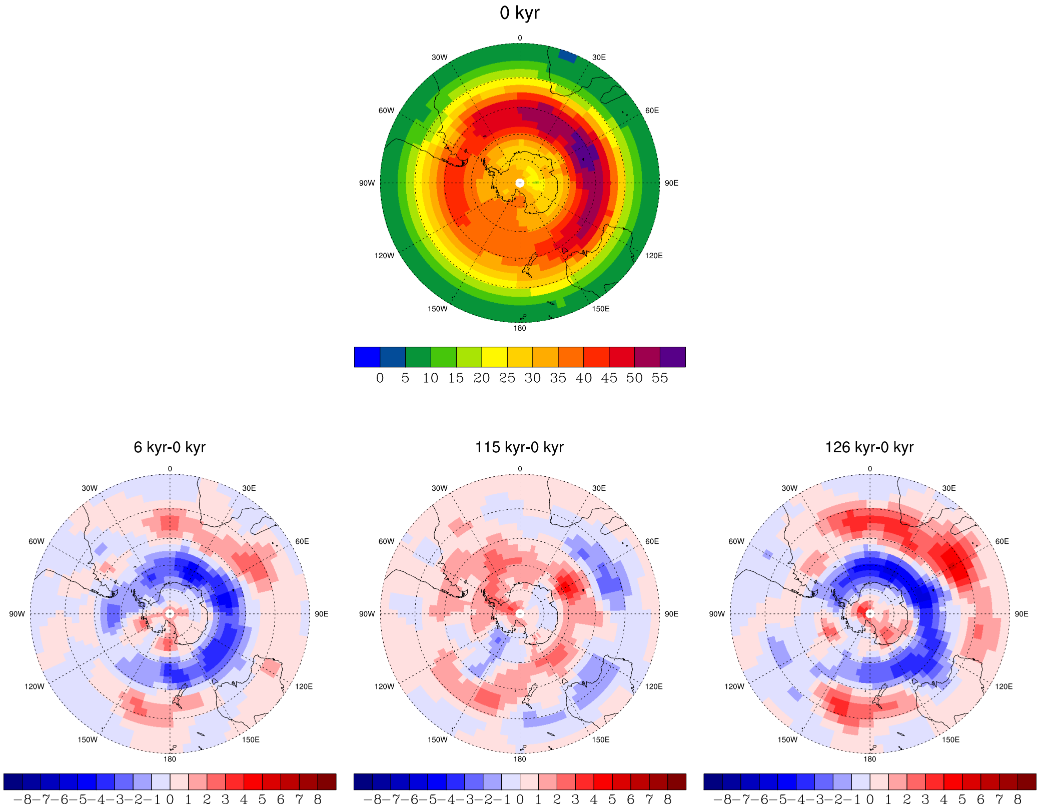

Figure 4.5— Standard deviation of 500 hPa height $[m]$ (annual mean), due to transient eddies in the bandpass regime from 2.5 to 6 days over the Southern Hemisphere shown for the CTRL simulation (top) and as a difference between 6 kyr, 115 kyr, 126 kyr and CTRL.

4.1.3 Global dust budget

The 20-year mean dust budget for the pre-industrial and three last interglacial time-slice simulations are shown in Table 4.3. The global mean load of mineral dust increases from CTRL to 126 kyr consistently with the dust emissions. The lifetime slightly varies between 4.7 days for the CTRL run and 4.1-4.4 days for past interglacial time-slices.

Table 4.3— Global mass budget for the interglacial time-slice simulations.

	CTRL	6 kyr	115 kyr	126 kyr
Emissions, $[Tg/yr]$				
Total	1540 (100%)	1951 (100%)	1898 (100%)	2385 (100%)
Sahara	559 (36%)	531 (27%)	741 (39%)	844 (35%)
Southern Hemisphere	62.2 (4.0%)	156.8 (8.0%)	65.0 (3.4%)	112.1 (4.7%)
Australia	60.0 (3.9%)	108.6 (5.6%)	62.6 (3.3%)	110.2 (4.6%)
South America	1.0 (0.06%)	47.0 (2.4%)	1.2 (0.06%)	1.2 (0.05%)
South Africa	1.2 (0.08%)	1.1 (0.06%)	1.1 (0.06%)	0.8 (0.03%)
Deposition, $[Tg/yr]$				
Total deposition	1539 (100%)	1952 (100%)	1896 (100%)	2376 (100%)
Wet deposition	643 (42%)	811 (42%)	790 (42%)	1123 (47%)
Dry deposition	214 (14%)	302 (15%)	239 (13%)	363 (15%)
Sedimentation	682 (44%)	839 (43%)	867 (46%)	890 (37%)
Load, Tg	19.7	21.8	22.8	27.5
Lifetime, days	4.7	4.1	4.4	4.2

The distribution of annual mean dust lifetime for the Southern Hemisphere for different time-slices is shown in Fig.4.6. Residence time reflects the aerosol properties, as they depend on particle size and solubility, but also the model-specific parameterizations of aerosol processes. In addition they reflect the spatial distributions of aerosols in conjuction with those of relative humidity, precipitation, and surface properties (Textor et al., 2006). One way to explain changes in dust lifetime is in terms of precipitation difference. In 6 kyr the decrease/slight increase of lifetime over the Southern Ocean and Antarctica is likely associated with the increase/slight decrease of precipitation over the ocean south of $40°S$ (Fig.4.7 and App.B.1) in DJF/SON, when dust emissions are strongest (see section 4.1.4). In 126 kyr the general decrease of dust lifetime over the Southern Ocean and Antarctica is caused by the slight increase of precipitation over the ocean south of $40°S$ in DJF and SON. In 115 kyr the changes relative to CTRL are rather small.

The annual cycle of the globally averaged emission flux and dust load for different time-slices are shown in Fig.4.8. The global emissions are strongest in boreal spring (MAM) and are dominated by the Saharan and Asian dust sources in all interglacial

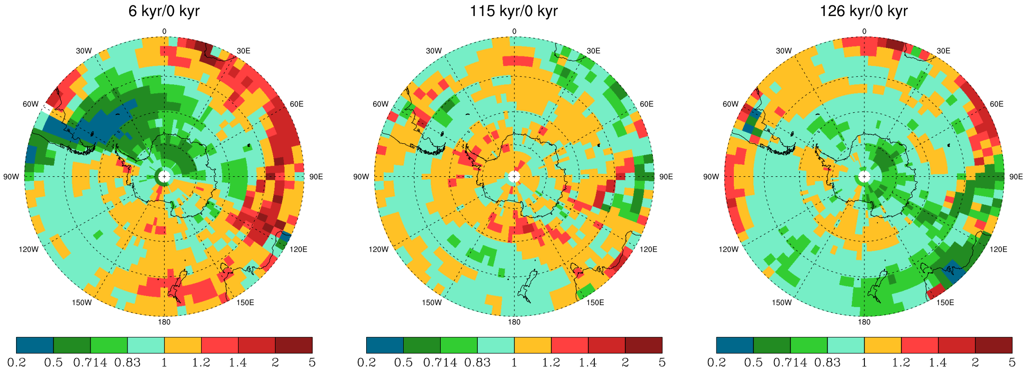

Figure 4.6— Dust atmospheric lifetime $[days]$, calculated as a ratio between dust load and deposition. Figure shows past interglacials to pre-industrial ratio.

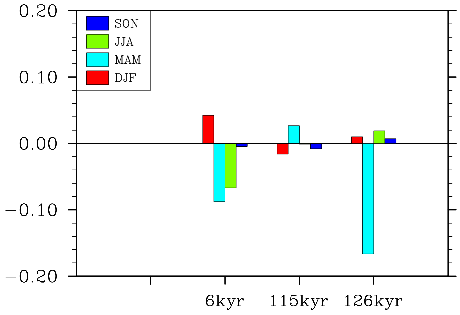

Figure 4.7— Difference in precipitation averaged over the ocean south of $40°$ S, interglatials minus pre-industrial values.

time-slices with the exception for 126 kyr, which has the highest activity from April through July. The strong emissions in JJA in 126 kyr are caused by the strengthening of the African monsoon activity due to very high temperature over the land and increased land-ocean temperature gradient. The monthly mean dust load is generally correlated with corresponding dust emissions for all interglacial time-intervals. The feature of dust burden in 126 kyr is a prominent buildup of dust load during the summer months. The summer emissions from Asian and Saharan dust sources are much higher than emissions removed by precipitation in these regions, although wet removal is increased in 126 kyr compared to CTRL. For example, strong monsoonal activity over the Saharan region in JJA in 126 kyr induces heavy precipitation and leads to high wet removal which might reduce the lifetime of dust particles and consequently dust burden. But this is not the case for the Saharan region, as the precipitation in 126 kyr is high over east of the Sahel region and the burden over the western Sahara remains high.

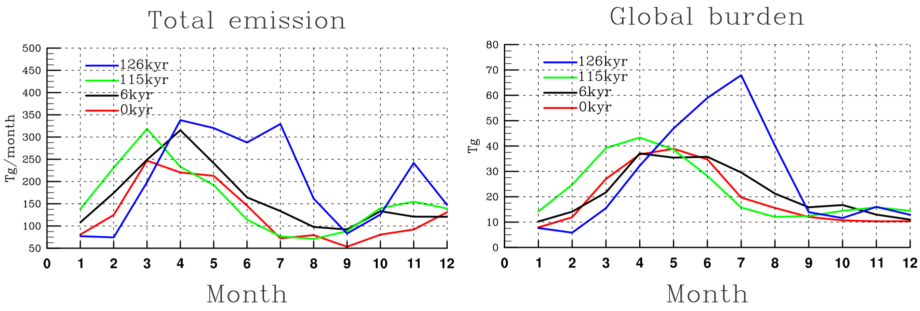

Figure 4.8— Globally averaged annual cycle of dust emissions $[Tg/month]$ and load $[Tg]$ for the interglacial time-slices.

Similar plots but for the Southern Hemisphere only are shown in Fig.4.9. Southern Hemisphere dust emissions are strong from October through January for all interglacial time-slices. Details of the seasonal variation of Southern Hemisphere dust emission are discussed in the section 4.1.4.

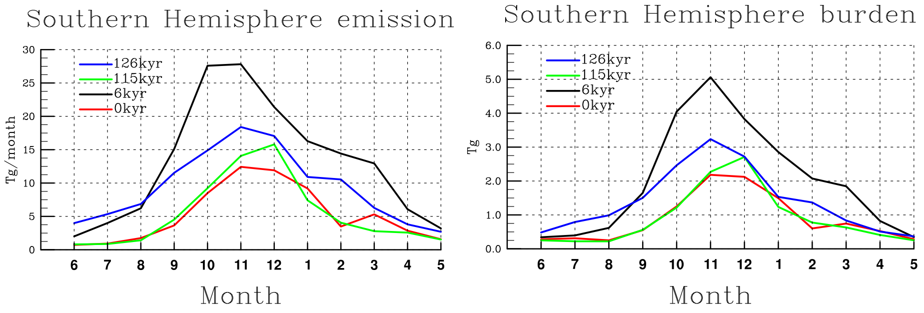

Figure 4.9— Annual cycle of dust emissions $[Tg/month]$ and load $[Tg]$ averaged over the Southern Hemisphere for the interglacial time-slices.

The dust burden over the Southern Hemisphere is consistent with the corresponding dust emissions for all interglacial time-slices.

4.1.4 Dust emission

The simulated global mean dust emission increases from 1540 Tg/yr for CTRL to 2385 Tg/yr for 126 kyr (Table 4.3). For all paleo time-slice simulations the global emissions are dominated by the Northern Hemispere dust sources. Dust emissions from the Southern Hemisphere contribute less than 10% to the global emissions and are the main sources of dust deposited in Antarctica. The mass of dust that reaches Antarctica is about 2-3 orders of magnitudes smaller than the mass of dust mobilized from the Southern Hemisphere dust sources. Southern Hemisphere dust emissions are dominated by the Australian dust source.

In our simulations, dust emissions in different time-slices depend on dust source area extent, 10 meter wind speed, soil moisture and snow cover, which change with different climate conditions. Other parameters for the calculation of dust emissions such as topography, surface roughness and soil types remain similar to pre-industrial. The dust source area extent is a function of vegetation (Fig.4.12, top) with a cover fraction less than or equal to 25% (see details in section 2.2.6). The source area extent in number of grid boxes for different time-slices is shown in Table 4.4.

Table 4.4— Dust surce area extent for the interglacial time-slice simulations.

	CTRL	6 kyr	115 kyr	126 kyr
Source area, [grid boxes]				
Australia	14	7	8	25
South America	9	10	7	9
Southern Africa	4	4	5	7
Σ	27	21	20	41

As a result of increased African-Asian summer monsoon in 6 kyr and 126 kyr, vegetation cover in Asian and west African regions increases in 126 kyr, but it is not recognizable in the 6 kyr simulation (Fig.4.12, top). At the same time, dryer conditions over some parts of the Southern Hemisphere continents reduced vegetation cover in Australia and southern Africa in 126 kyr. In 115 kyr, the weakening of summer monsoons in the northern Sahel region, extends the Saharan dust source, while wetter conditions over the Southern Hemisphere continents (Fig.4.3) lead to a reduction of the dust source areas in Australia and South America. Together with changes in dust source area extent the difference in 10 m wind speed is also highly important for dust mobilization. The annual probability density functions (PDF) of wind speed for different time-slice simulations are shown in Fig.4.10.

According to the simulations, the largest extention of the Southern Hemisphere dust source area is in 126 kyr (by 50% higher compared to CTRL) (Table 4.4; Fig.4.12, top). The main contributor to this extent is an increased Australian dust source area due to significant reduction of vegetation, resulting from drier austral summers in 126 kyr. This together with a slightly higher probability of high wind

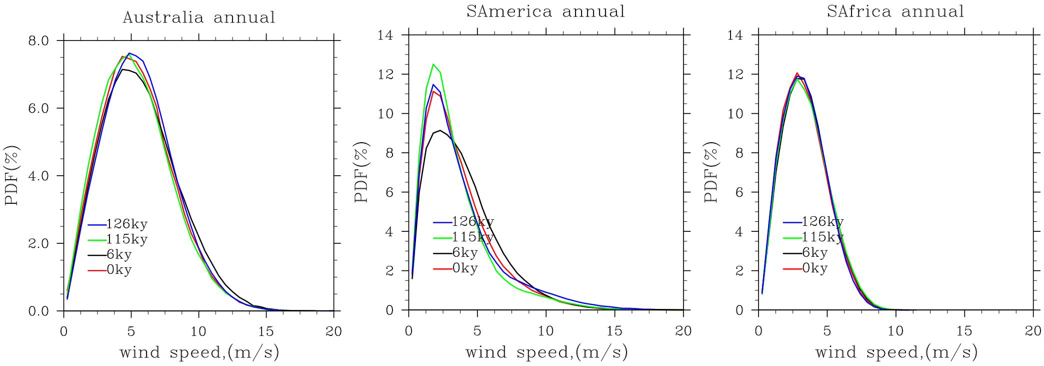

Figure 4.10— Annual PDF of wind speed calculated based on 20 years of 6 hourly data of 10 meter wind speed over the Australian, South American and south African dust source areas for the interglacial time-slices. Note that the extent of dust source areas differs in different time-slices.

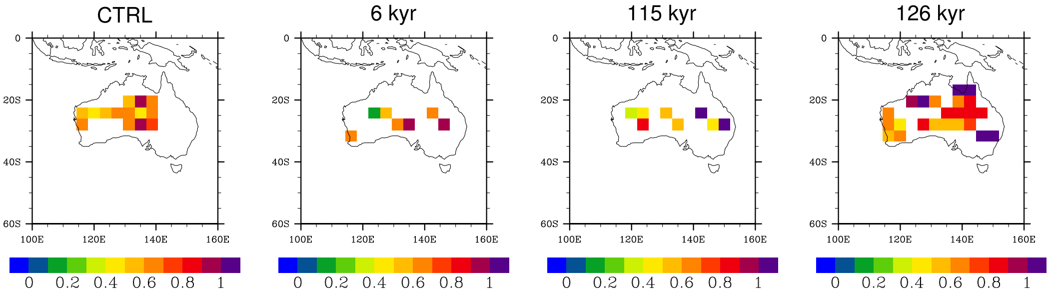

Figure 4.11— Typical soil wetness $[m]$ during dust emissions for Australian dust source area for the interglacial time-slices.

speed (compared to CTRL) results in an increase of emissions from the Australian source by about 46% (Table 4.3, Fig.4.12, bottom). On the other hand, in the 6 kyr simulation, Australian dust source area is half of the source area in the CTRL run. The increased mobilization of Australian dust in 6 kyr (also by about 45%), is caused by more frequent high wind speed, especially during Austral spring, compared to CTRL and other interglacial time-slices (Fig.4.10 and 4.15). Increased emissions in 6 kyr in the western part of Australia, are furthermore related to very low soil wetness (Fig.4.11).

The simulated emissions from the Southern Hemisphere dust source areas in 115 kyr are similar to those in the CTRL run. The Australian dust source area extent in 115 kyr decreases by almost half compared to the extent in CTRL. However dry soil in few grid boxes in western and eastern parts of the continent (Fig.4.11) in combination with an almost unchanged PDF of wind speed (to CTRL) result in emissions similar to CTRL.

The dust source areas and emissions in South America are persistent through all interglacial time-slices, except for a large increase of emissions in 6 kyr. This is due to very strong dust emissions from one particular grid box (Fig.4.12, bottom) with relatively high wind speed and relatively low soil wetness (Fig.4.13, middle and right columns). The dust emissions from the south African source are stable through all time-slices, consistently with the frequency of high wind speed (Fig.4.10).

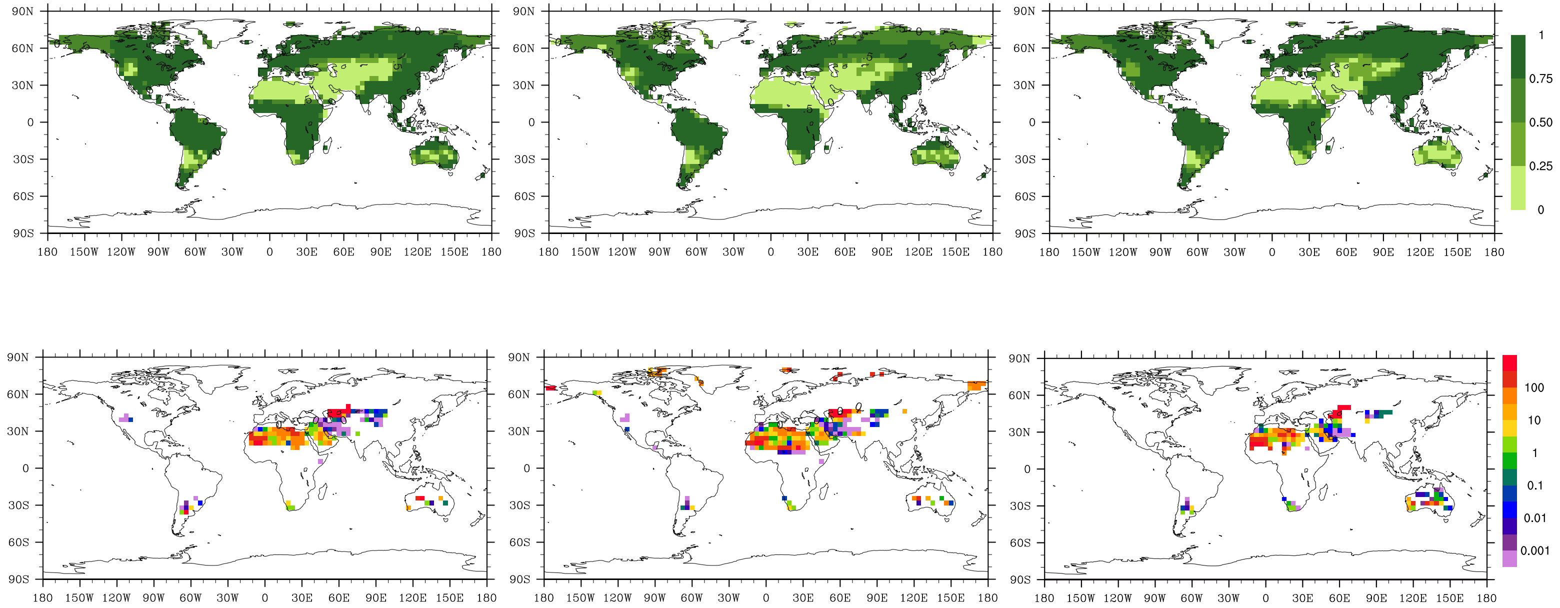

Figure 4.12— Annual maximum vegetation cover fraction obtained from the LPJ model for 6 kyr, 115 kyr and 126 kyr (top) and mean dust emission flux $[g/m^2/yr]$ for the corresponding time-slices (bottom).

Dust emissions as a function of wind speed and soil moisture

In this section, dust emissions as a function of wind speed and soil moisture are examined in more detail for the interglacial time-slices, as was done for the CTRL run in chapter 3.2.2. A comparison of the results for all past interglacial time-slices with those in the CTRL run (Fig.3.2) shows a rather similar dust emission distribution as a function of wind speed for the Australian and south African dust sources. In Australia most emissions are mobilized at wind speeds of about 9-13 m/s for 6 kyr and 115 kyr and 9-14 m/s for 126 kyr. In southern Africa the highest emissions occur with slightly lower wind speeds of 7-9 m/s for 6 kyr and 115 kyr and 7-10 m/s for 126 kyr (not shown).

For South America the distribution of dust emissions with respect to wind speed shows considerable differences between the individual time-slices. As discussed before, the distribution of emissions for the pre-industrial simulation shows two peaks Fig.3.2). At 6 kyr dust emissions at wind speeds of 10-16 m/s are substantially increased and the distribution of dust emissions seems to have only one peak. The emission at given wind speed is enhanced from one particular grid box ($\sim 35°S, 65°W$) with relatively high wind speed and relatively low soil wetness (Fig.4.13, middle and right columns). The PDF of high wind speed of 17-23 m/s in 6ky is broadly similar to those in CTRL.

For 115 kyr the distribution of emissions as function of wind speed shows only one peak as well, but at high wind speeds between 18 and 23 m/s. Dust mobilization at low wind speeds does not contribute substantially to the total dust mobilization.

The distribution of dust emission mass flux as a function of wind speed at 126 kyr is relatively similar to CTRL and has two peaks as well. The high wind speed peak is relatively similar, but the low wind speed peak is shifted towards even lower wind speeds. Maximal emissions occur between 8 and 9 m/s from grid points with relative low soil wetness. At 126 kyr the likelihood of high wind speeds is enhanced compared to CTRL (Fig.4.10).

In the model, strong wind speed is only effective for dust mobilization, if the relative soil moisture, defined as ratio of soil wetness to field capacity of soil, is less than 0.99. Otherwise dust emission is not possible.

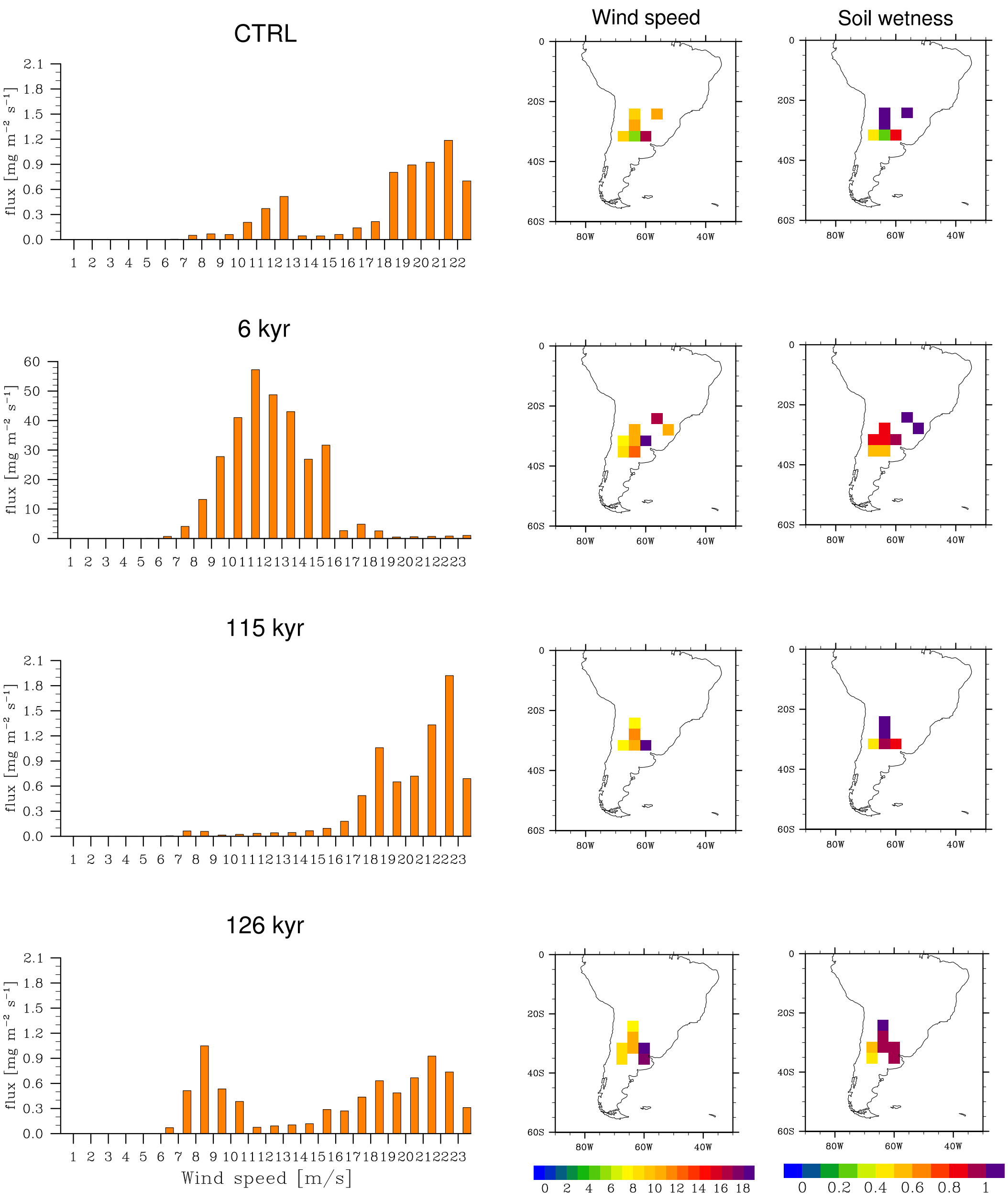

Figure 4.13— Distribution of the dust emission mass flux as a function of wind speed over the south American dust source for CTRL, 6 kyr, 115 kyr and 126 kyr (left column). The computation is based on 6 hour data for wind bins defined as 0-1, 1-2, 2-3, ... [m/s] for 20 years of each simulation. Typical wind speed [m/s] (middle column) and soil wetness [m] (right column) during dust emissions from the South American dust source.

Seasonal variability of Southern Hemisphere dust emissions

The seasonal distribution of dust emissions from the Australian, south African and South American sources, together with the PDF of wind speed calculated over these regions for the interglacial intervals are shown in Fig.4.14 and Fig.4.15 respectively. The Southern Hemisphere dust sources are more productive in austral spring (SON) and austral summer (DJF) for all interglacial time-slices.

The main difference to CTRL is an increase of dust emissions in SON/JJA in 6 kyr and in JJA in 126 kyr from all Southern Hemisphere dust sources. This is the result of an increase in wind speed in the corresponding months, caused by reduced seasonality in the Southern Hemisphere in 6 kyr and 126 kyr, which is consequence of the perehelion shift to September in 6 kyr and to July in 126 kyr.

In the 115 kyr simulation the seasonal variability of emissions from each of the Southern Hemisphere dust sources is similar to the CTRL run. The warming of the Southern Hemisphere land masses in austral summer (DJF) due to shift of the perihelion to January leads to an increased temperature contrast between land and ocean and therefore increased Southern Hemisphere monsoons. This results in a slight increase of dust emissions from all Southern Hemisphere dust sources in the austral summer.

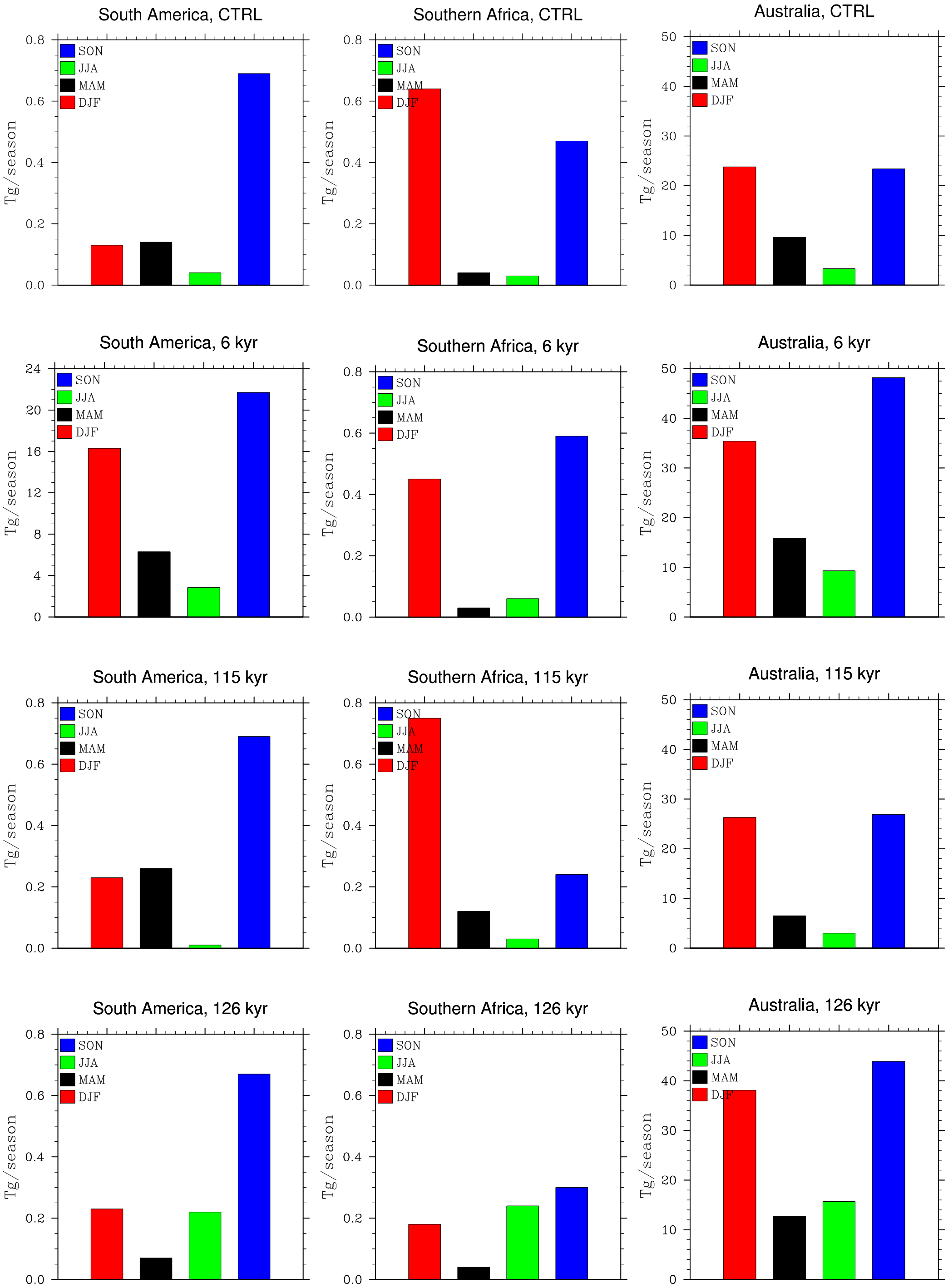

Figure 4.14— Seasonal cycle of dust emissions for the South American, south African and Australian dust sources for the CTRL (first row), 6 kyr (second row), 115 kyr (third row) and 126 kyr (fourth row) simulations. Note that scales are different.

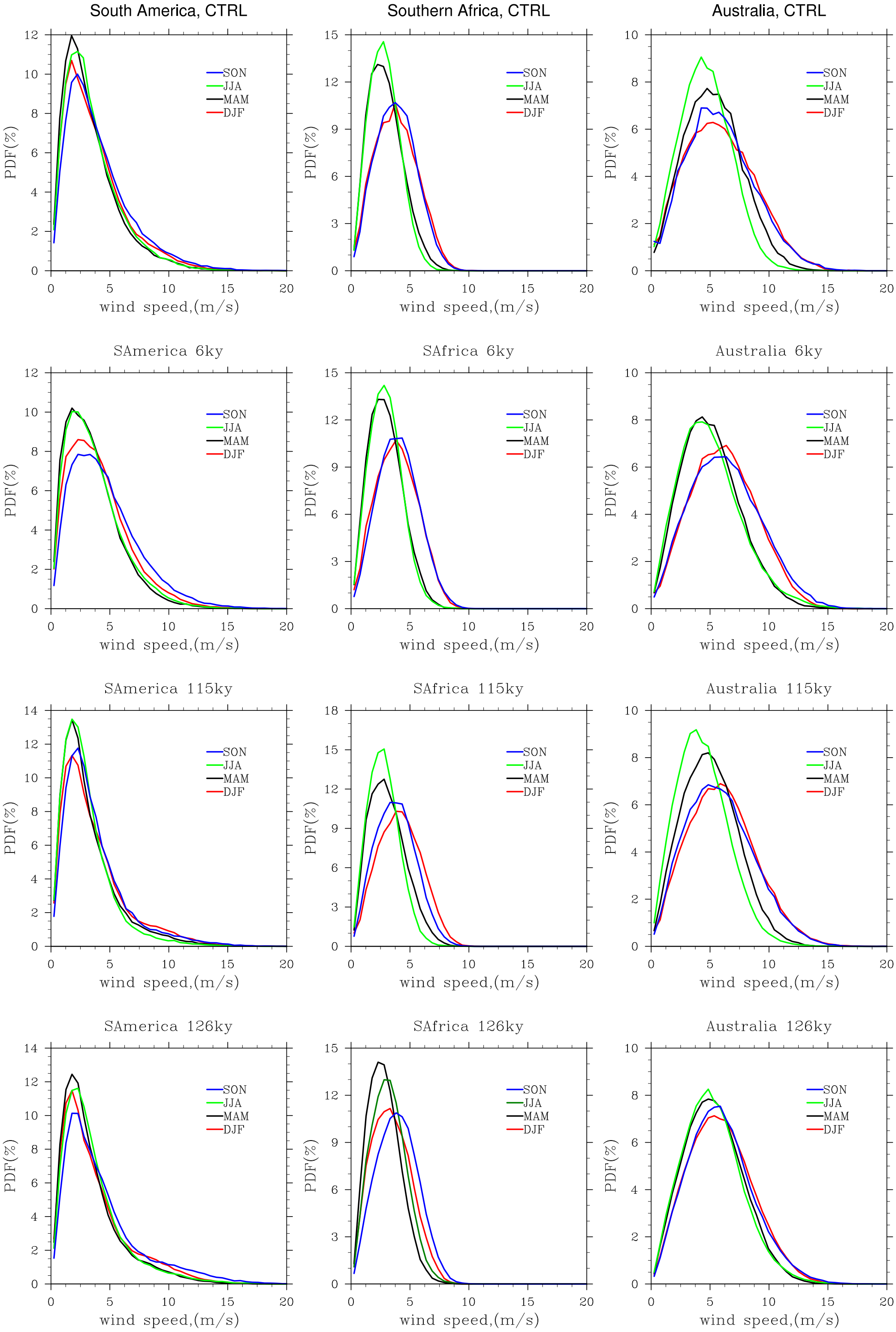

Figure 4.15— Seasonal cycle of probability density function of wind speed over the South American, south African and Australian dust sources for the CTRL (first row), 6 kyr (second row), 115 kyr (third row) and 126 kyr (fourth row) simulations. Note that scales are different.

4.1.5 Dust deposition

Simulated global mean dust deposition is higher by a factor of 1.3 in 6 kyr, by a factor of 1.2 in 115 kyr and by a factor of 1.5 in 126 kyr compared to CTRL (Table 4.3.) In all interglacial time-slice simulations, sedimentation and wet deposition are the main global loss processes of mineral dust. Each accounting for more than 40% of the total dust removal, except for 126 kyr. In 126 kyr the relative contribution of sedimentation to the total sink is weaker, due to increased tropical monsoonal activity and consequently wet deposition close to the main dust source regions in Asia and Sahara. Dry deposition is also a significant sink process, accounting for 14+-1% of dust removal in the interglacial time-slices.

Dust deposition integrated over Antarctica for the interglacial time-slice simulations is shown in Table 4.5.

Table 4.5— Dust deposition over Antarctica $[Tg/yr]$ for the interglacial time-slice simulations

	CTRL	6 kyr	115 kyr	126 kyr
Antarctica				
Total deposition	0.053 (100%)	0.2024 (100%)	0.0613 (100%)	0.1407 (100%)
Wet deposition	0.0477 (90.0%)	0.1785 (88.2%)	0.0549 (89.6%)	0.1266 (90.0%)
Dry deposition	0.0005 (0.9%)	0.0020 (1.0%)	0.0006 (1.0%)	0.0015 (1.1%)
Sedimentation	0.0048 (9.1%)	0.0219 (10.8%)	0.0058 (9.5%)	0.0127 (9.0%)

Over the Antarctic continent, wet deposition is by far the most important sink process for all interglacial time-slice simulations. Interestingly that in 6 kyr the relative contribution of wet deposition is decreased, while annual averaged precipitation over Antarctica is slightly increased. This is due to the features of precipitation distribution over Antarctica in the seasons of maximum dust deposition (SON and DJF in 6 kyr). Precipitation is decreased in 6 kyr SON over most coastal regions of Antarctica and in DJF partly over the Indian and west Pacific sectors of Antarctica (App.C.1). In 126 kyr the relative contribution of wet deposition is similar to CTRL, while precipitation over Antarctica is also increased. This results from the canceling effect of reduced precipitation in SON and increased precipitation in JJA over the Pacific sector of Antarctica, which is the area with maximum dust deposition (Fig.4.16). The relative contribution of wet deposition to the total deposition over Antarctica in 115 kyr is slightly reduced compared to CTRL due to the uniform decrease of precipitation over Antarctica in SON and partly decrease in DJF over Indian and Pacific sectors of Antarctica.

Simulated dust deposition over Antarctica is slightly larger in 115 kyr, and higher by a factor of 3.8 in 6 kyr and by a factor of 2.7 in 126 kyr with respect to the pre-industrial. However, Southern Hemisphere dust emissions for 6 kyr and 126 kyr increase by a factor of 2.5 and 1.8 respectively. Besides the emission increase, reduced precipitation over the Southern Ocean, as well as more vigorous atmospheric transport could lead to the increase of dust deposition in Antarctica. The factors that influence the variability of dust deposition in Antarctica in different time-slices are discussed in the next chapter 4.1.6. Additionally, the 6 kyr case is discussed in more detail in the discussion section 6.

Annual average dust deposition over the Southern Hemisphere for the interglacial time-slice simulations is shown in Fig.4.16. In all simulations the spatial distribution of dust deposition is higher in western than in the eastern Antarctica. The dust deposition in Antarctica is highest in the coastal area and decreases in the interior of the continent similar to the precipitation patterns.

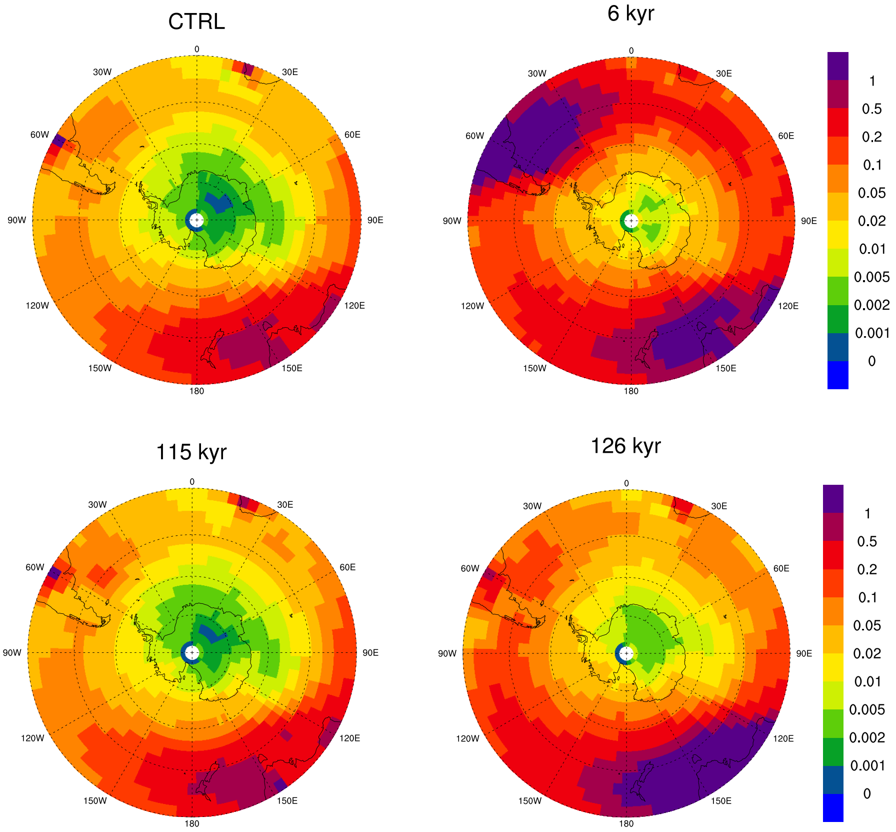

Figure 4.16— Annual average dust deposition $[\mu g/m^2]$ in the Southern Hemisphere for the interglacial time-slices.

4.1.6 Processes influencing dust deposition in Antarctica

One of the main processes, that influences dust deposition in Antarctica is atmospheric transport towards high southern latitudes. The air mass trajectories from the Southern Hemisphere dust sources to the Antarctic continent were calculated by using the method described in section 3.2.5 and results are shown in Tables 4.6 and 4.7. In order to consider atmospheric transport alone, without the influence of the dust source extent which is different in all simulations, the number of trajectories for each time-slice was divided by the total number of the Southern Hemisphere dust source grid boxes for the corresponding time-slice. Thus, the following discussion is based on the average number of trajectories originating over a single grid box and reaching Antarctica.

For all interglacial time-slice simulations, the number of trajectories originating over the Southern Hemisphere dust sources at the height of 800 hPa and reaching Antarctica is about 10% of the total number of trajectories (Table 4.6); and the number of trajectories originating at the height of 500 hPa and reaching Antarctica is about 3.5-5% (Table 4.7). Total low level- and middle troposphere transport towards Antarctica are similar for CTRL and 126 kyr, are slightly higher in 6 kyr and reache the highest values in 115 kyr, particularly in the middle troposphere. The increase of atmospheric transport in 115 kyr is due to enhanced cyclonic activity (Fig.4.5) and stronger zonal circulation over the Southern Ocean (not shown). This result is in agreement with Krinner and Genthon (2003), suggesting that the air mass transport towards Antarctica at 115 kyr is in a sense intermediate between the present and the LGM, showing signs of a more vigorous circumpolar circulation.

The atmospheric transport from the Southern Hemisphere dust sources towards Antarctica for all interglacial time-slices is more active in winter (JJA) and minimal in summer (DJF) for both the low- and middle troposphere. This implies that seasonality of atmospheric transport towards Antarctica and dust mobilization from Southern Hemisphere dust sources is out of phase. The seasonality of low level transport for all interglacial time-intervals is more pronounced compared to the middle troposphere.

For dust deposition in Antarctica the transport strength is most important for the seasons with largest Southern Hemisphere dust emissions, SON and DJF. Detailed analysis shows an increase of low- and middle troposphere transport in the corresponding seasons in 6 kyr and 126 kyr. This is due to southward deflection of the transport pathway over the Weddell Sea in 6 kyr and over the Indian sector of the Southern Ocean in 126 kyr (App.E.2) as well as due to increased cyclonic activity over the Pacific sector of the Southern Ocean in both time-slices in SON (App.D.1).

The contribution of each Southern Hemisphere dust source to the total number of trajectories shows that in 6 kyr and 115 kyr the fraction of the trajectories originating over Australia and South America and reaching Antarctica are similar to CTRL. Results show equal contribution of trajectories from both sources originating at 800 hPa and dominant South American trajectories originating at 500 hPa. Interestingly, the results show a slight increase in the contribution of south African trajectories at 115 kyr. In 126 kyr, the trajectories originating at the heights of 800 hPa, as well as 500 hPa, are dominated by the Australian dust source.

Due to large differences in dust source area extents in different time-slices it is also reasonable to analyze the total number of trajectories originating over the Southern Hemisphere dust sources (and not over a single grid box). The low- and middle troposphere transports towards Antarctica are maximal in 126 kyr due to the largest source area extent. Low level transport is weaker in 6 kyr and 115 kyr compared to CTRL and middle troposphere transport is similar in CTRL and 6 kyr and higher in 115 kyr (compared to CTRL).

In order to investigate which processes contribute to the increase of dust deposition in Antarctica in the different interglacial time-slices, changes in emissions, precipitation and transport are considered. The quantitative contribution of such processes as Southern Hemisphere dust emissions, atmospheric transport from the Southern Hemisphere dust sources to Antarctica, dust transport efficiency, precipitation over the ocean south of 40°S to deposition of mineral dust over Antarctica is combined in Fig.4.17. Atmospheric transport is shown here as a sum of average number of trajectories originating over a single grid box at the heights of 800 hPa and 500 hPa. Increased Southern Hemisphere emissions in 6 kyr and in 126 kyr, can explain just two thirds (Table 4.3) of increased dust deposition over Antarctica. Analysis of precipitation over the ocean south of 40°S for 6 kyr shows an increase in DJF and a slight decrease in SON (Fig.4.7). In 126 kyr, precipitation over the ocean south of 40°S is increased in DJF, SON and JJA. Total transport towards Antarctica suggest similar strength of the transport in 126 kyr and slightly more active transport in 6 kyr. The explanation for increased dust deposition over Antarctica can be found in the changes of transport strength in the seasons with the most active dust emissions, SON and DJF. Our results show an increase of low- and middle troposphere transport in SON and DJF in 6 kyr and 126 kyr, with particular increase of low level transport in DJF in 126 kyr, which is doubled compared to CTRL.

Table 4.6— Total number of trajectories originating at the height of 500 hPa and 800 hPa over the Southern Hemisphere dust sources and reaching Antarctica within 10 days for the CTRL and LGM simulations.

	CTRL	6 kyr	115 kyr	126 kyr
Number of trajectories originating over SH sources and reaching Antarctica				
DJF	979 (5.7%)	1124 (7.5%)	1074 (7.3%)	2911 (10.7%)
MAM	4391 (25.6%)	3694 (24.7%)	3867 (26.4%)	5974 (21.9%)
JJA	8234 (48.0%)	6757 (45.2%)	6187 (42.2%)	12840 (47.0%)
SON	3565 (20.8%)	3374 (22.6%)	3530 (24.1%)	5587 (20.5%)
Σ	17169 (8.7%)*	14949 (9.8%)*	14658 (10.0%)*	27312 (9.1%)*
Total number of trajectories originating over SH sources	197100	153300	146000	299300
Average number of trajectories originating over a single grid box and reaching Antarctica				
DJF	36.3	53.5	53.7	71.0
MAM	162.6	175.9	193.4	145.7
JJA	305.0	321.8	309.4	313.2
SON	132.0	160.7	176.5	136.3
Σ	636.0	711.9	733.0	666.2

* - Percentage is calculated relative to the total number of potential trajectories originating over the SH dust sources.

Table 4.7— Total number of trajectories originating at the height of 500 hPa and 800 hPa over the Southern Hemisphere dust sources and reaching Antarctica within 10 days for the CTRL and LGM simulations.

	CTRL	6 kyr	115 kyr	126 kyr
Trajectories that originating over SH sources and reaching Antarctica				
DJF	702 (10.3%)	805 (12.2%)	677 (9.2%)	1442 (13.7%)
MAM	2307 (33.9%)	1838 (27.9%)	2411 (32.8%)	2710 (25.8%)
JJA	2496 (36.7%)	2487 (37.7%)	2667 (36.3%)	4161 (39.6%)
SON	1301 (19.1%)	1459 (22.1%)	1601 (21.8%)	2184 (20.8%)
Σ	6806 (3.5%)*	6589 (4.3%)*	7356 (5.0%)*	10497 (3.5%)*
Total number of trajectories originating over SH sources	197100	153300	146000	299300
Average number of trajectories originating over a single grid box and reaching Antarctica				
DJF	26.0	38.3	33.9	35.2
MAM	85.4	87.5	120.6	66.1
JJA	92.4	118.4	133.4	101.5
SON	48.2	69.5	80.1	53.3
Σ	252.1	313.8	367.8	256.0

* - Percentage is calculated relative to the total number of potential trajectories originating over the SH dust sources.

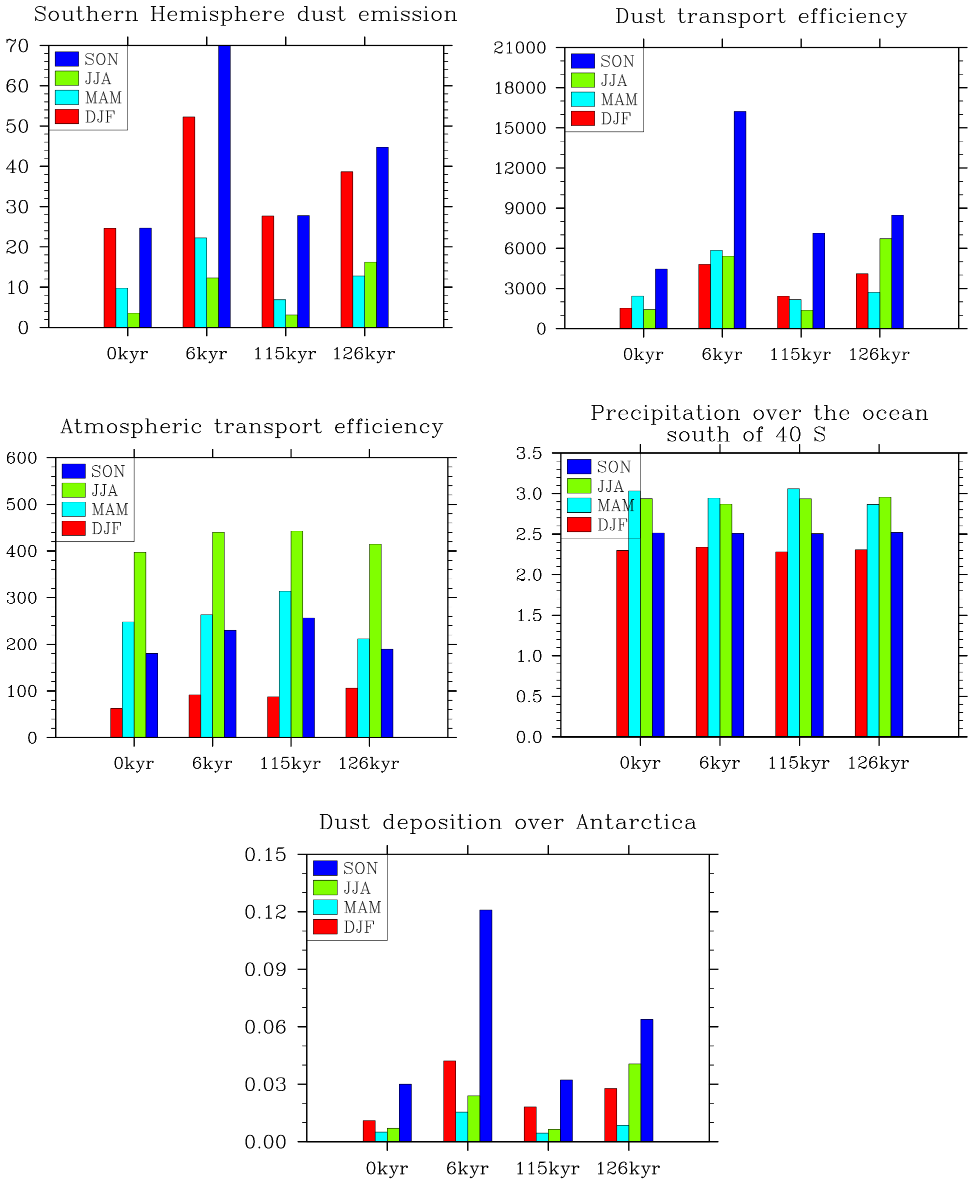

Figure 4.17— Impact of Southern Hemisphere dust emission $[Tg/season]$ (top left), atmospheric transport efficiency $[trajectories\,per\,season]$ (central left), the dust transport efficiency $[arbitrary\,units]$ (top right), precipitation over the ocean south of $40°$S $[mm/day]$ (central right) on dust deposition in Antarctica $[Tg/season]$ (bottom) for the interglacial simulations. Atmospheric transport efficiency is a sum of number of trajectories per season originated at 500 hPa and 800 hPa from a single dust source grid box and reached Antarctica within 10 days.

4.1.7 Atmospheric transport towards Antarctica

As mentioned above, SON and DJF are the seasons of maximal dust deposition in Antarctica. In the figure 4.18 the meridional dust flux over Antarctica for corresponding seasons for 6 kyr, 115 kyr and 126 kyr is shown. The pressure level of most effective dust transport towards Antarctica is similar for all interglacial time-slices and is a pressure levels of about 500 hPa (levels 10-12 dependent on the latitude). It can be seen that in 6 kyr the poleward transport of dust is slightly higher compared to CTRL and the near surface equatorward flux over the Antarctic continent is stronger but confined closer to the surface. In 115 kyr in DJF near surface equatorward flux over high southern latitudes is higher compared to CTRL.

The contribution of the synoptic scale eddies and other short-term processes (e.g. diurnal cycle) to the total transport can be seen in Fig.4.19. The short timescale processes contribute to poleward transport of dust with the exception for some near-surface values in the high southern latitudes in DJF (and MAM, not shown) in all time-slices. The katabatic component of the eddy flux over Antarctica is confined closer to the surface in DJF in 6 kyr and 126 kyr compared to CTRL. This is due to an increased Antarctica-Southern Ocean temperature gradient and the establishment of a more stable equatorward flow. Weaker equatorward component of the eddy flux over Antarctica in 115 kyr could mean lower wind speed and/or lower dust concentration. Since dust concentration in 115 kyr is slightly higher compared to CTRL, the weakening of the equatorward component of the eddy flux means reduced wind speed of eddy flux.

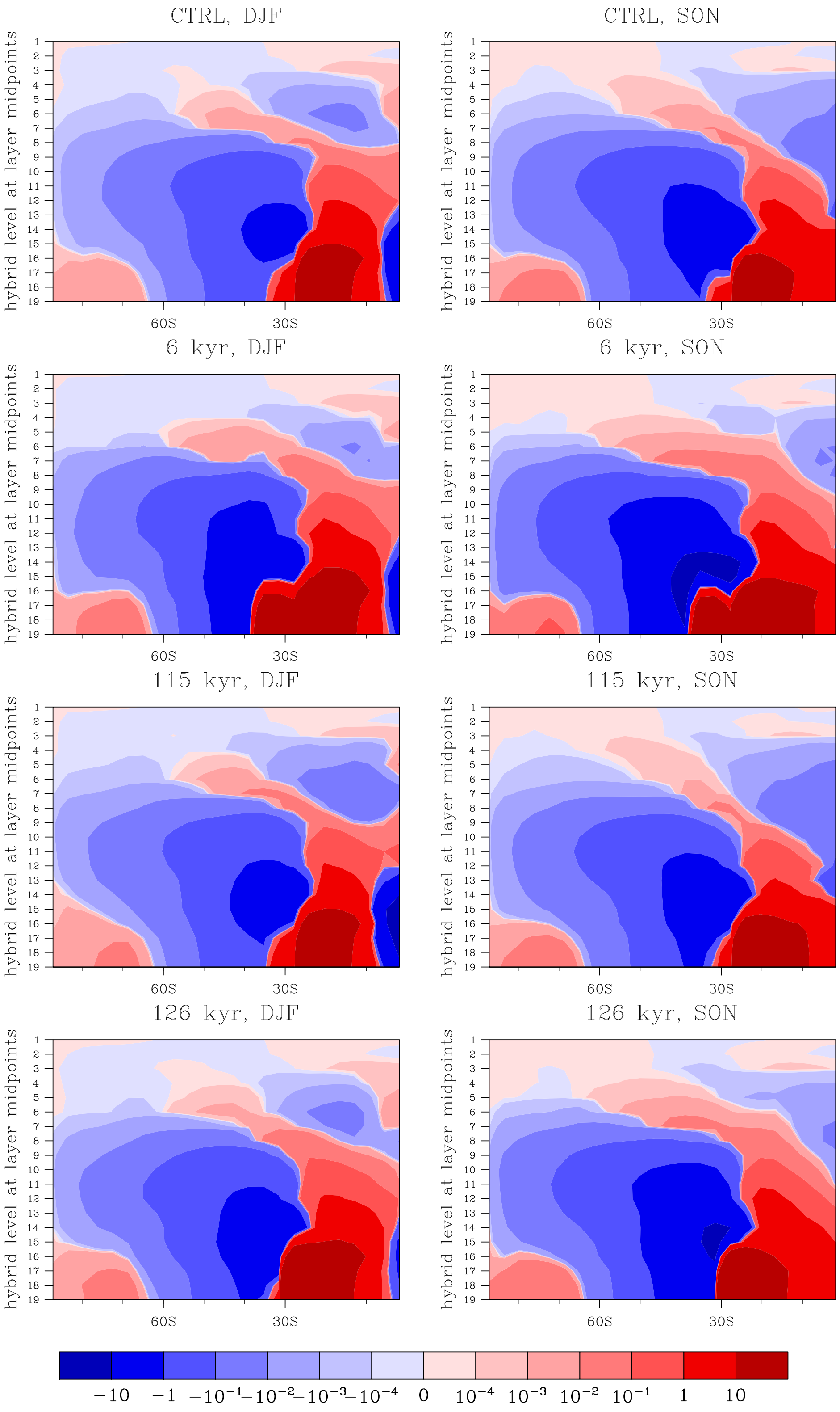

Figure 4.18— Seasonal mean zonal average meridional dust flux $[\mu g/m^2/s]$ over the Southern Hemisphere in DJF and SON for the interglacial time-slices. Positive values indicate equatorward transport.

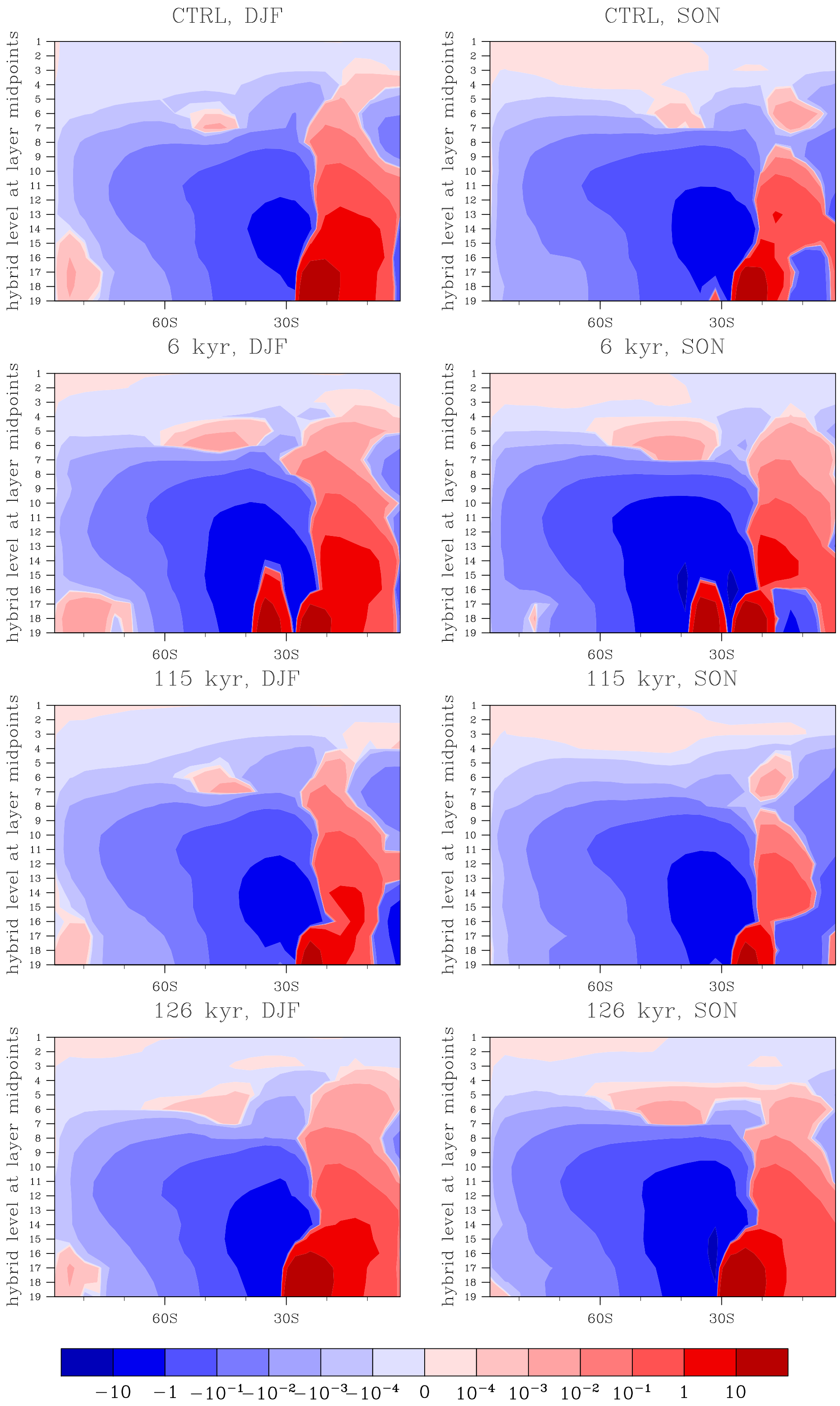

Figure 4.19— Seasonal mean zonal average synoptic scale eddy flux ($\overline{V \cdot DU} - \overline{V} \cdot \overline{DU}$) over the Southern Hemisphere for the interglacial time-slices.

4.2 Simulation of the dust cycle for glacial climate conditions

4.2.1 Experimental setup

A 20-year paleo-slice simulation after 5 years of spin up for the Last Glacial Maximum (LGM) climate conditions (21,000 years before present, hereafter 21 kyr) was performed.

The LGM and CTRL simulations differ in following characteristics:

1) Orbital parameters were modified following the PMIP2 protocol ($http://pmip2.lsce.ipsl.fr$, Braconnot et al., 2007) and listed in Table 4.8.

2) The atmospheric CO_2 concentration was reduced compared to pre-industrial conditions to a volume mixing ratio of 185 ppm following the PMIP2 protocol. Concentrations of the other greenhouse gases (CH_4 and N_2O) were also reduced compared to the CTRL simulation. Values are given in Table 4.9.

3) Sea-surface temperature, sea-ice concentration and surface background albedo were obtained from the long-term simulation by the coupled atmosphere-ocean-vegetation model ECHAM5/MPIOM/LPJ. Prescribed SST is lower by $-2.7°C$ (global average) and concentration of sea ice is higher in the LGM compared to the pre-industrial. Vegetation information was obtained from the dynamical vegetation model LPJ (for details see section 3.1).

For defining the topography and the land-sea mask, the 5 min data set of reconstruction of ice sheet topography from PMIP2 (Peltier, 2004), interpolated linearly to a T31 grid was used. Thereby, the global mean sea level is about 130 m lower during the LGM compared to the CTRL simulation.

Table 4.8— Orbital parameters for the CTRL and LGM simulations derived from PMIP2 protocol.

	CTRL	LGM
eccentricity	0.016724	0.018994
obliquity	23.446	22.949
longitude of perihelion	282.04	294.42

Table 4.9— Greenhouse gas concentrations for the CTRL and LGM simulations derived from PMIP2 protocol.

	CTRL	LGM
CO_2, [ppm]	280	185
CH_4, [ppm]	0.76	0.35
N_2O, [ppm]	0.27	0.20

4.2.2 Large-scale features of mean climate state

The Earth's orbital parameters (Table 4.8) and consequently insolation at the top of the atmosphere (Fig.4.20, left) do not differ significantly compared to pre-industrial conditions.

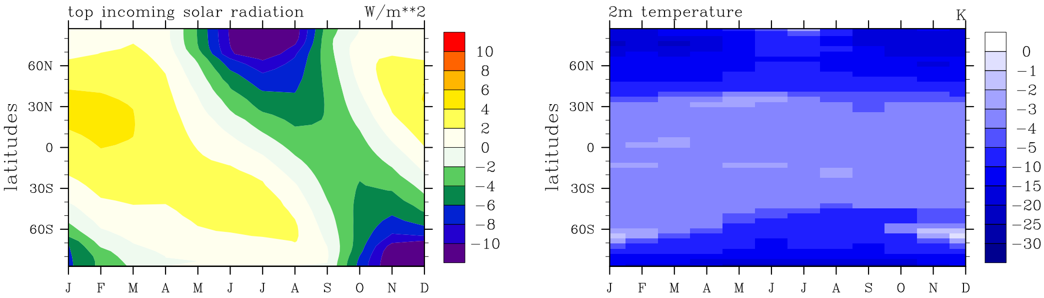

Figure 4.20— Difference of incoming solar radiation at top of the atmosphere $[W/m^2]$ (left) and 2m air temperature $[°C]$ (right) as a function of latitude and time of year between the LGM and CTRL simulations.

The high temperature response in the LGM (Fig.4.20, right) caused mainly by the reduced atmospheric CO_2 concentration compared to CTRL as well as the presence of massive ice sheets in the high Northern latitudes (Otto-Bliesner and Brady, 2005; Braconnot et al., 2007). In the LGM simulation the annual mean global cooling is about $-5.16°$C compared to the CTRL run. This value lies within the range of -3.6 to -5.7°C suggested by the PMIP2 simulations (Braconnot et al., 2007). The cooling is stronger at high latitudes in both hemispheres with particularly high anomalies in the areas occupied by ice sheets in the Northern Hemisphere (e.g. large cooling by about $-30°$ C in the north of northern America) (Fig. 4.21, left).

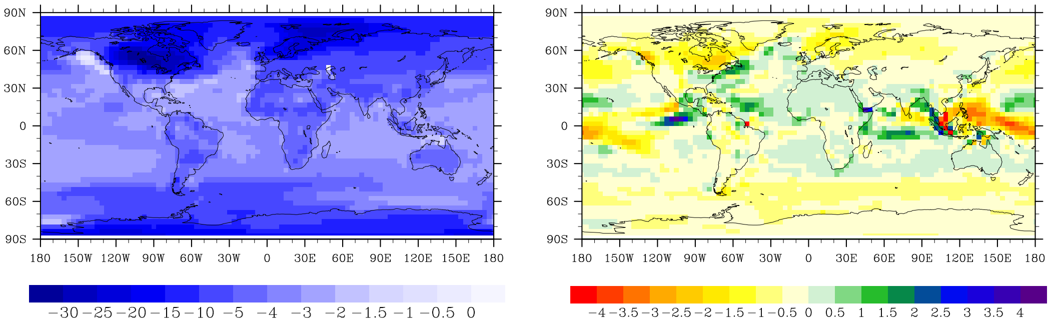

Figure 4.21— Difference of annual average 2m air temperature $[°C]$ (left) and precipitation $[mm/month]$ (right) between the LGM and CTRL simulations.

The LGM simulation is characterized by more arid climate (-1 to -4 mm/day

depending on the region) resulting from large-scale cooling and reduced evaporation (Braconnot et al., 2007). Precipitation is decreased over high- and most part of mid-latitudes in both hemispheres. However, higher precipitation occurs over most tropical and subtropical regions (Fig.4.21, left). Tropical parts of Indian and west Pacific ocean are affected by a southward shift of the intertropical convergence zone (ITCZ).

The simulated cyclone activity over the Southern Hemisphere, as a difference in standard deviation of 500 hPa height (m) due to transient eddies in the bandpass regime from 2.5 to 6 days between the LGM and CTRL simulations is shown in Fig.4.22 (right). Cyclone activity is somewhat enhanced and shifted equatorward. Over the Antarctic continent as well as over the Indian sector of Southern Ocean the cyclone activity is reduced.

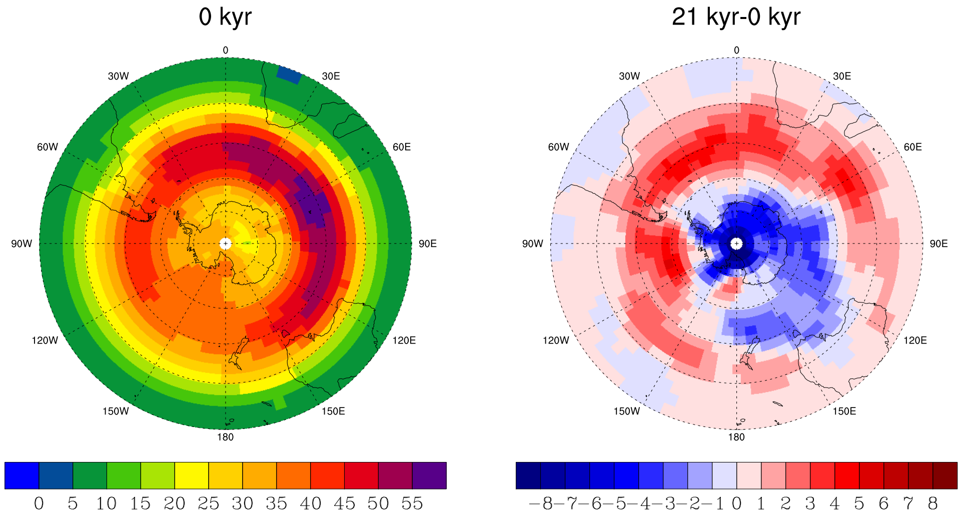

Figure 4.22— Standard deviation of 500 hPa height $[m]$ (annual mean), due to transient eddies in the bandpass regime from 2.5 to 6 days over the Southern Hemisphere shown for the CTRL simulation (left) and as a difference between the LGM and CTRL (right).

4.2.3 Global dust budget

The 20-year mean dust budget for the CTRL and LGM simulations are shown in Table 4.10. The average load of mineral dust increases by a factor of 1.6 for the LGM compared to CTRL. The mean lifetime of the dust in the atmosphere shortens from 4.7 days for pre-industrial to 3.7 days for glacial climate conditions. This is presumably due to the fact that the dust sources in the LGM are extended to the regions with high precipitation. For example the stronger and more extended Asian dust source is subject to a greater influence of wet conditions in mid-latitude, similar to the Patagonian dust source in the Southern Hemisphere. The lifetime due to wet deposition alone is 11 days in CTRL, while it is reduced to 9.0 days in the LGM, similar to previous studies (Mahowald et al., 1999).

Table 4.10— Global mass budget for the CTRL and LGM simulations

	CTRL	LGM
Emissions, $[Tg/yr]$		
Total	1540 (100%)	3106 (100%)
Sahara	559 (36%)	759 (24%)
Southern Hemisphere	62 (4%)	160 (5%)
Australia	60 (3.9%)	84 (2.7%)
South America	1 (0.06%)	75 (2.4%)
South Africa	1.2 (0.08%)	1.6 (0.05%)
Deposition, $[Tg/yr]$		
Total deposition	1539 (100%)	3119 (100%)
Wet deposition	643 (42%)	1293 (41%)
Dry deposition	214 (14%)	456 (15%)
Sedimentation	682 (44%)	1370 (44%)
Load, Tg	19.7	31.9
Lifetime, days	4.7	3.7

The distribution of the annual mean dust lifetime for the Southern Hemisphere (Fig.4.23) shows a slight increase of dust lifetime over the Pacific sector of the Southern Ocean possibly due to reduced precipitation. Dust lifetime over most part of Antarctica is reduced (similar to Albani et al., 2011), likely owing to higher concentration of dust in low level, as a result of weaker wet removal, and therefore faster sedimentation to the surface.

The annual cycle of the globally averaged emission flux and dust load for the CTRL and LGM simulations are shown in Fig.4.24. Global dust emissions in the LGM increase significantly from May to November compared to CTRL. The main contribution to this increase is the strengthening of the Asian and Saharan dust sources. This is the result of larger unvegetated areas, increased wind speed over

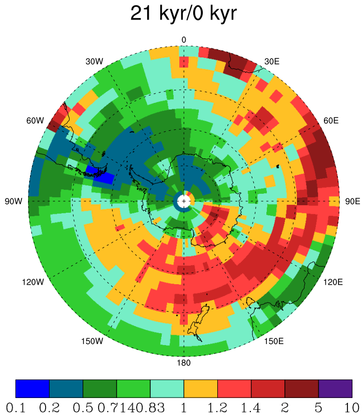

Figure 4.23— Dust atmospheric lifetime $[days]$, calculated as a ratio between dust load and deposition. Figure shows LGM to CTRL ratio.

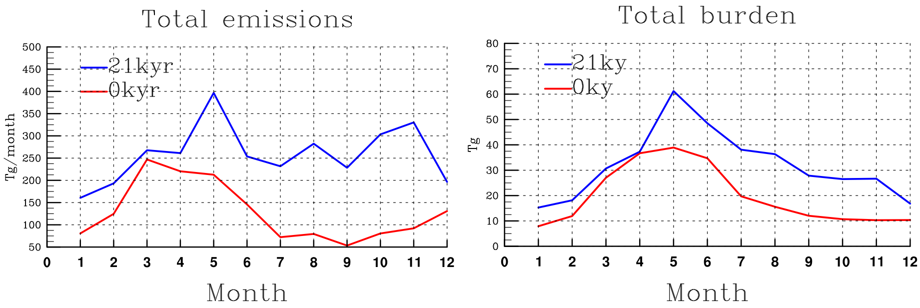

Figure 4.24— Globally averaged annual cycle of dust emissions $[Tg/month]$ and load $[Tg]$ for the CTRL and LGM simulations.

these areas in boreal summer and regionally decreased soil wetness. The dust burden in the LGM is maximal in May with subsequent subsidence till January. This inconsistency with dust emissions is explained by a strong wet removal of dust at high northern latitudes in boreal summer and over the western part of Eurasia in autumn.

Southern Hemisphere dust emissions in the LGM are highest from October through January with a distinct lowering of emissions in December (Fig.4.25). The dust load averaged over the Southern Hemisphere ($15 - 90°S$) is consistent with the corresponding dust emissions.

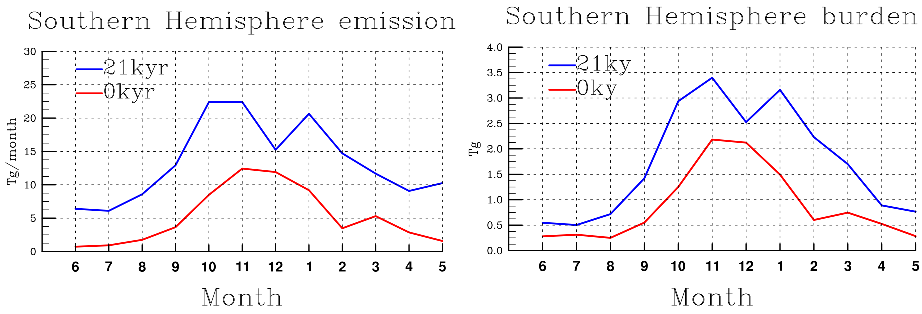

Figure 4.25— Annual cycle of dust emissions $[Tg/month]$ and load $[Tg]$ averaged over the Southern Hemisphere for the CTRL and LGM simulations.

4.2.4 Dust emission

Due to colder and drier climate in the LGM, unvegetated areas are significantly expanded compared to the pre-industrial (Fig.4.27, top). New source areas on the continental shelf are exposed due to lower sea levels at the LGM. The global dust emission increases by a factor of 2 for the LGM compared to the CTRL run and yields 3106 Tg/yr (Table 4.10). In the LGM, the Southern Hemisphere dust emission increases by a factor of 2.6, while the dust source area in the Southern Hemisphere is just 1.5 times larger than in the pre-industrial simulation (Table 4.11). Simulated Southern Hemisphere emissions mobilized from the pre-industrial dust source areas during the LGM are quite similar to those in the CTRL run. Thus, the additional dust source area which is formed in the LGM is more efficient for dust mobilization than the source area in the pre-industrial simulation. The main contributor to the increase of Southern Hemisphere emissions in the LGM is the significantly strengthened South American dust source. Increased emissions from South America are induced by not only an extended dust source area, but also by a much higher probability of high wind speed over this additional area (Fig.4.26). Furthermore increased emissions are also related to regionally reduced soil wetness and particularly dry soil in the "new" source in the south of Patagonia region (Fig.4.28, right column). In the LGM, the South American dust source is almost as strong as the Australian source. Emissions from the Australian dust source is slightly increased in the LGM compared to the pre-industrial time-slice due to an enlarged dust source area extent and regionally lower soil wetness, while the probability of high wind speed is similar to that in the CTRL run (Fig.4.26).

Table 4.11— Dust source area extent for the CTRL and LGM simulations

	CTRL	LGM
Source area, [grid boxes]		
Australia	14	22
South America	9	15
Southern Africa	4	4
Σ	27	41

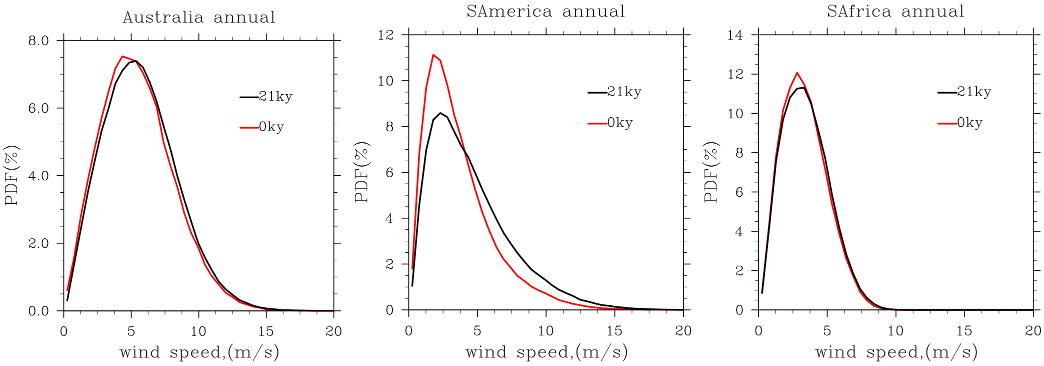

Figure 4.26— PDF of wind speed over the Australian, South American and south African dust source areas. Note that the extent of dust source areas differs in different time-slices.

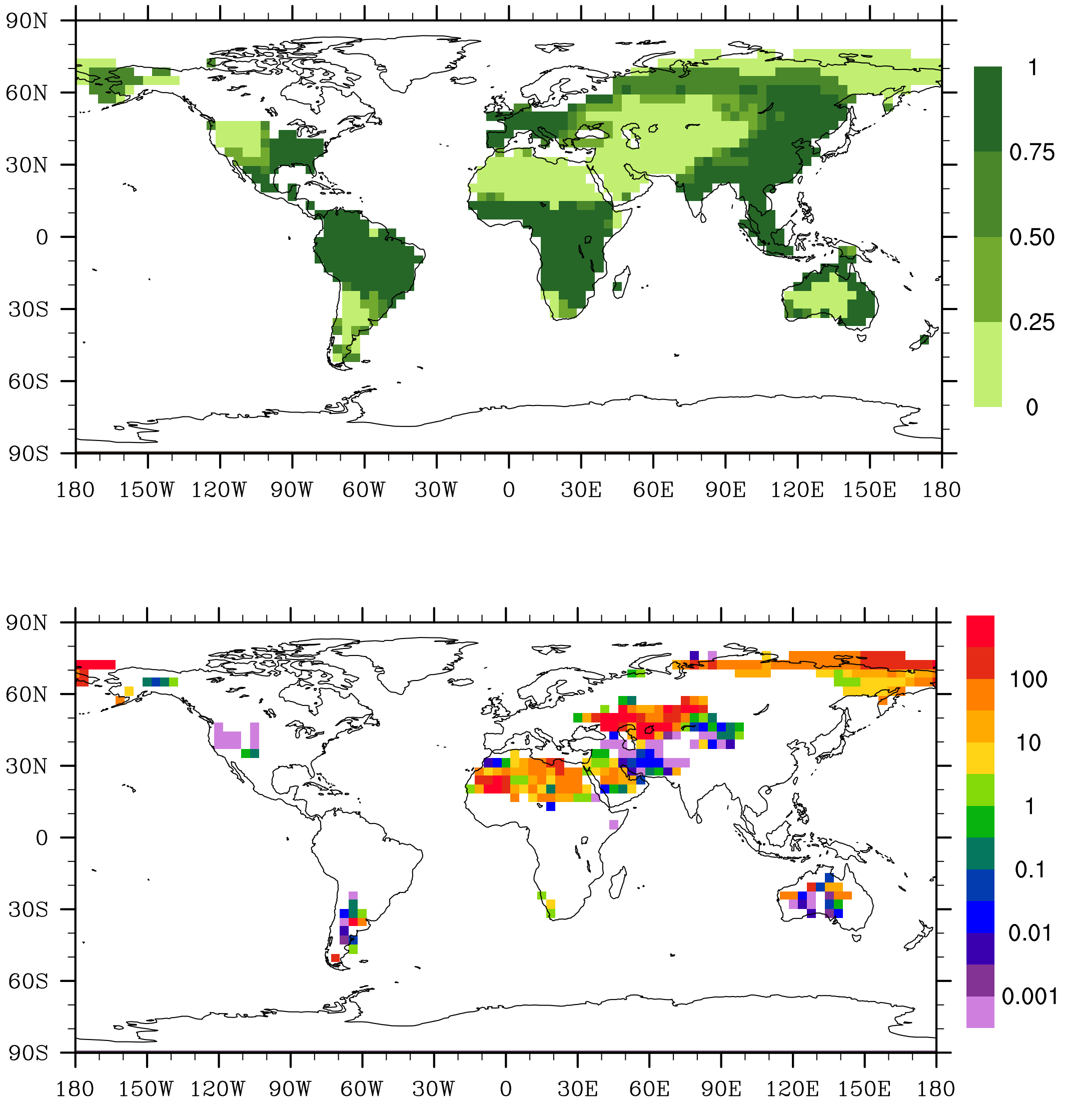

Figure 4.27— Annual maximum vegetation cover fraction obtained from the LPJ model for LGM conditions (top) and the mean dust emission flux $[g/m^2/yr]$ (bottom) for the LGM simulation.

Dust emissions as a function of wind speed and soil moisture

Dust emissions distribution as a function of wind speed in the LGM for the Australian and south African sources does not show a significant difference to their counterparts from the CTRL simulation. Strongest emissions in Australia take place at wind speeds of about 9-12 m/s and in southern Africa at wind speeds of 7-9 m/s (Fig.3.2).

The distribution of South American emissions in the LGM differs from the CTRL simulation (Fig.4.28, left column). In can be seen, that in the LGM the second peak of emissions is not as pronounced as the first peak. The emissions at wind speeds of 10-14 m/s are enhanced by roughly two orders of magnitude. They are associated with regions of relatively high wind speed and relatively low soil wetness. These are regions in the southmost part of the continent and a few grid boxes in Pampas region $35°S, 65-60°W$.

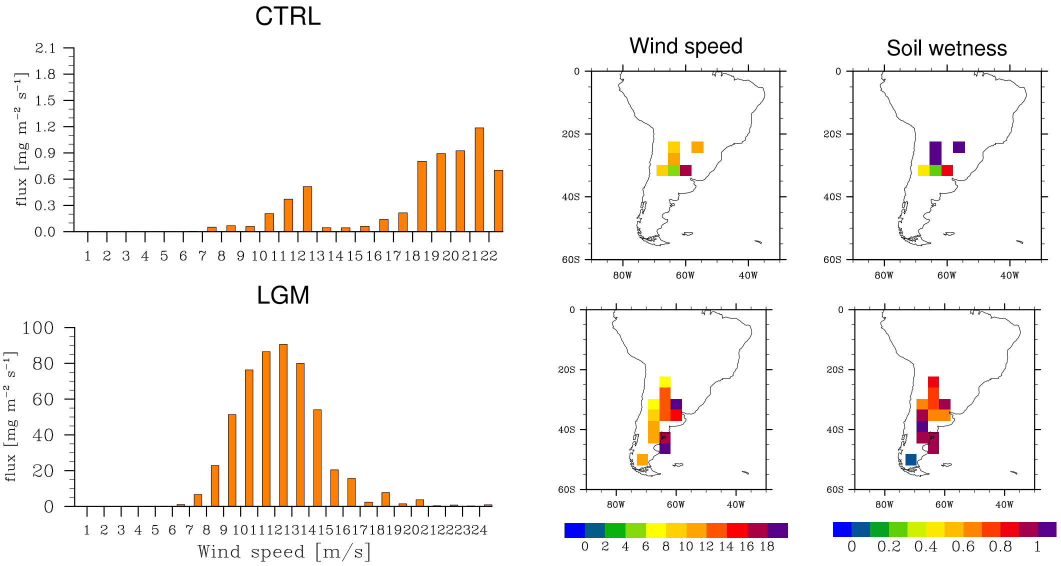

Figure 4.28— Distribution of the dust emission mass flux as a function of wind speed over the South American dust source for CTRL and LGM (left column). The computation is based on 6 hour data for wind bins defined as 0-1, 1-2, 2-3, ... [m/s] for 20 years of each simulation. Typical wind speed [m/s] (middle column) and soil wetness [m] (right column) during dust emissions from the South American dust source.

Seasonal variability of Southern Hemisphere dust emissions

The seasonal cycle of dust emissions from each of the Southern Hemisphere dust sources for the LGM is shown in Fig.4.29 (top). In the LGM simulation the South American dust emissions are strong throughout entire year, which is different compated to interglacial time-slices (Fig.4.14). The reason for this is the year-round high probability of high wind speed over the extended South American dust sources (Fig.4.29, bottom). The relatively low emissions in South America in JJA, despite high wind speed, result from snow cover, which accumulates in the austral winter in the Patagonian region, as well as the slightly increased soil wetness in this region. The seasonal variations in Australian emissions are consistent with the probability of high wind speeds and are maximal in SON, followed by DJF. Seasonality of dust emissions from the south African source is similar in the LGM and CTRL simulations.

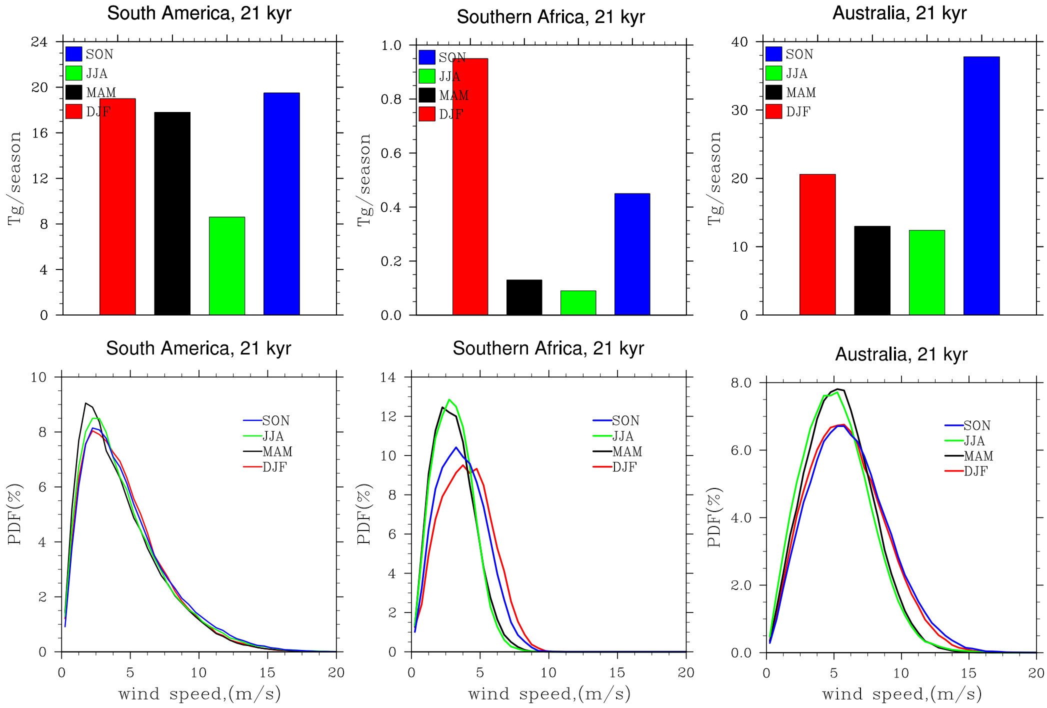

Figure 4.29— Seasonal cycle of dust emissions for the South American, south African and Australian dust sources (top) for the LGM simulation. Note that scales are different. Seasonal cycle of probability density function of wind speed over corresponding dust sources (bottom).

4.2.5 Dust deposition

Simulated global mean LGM to pre-industrial deposition ratio is about 2 (Table 4.10), which is quite similar to previous modeling studies (Albani et al., 2011), and reflects the increase of dust emissions. In the LGM simulation, sedimentation and wet deposition are the main global loss processes for mineral dust. Sedimentation contributes about 44% to total deposition in the LGM, which is similar to the pre-industrial simulation. Wet deposition is slightly reduced in strength in the LGM (41%) compared to CTRL (42%) due to the drier climate conditions. Dry deposition is also a significant sink process, accounting for 15% of dust removal.

Table 4.12— Dust deposition in Antarctica for the CTRL and LGM simulations

Dust deposition, $[Tg/yr]$	CTRL	LGM
Antarctica		
Total deposition	0.053 (100%)	0.540 (100%)
Wet deposition	0.0477 (90.0%)	0.4790 (88.7%)
Dry deposition	0.0005 (0.9%)	0.0039 (0.7%)
Sedimentation	0.0048 (9.1%)	0.0566 (10.6%)

Wet deposition is the dominant loss process over the Antarctic continent, although the relative contribution to the total sink is slightly weakened (Table 4.12). Simulated total dust deposition over Antarctica in the LGM is increased by a factor of 10.2, while emission from the Southern Hemisphere is increased by just a factor of 2.6 (Table 4.10), compared to the pre-industrial time-slice. Albani et al. (2011) suggested that southward extended South American dust source in the LGM, possibly in combination with changes in transport is important for large increase in dust deposition over Antarctica. According to our simulations, slight increase of emissions from Australia may also play role in increased dust deposition over some parts of Antarctica. However, observations (e.g. Delmonte et al., 2010) exclude Australia as a dominant dust supplier during glacial time and corroborate the hypothesis of a uniform South American origin of dust over the entire East Antarctic plateau during the LGM. The annual average deposition of mineral dust in the Southern Hemisphere for the LGM is shown in Fig.4.30. From this figure the strong contribution of South American and particularly Patagonian dust to the deposition in Antarctica can be seen.

According to Mahowald et al. (1999), the processes that could explain high dust deposition in the glacial climate are extended dust source areas due to changes in soil moisture and/or reduced vegetation cover leading to larger dust mobilization; a more vigorous atmospheric circulation, leading to more efficient entrainment and transport of dust; a weakened hydrological cycle, leading to less efficient scavenging by precipitation and therefore more efficient transport of dust. In terms of increased dust deposition over Antarctica, Albani et al. (2011) has added to this the enhanced

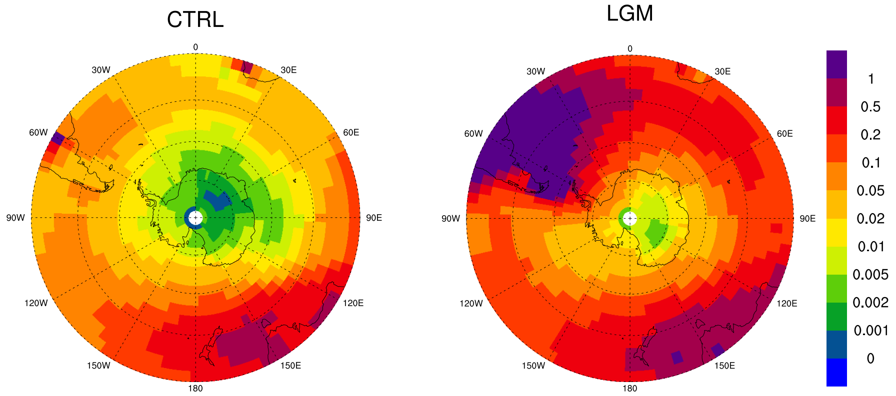

Figure 4.30— Annual average dust deposition $[\mu g/m^2]$ in the Southern Hemisphere for the CTRL and LGM simulations.

transport efficiency from Southern Patagonia, less vertical mixing and more efficient scavenging over Antarctica, due to lower transport. In the next subsection (4.2.6) the influence of atmospheric transport and precipitation on dust deposition over Antarctica during the LGM is analyzed.

4.2.6 Processes influencing dust deposition in Antarctica

To calculate air mass trajectories leading from the Southern Hemisphere dust sources to the Antarctic continent for the LGM the method described in section 3.2.5 was used and results are shown in Table 4.13.

The seasonality of the atmospheric transport in the LGM is similar to the CTRL simulation with maximum number of trajectories in JJA and minimum in DJF. Similar to CTRL a more pronounced seasonal cycle of atmospheric transport is found in the lower troposphere than in the middle troposphere. These results are in agreement with a previous study by Krinner et al. (2010), suggesting that seasonality of the modeled near-surface and upper level tracer concentration above Antarctica is fairly similar for the present and the LGM, with maximum concentration in winter and minimum in summer. However in contrast to CTRL and other interglacial time intervals the seasonality in the LGM is less pronounced. The low-level transport in DJF is increased by a larger factor than the transport in JJA in the LGM compared to CTRL. The increased meridional temperature gradient in the LGM leads to more efficient poleward transport (Petit et al., 1999). The Antarctic ice sheet serves as an effective barrier to the southward-moving air in the lowest level of the atmosphere (Parish and Bromwich, 2006). The influence of this barrier is weaker in austral summer (DJF) leading to higher relative increase of trajectories reaching the Antarctic continent in DJF compared to the increase of trajectories in JJA.

The total low-level transport in the LGM is more active compared to CTRL. This is consistent with Krinner and Genthon (2003) who indicated a more frequent fast low-level tracer advection towards Antarctica as a consequence of the more vigorous meridional eddy transport and of the increased vertical atmospheric stability (less convection) during the LGM. On the other hand in our study the middle troposphere transport in the LGM is stronger than in the CTRL run as well. However, the study by Krinner and Genthon (2003) suggest a lower fraction of tracers advected via the upper-level pathways in the LGM than in present. The reason for this disagreement could be related to different trajectory analyses. Krinner and Genthon (2003) consider the tracers originating above 400 hPa over the Southern Ocean between 50 and 70° S in contrast with our trajectories that originate only above the Southern Hemisphere dust sources at the height of 500 hPa.

In the LGM, the fraction of the trajectories originating at 800 hPa over Australian and South American sources and reaching Antarctica is similar, while trajectories originating at the height of 500 hPa are mostly dominated by the South American source. In other words our simulation shows increased transport from South America to Antarctica in the LGM, similar to the study of Krinner and Genthon (2003).

Table 4.13— Total number of trajectories originating at the height of 500 hPa and 800 hPa over the Southern Hemisphere dust sources and reaching Antarctica within 10 days for the CTRL and LGM simulations.

	CTRL 800hPa	21ky 800hPa	CTRL 500hPa	21ky 500hPa
Number of trajectories originating over SH sources and reaching Antarctica				
DJF	979 (5.7%)	4728 (12.2%)	702 (10.3%)	3011 (13.8%)
MAM	4391 (25.6%)	10018 (25.8%)	2307 (33.9%)	6123 (28.0%)
JJA	8234 (48.0%)	14969 (38.6%)	2496 (36.7%)	7440 (34.0%)
SON	3565 (20.8%)	9041 (23.3%)	1301 (19.1%)	5314 (24.3%)
Σ	17169 (8.7%)*	38756 (12.9%)*	6806 (3.5%)*	21888 (7.3%)*
Total number of trajectories originating over SH sources	197100	299300	197100	299300
Average number of trajectories originating over a single grid box and reaching Antarctica				
DJF	36.3	115.3	26.0	73.4
MAM	162.6	244.3	85.4	149.3
JJA	305.0	365.1	92.4	181.5
SON	132.0	220.5	48.2	129.6
Σ	636.0	945.2	252.1	533.8

* - Percentage is calculated relative to the total number of potential trajectories originating over the Southern Hemisphere dust sources.

The quantitative contribution of dust emissions, precipitation and transport to dust deposition in Antarctica for the CTRL and LGM simulations is shown in Fig.4.31.

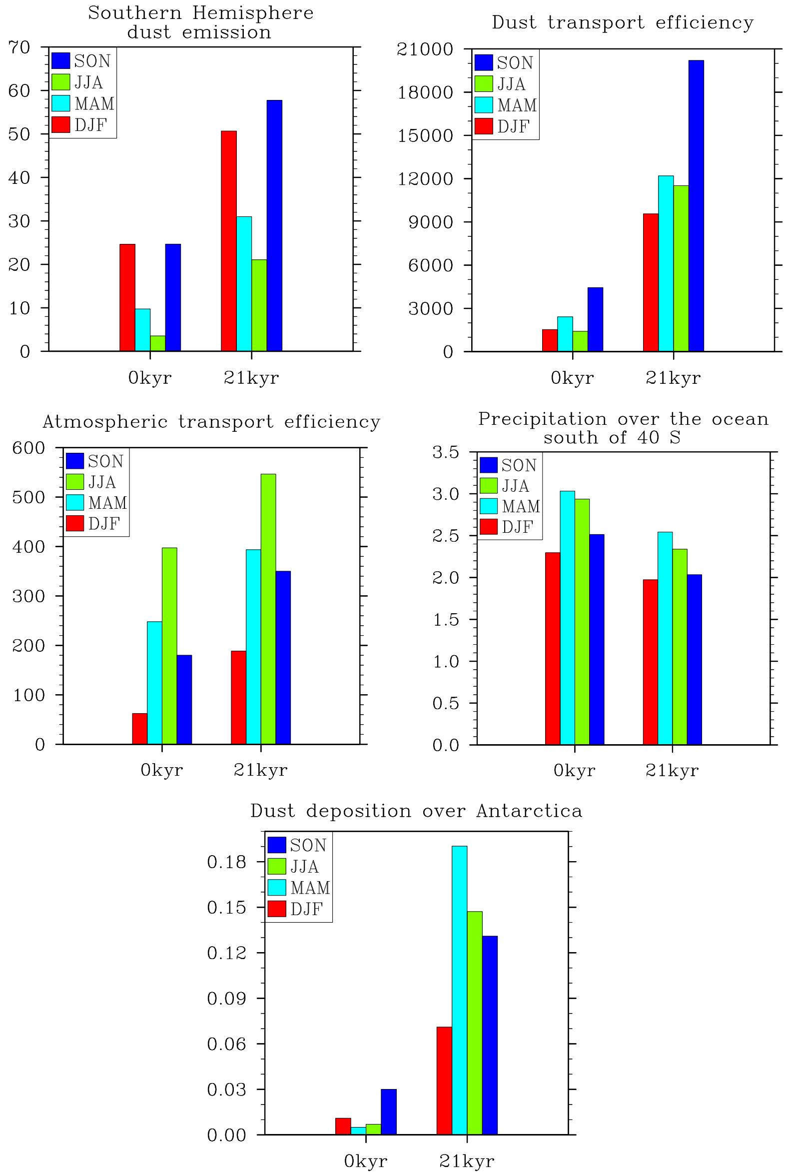

Figure 4.31— Impact of Southern Hemisphere dust emission $[Tg/season]$ (top left), atmospheric transport efficiency $[trajectories\,per\,season]$ (central left), the dust transport efficiency $[arbitrary\,units]$ (top right), precipitation over the ocean south of $40°$S $[mm/day]$ (central right) on dust deposition in Antarctica $[Tg/season]$ (bottom) for the CTRL and LGM simulations. Atmospheric transport efficiency is a sum of number of trajectories per season originated at 500 hPa and 800 hPa from a single dust source grid box and reached Antarctica within 10 days.

In the LGM, enhanced Southern Hemisphere dust emissions, together with increased transport and reduced precipitation over the Southern Ocean lead to an increase of dust deposition over Antarctica by a factor of about 10.2 compared to the CTRL simulation.

The seasonality of dust deposition over Antarctica in MAM and JJA is not strongly affected by precipitation. This probably results from an increased fraction of snow fall, compared to rain in the LGM over the Southern Ocean and different scavenging efficiency coefficients for snow and liquid in the model (Stier et al., 2005). According to Stier et al. (2005), liquid precipitation removes aerosol more efficiently than snow. The geographical patterns of seasonal maximum dust concentration in Antarctic ice in the LGM depend on the region and are shown in Fig.4.32. However, for interglacial time-slices the maximum dust concentration is in SON for entire Antarctica.

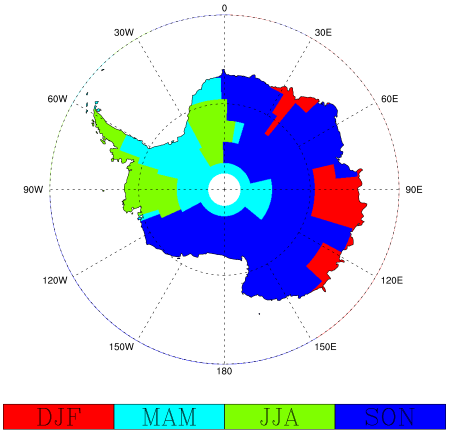

Figure 4.32— The seasons with maximum dust concentration in the Antarctic ice for the LGM simulation.

4.2.7 Atmospheric transport towards Antarctica

In this section a more detailed analysis of atmospheric transport is presented. In particular the roles of polar transport by the mean circulation and transport by synoptic eddies are investigated.

In the LGM, due to a colder climate and weaker wet removal, as well as less vertical mixing, the most effective dust transport to Antarctica is located at lower, compared to interglacials, pressure level, which is of about 600-700 hPa. In figure 4.33, the mean meridional dust flux is shown. The near-surface equatorward flux over high southern latitudes in the LGM is confined closer to the surface and the poleward transport (blue color) of meridional dust flux towards Antarctica is stronger than in CTRL. The contribution of the synoptic scale eddies to the the total dust transport is shown in Fig.4.34. In the LGM the eddy fluxes in high southern latitudes are negative, which means that they contribute to the poleward transport of dust in all seasons, with contrast to CTRL where some near-surface values over Antarctica in DJF and MAM show positive (equatorward) values (Fig.3.11). This is due to colder climate conditions, increase of the pole-equator temperature gradient and the establishment of a more stable equatorward flow in Antarctica, which contributes to a stronger and more persistent katabatic winds.

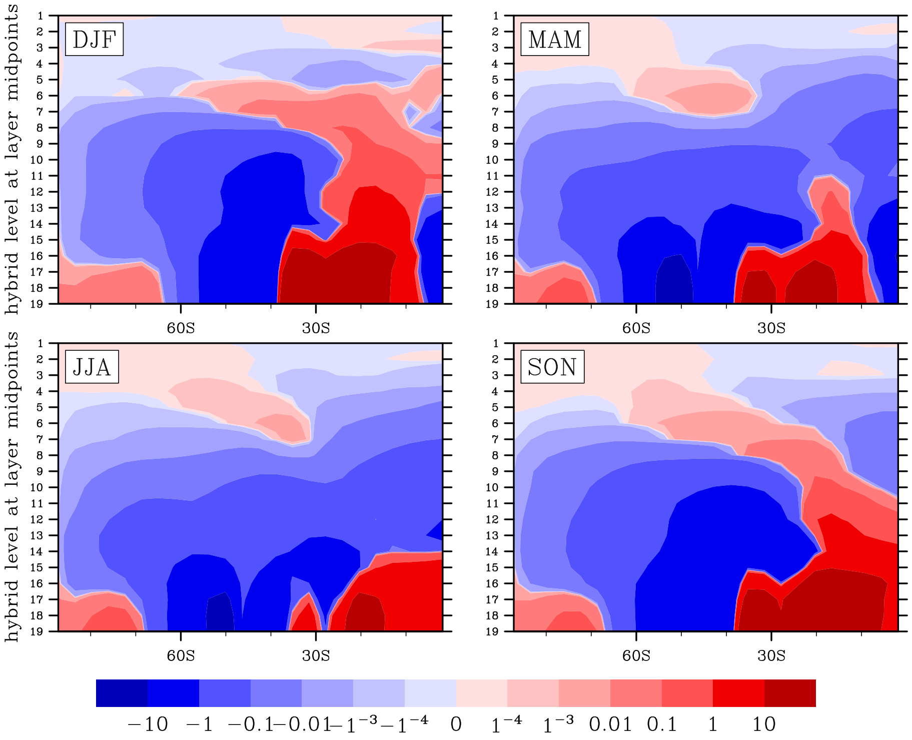

Figure 4.33— Seasonal mean zonal average meridional dust flux $[\mu g/m^2/s]$ over the Southern Hemisphere for the LGM simulation.

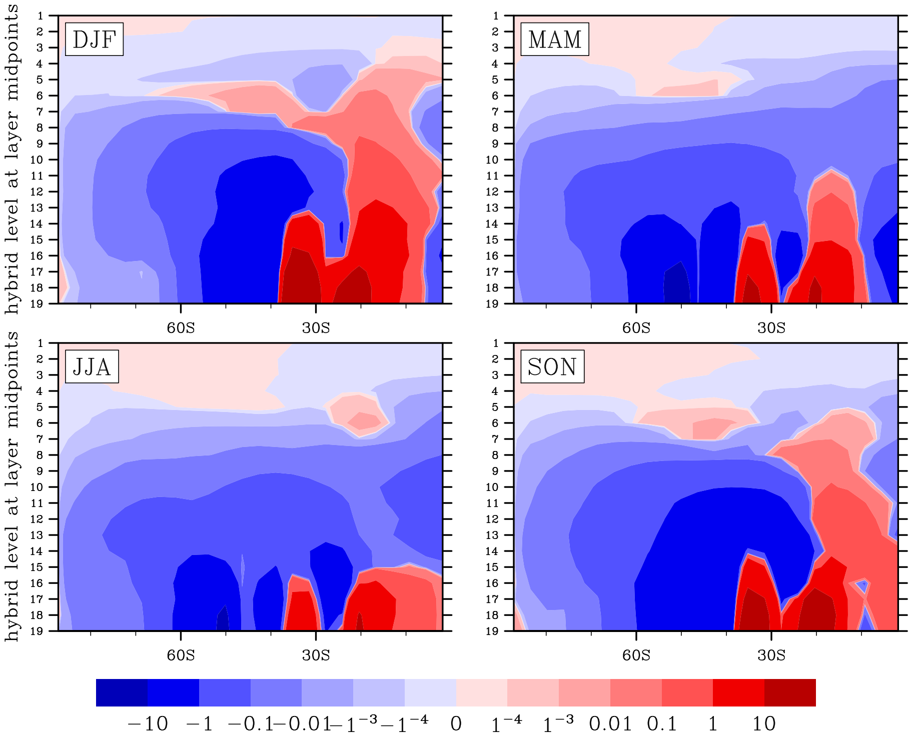

Figure 4.34— Seasonal mean zonal average synoptic scale eddy flux ($\overline{V \cdot DU} - \overline{V} \cdot \overline{DU}$) over the Southern Hemisphere for the LGM simulation.

Chapter 5

Validation of the dust deposition

5.1 Description of observational data

The modelled dust deposition flux of the pre-industrial simulation is compared with observed records of dust deposition. Records of dust deposition included in the current study are ice core measurements, marine sediment core and marine sediment trap records. The data are derived from the second version of the ”Dust Indicators and Records of Terrestrial and Marine Palaeoenvironments” data base (DIRTMAP, Kohfeld and Harrison, 2001).

The continental particulate material deposited on ice sheets is of purely aeolian origin. Of all the dust archives, ice cores are therefore the most straightforward to interpret and can provide useful records of dust deposition from regions that are currently ice-covered (Kohfeld and Harrison, 2001). Deposition fluxes derived from ice core data are given in Table 5.1. The data include information on dust concentrations (both particle number and mass), ice accumulation rates, and dust deposition fluxes. This information is available for the current time-interval and as LGM/current ratio.

According to Mahowald et al. (1999), dust concentrations in the ice are measured by several different techniques and, as a result, are expressed in several different ways (e.g. total insoluble mass as measured by laser light scattering, Al concentration measured by atomic absorption, and Coulter Counter measurements of particle number concentrations). It was assumed that all the methods yield broadly comparable results, although there are differences in calculated ratios depending on whether mass- or number-based concentrations are used. In this data base, ice core dust deposition is expressed as deposition fluxes and not dust concentration in the ice core. This ensures consistency with the marine sediment data. The disadvantage of converting ice core data from concentration to fluxes is that this calculation relies upon estimated ice accumulation rates (Mahowald et al., 1999).

The time intervals vary between the different locations. The current value is the mean for the Holocene (0-10 kyr) or the mean of samples from a shorter period within that interval. The LGM value is either the mean of the interval 15-30 kyr or the mean of samples from a shorter period within that interval.

Table 5.1— Dust deposition fluxes retrieved from ice cores

Site	Dust concentration				Ice Accumulation Rate $mw.eq.yr^{-}1$			Dust Deposition $gm^{-}2yr^{-}1$	
	Current $ngg^{-}1$	LGM/ Current	Reference	Method	Current	LGM/ Current	Reference	Current	LGM/ Current
Greenland:									
Camp Century (77N, 61W)	125	11	Cragin et al., 1977	mass	0.35	0.2	Johnsen and Dansgaard, 1992	0.04	2.2
		12	Thompson and Mosley-Thompson, 1981	number					2.4
Dye 3 (65N, 44W)	50	5-60	Hammer et al., 1985	$mass^*$	0.45	0.28	Johnsen and Dansgaard, 1992	0.02	1.5-17
Renland (71N, 27W)	133	8	Hansson, 1994	$mass^*$	0.46	0.22	Johnsen and Dansgaard, 1992	0.06	2
GRIP, Summit (73N, 38W)	38	$(158)^{\star}$	Steffensen, 1997	$mass^*$	0.21	0.43	Dahl-Jensen et al., 1993	0.008	$(68)^{\star}$
GISP2, Summit (73N, 38W)					0.22	0.25	Cuffey and Clow, 1997		
Antarctica:									
Byrd (80S, 120W)	19	7	Cragin et al., 1977	mass	0.16	0.5	Lorius, 1989	0.003	4
		3	Thompson and Mosley-Thompson, 1981	number					1.5
Dome C (75S, 124E)		6	Thompson and Mosley-Thompson, 1981	number	0.034	0.5	Lorius, 1989		3
		12	Petit et al., 1981	number					6
		23	Petit et al., 1981	$mass^*$					12
	34	21	Petit et al., 1981	mass				0.001	11
	26	17	Royer et al., 1983	$mass^*$				0.0009	8.5
Vostok (78S, 107E)	30	37	De Angelis et al. 1984	mass	0.023	0.5	Lorius, 1989	0.0007	18.5
			Petit et al., 1990	mass					15.0
Other									
Devon, Canada (67N, 66W)		20-30	Fisher, 1979	number	0.22	0.33	Paterson and Hammer, 1987		7-10
Dunde, China (38N, 97W)		1.5-4	Thompson et al., 1989	number	0.4	> 1	Thompson et al., 1989		$> 1.5 - 4$
Guliya, China (35N, 82W)		< 1	Thompson et al., 1997	number	0.2	0.2	Thompson et al., 1997		< 0.2
Huascarn, Peru (9S, 78W)	160	200	Thompson et al., 1995	number	1.3	< 1	Thompson et al., 1995	0.2	< 200
Sajama, Bolivia (18S, 69W)		0.125	Thompson, Mahowald's communication, 1998	number		1.5-1.75	Hastenrath and Kutzbach, 1985		0.20 0.20

Current climate dust deposition rates to the ocean using marine sediment trap data archived in the DIRTMAP database are given in App.F.2. Terrigenous accumulation rates were calculated by isolating terrigenous material from organic carbon, carbonate content, and biogenic opal (e.g. Wefer and Fischer, 1993). In the north Pacific sites, the terrigenous content was estimated from Al concentration measurements (Satio et al., 1992), assuming that terrigenous material is 8% Al. According to Mahowald et al. (1999), the data measurements cover seasonal to annual fluxes, since the sediment traps were deployed for 176-1626 days, with the exception of two Pacific Ocean studies (Noriki and Tsunogai, 1986; Satio et al., 1992) that sampled mostly 14-30 day periods. In the current study only those stations with deployment period larger than 50 days was used following suggestion by Tegen et al. (2002).

Additionaly, estimates of dust deposition to the ocean based on marine core records from the DIRTMAP database were used. Marine sediment data are available for current climate and as LGM/current dust deposition ratio (App.F.4). According to Mahowald et al. (1999), aeolian accumulation rates $MAR_{eol}(g/m^2/yr)$ in marine sediments are generally calculated as

$MAR_{eol} = LSR(BD)f;$

where $LSR(m/yr)$ is the linear sedimentation rate, $BD(g/m^3)$ is the sediment bulk density (standard error = ± 10-25%), and f is the measured aeolian fraction of the sediment sample (standard error = ± 10-40%). The aeolian fraction is determined by eliminating carbonate and opaline components from total particles, methods summarized by Rea (1994). In cores from the Pacific and Indian Oceans, oxides and hydroxides are also eliminated (e.g. Clemens and Prell, 1990; Hovan et al., 1991). Sediment age models were determined using radiocarbon dates where available (Ruddiman, 1997; Sirocko et al., 1991) and the SPECMAP oxygen isotope timescale (e.g. Imbrie et al., 1984) everywhere else. The samples represent average values over periods of several thousand years. The surface sediment samples generally represent the average for the Holocene, but the precise periods vary from data set to data set (e.g., 3-11 kyr in the Atlantic Ocean (Ruddiman, 1997) and 0-8 kyr in the Indian Ocean (Sirocko et al., 1991)). For the LGM, the values are averages for the interval 18 ± 2 kyr B.P., except for sites derived from the Ruddiman (1997) and Sirocko et al. (1991) studies, which both give averages over the interval 15 to 25 kyr (Mahowald et al., 1999).

5.2 Validation for pre-industrial time-slice

Simulated dust deposition flux in the pre-industrial CTRL time-slice and dust deposition data compiled from ice cores, marine sediment traps and marine sediment cores (circles) are shown in Fig.5.1 (top).

The simulated patterns of dust deposition capture the observed high dust deposition rates in the Atlantic ocean close to the western coast of the Saharan desert, in the Arabian Sea, as well as in the western parts of north Pacific ocean close to the Asian source region.

A scatter plot of observed deposition fluxes and model values at the closest grid point, highlighting data from Antarctica (indicated by red color) and Greenland (indicated by green color) is shown in Fig.5.1 (bottom). The correlation coefficient of the observed versus modeled values for marine sediment traps data is 0.87, for ice core data it is 0.77, while for marine sediment it is only 0.31. The low correlation of the modeled data with marine sediment data is caused either by model's underestimation of the values in the Arabian Sea or uncertainty in the observations. The model's underestimation of dust deposition in the Arabian Sea is most likely due to underestimation of the source on the Arabian peninsula. The correlation coefficient of the natural logarithm of the all observed and modeled values is 0.78. The root mean square error of the difference between the natural logarithm of the observations and the model is 1.64. The model tends to underestimate the magnitude of dust deposition off the east coast of Asia, but the geographical location of the plume appears to be consistent with the data available from this region. Most of the sites are located in the Northern Hemisphere and fewer datasets are available for the Southern Hemisphere. Therefore it is difficult to validate the model for southern latitudes. However, marine sediment data from south-east of Australia suggest that the model does capture the general pattern and magnitude of deposition observed in the Tasman sea. Notable discrepancy between the simulated and available observed dust deposition in the pre-industrial period occurs in the northern high-latitudes in Greenland, where the model overestimates the observed deposition by a factor of about 3-10. A similar disagreement is also reported in Mahowald et al. (1999). In the southern high-latitudes in Antarctica the model overestimates observed values by a factor of about 2-3. At the same time, the model underestimates the dust deposition in the Weddel Sea close to Antarctica, which also occurs in other global modeling studies (e.g. Huneeus et al., 2011).

Dust deposition flux in the pre-industrial PreVeg simulation and dust deposition data, as well as scatter plot of observed deposition fluxes versus model values are shown in Fig.5.2. In Greenland the PreVeg simulation shows better agreement with ice-core records than CTRL, but are still overestimated the observed values. Compared to CTRL, this simulation better repoduces the observations both in the North Pacific ocean as well as close to Sahara. However in Antarctica the modeled data from PreVeg strongly overestimate the dust deposition, due to the overestimation of Australian source.

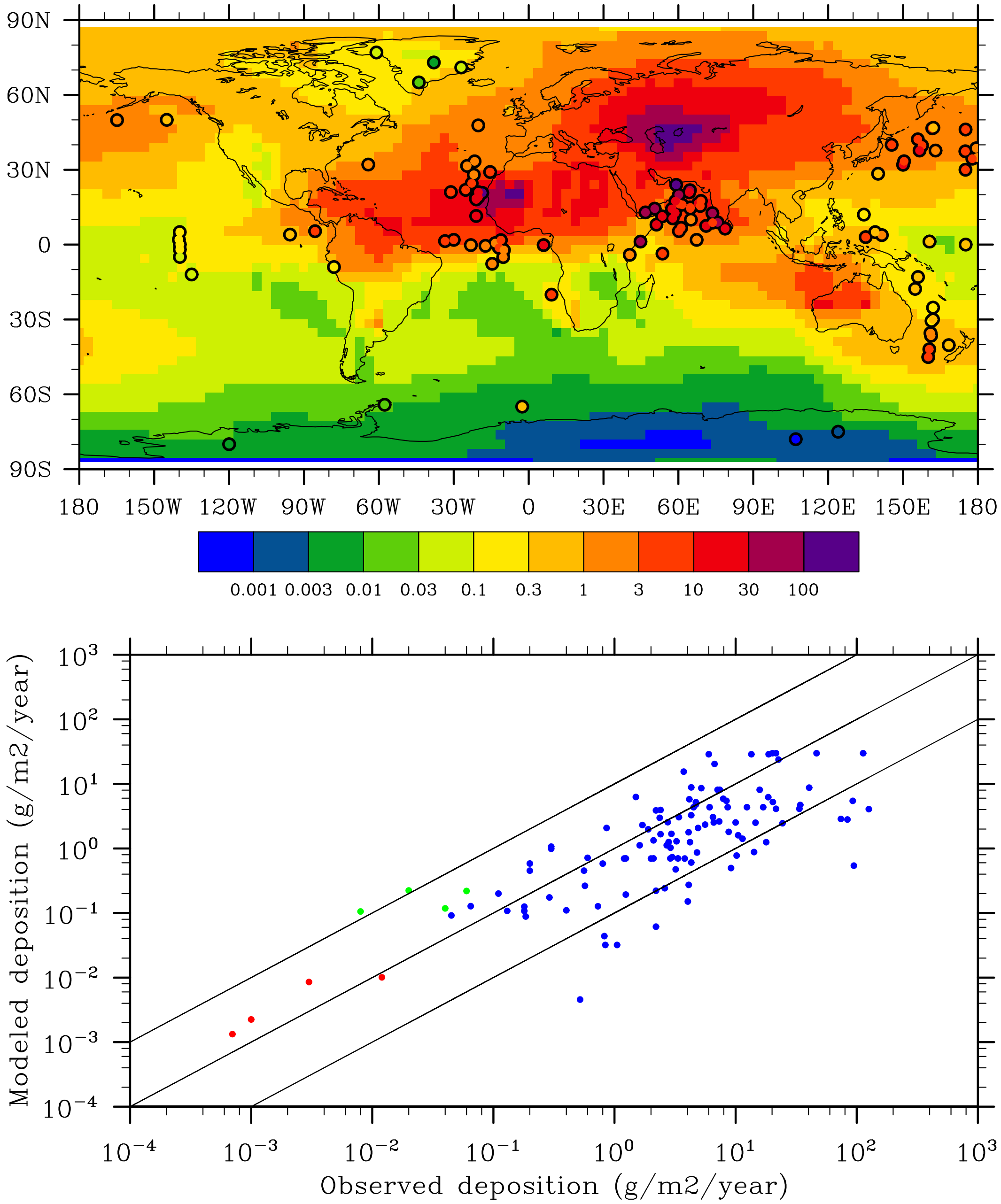

Figure 5.1— Simulated dust deposition flux ($g/m^2/yr$) for the pre-inductrial CTRL simulation compared with dust deposition data compiled from ice cores, marine sediment traps and marine sediment cores ($g/m^2/yr$) (circles) and a scatter plot between the modeled and observed dust deposition. Red color indicates data in Antarctica, green indicates data in Greenland, blue is elsewhere.

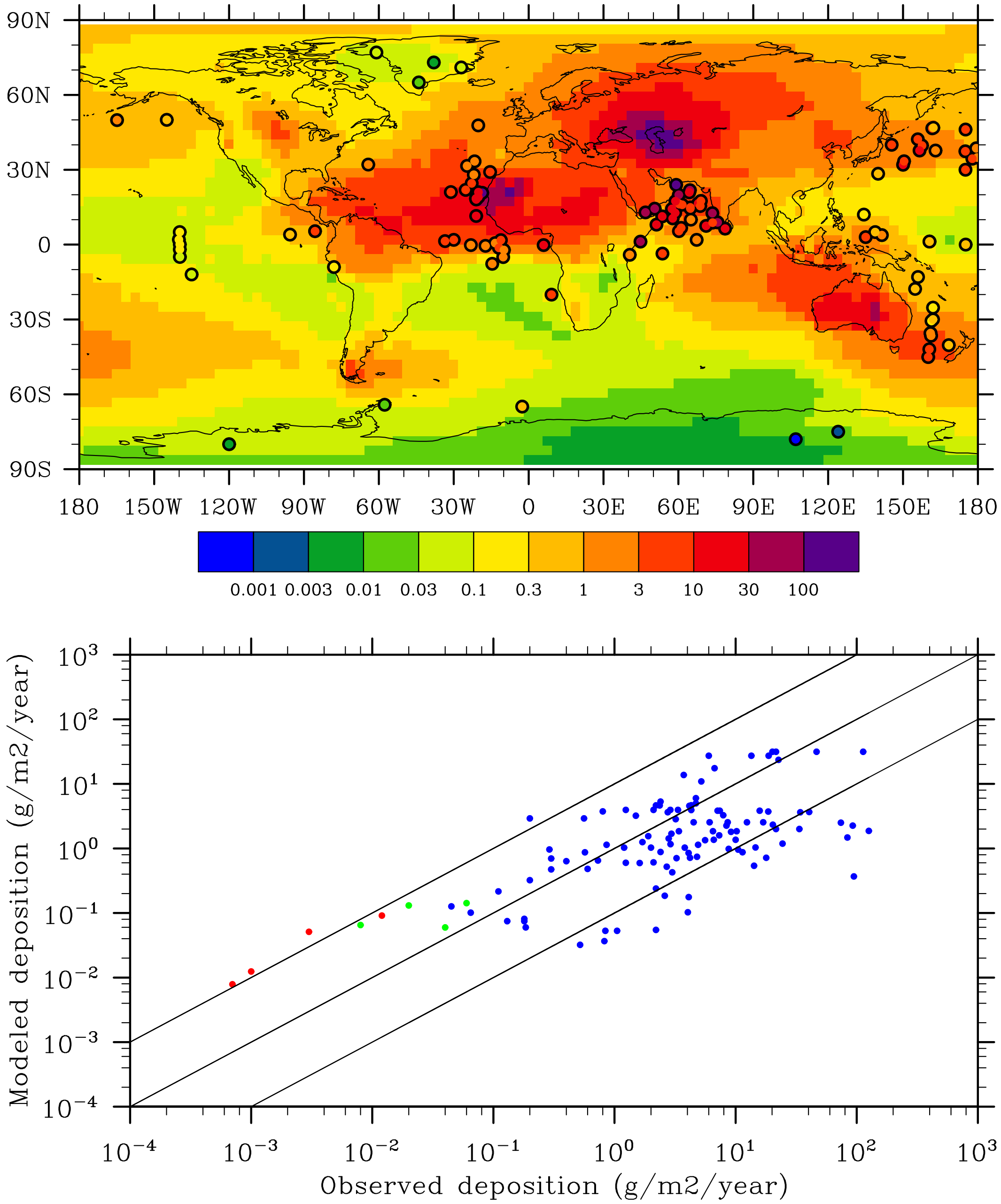

Figure 5.2— Simulated dust deposition flux $(g/m^2/yr)$ for the pre-inductrial PreVeg simulation compared with dust deposition data compiled from ice cores, marine sediment traps and marine sediment cores $(g/m^2/yr)$ (circles) and a scatter plot between the modeled and observed dust deposition. Red color indicates data in Antarctica, green indicates data in Greenland, blue is elsewhere.

5.3 Validation for the LGM simulation

The absolute magnitude of the observed LGM dust deposition rates (circles) and modeled data are shown in Fig.5.3 (top). Dust deposition records at the LGM show deposition flux that are generally higher than in the current climate. Observations indicate that in the LGM, dust deposition in the tropics and mid-latitudes was 2-5 times higher than today, while dust deposition at high latitudes in polar regions was up to 20 times higher than today (Kohfeld and Harrison, 2001). A scatter plot of the observed versus modeled dust fluxes (Fig.5.3, bottom) for the LGM shows that the model is able to capture the high- and low-deposition regions. The correlation coefficient of the natural logarithm of the observed and modeled values is 0.81. The root mean square error of the difference between the natural logarithm of the observations and the model is 1.67. The model underestimates deposition in the tropical Atlantic. In Greenland, the model is in better agreement with the LGM observations than in the current climate, while in eastern Antarctica the model underestimates LGM deposition by factor of about 4-5. The observational studies (e.g. Delmonte et al., 2010) suggest uniform South American origin of LGM dust in the East Antarctic plateau. This would suggest that the model underestimates the LGM dust source in South America.

The LGM/current dust deposition ratio is shown in Fig.5.4. Close to the current source regions two- to five-fold increases can be seen downwind of the west of Sahara Desert and in the Arabian Sea downwind of the Arabian Peninsula. The model underpredicts the increase in dust deposition observed in sediment samples near west African equatorial region. In the east Antarctica, the deposition rate is up to 20 times higher in Dome C and Vostok ice cores in the LGM compared to current climate, which is underestimated by the model. In the west Antarctic site the model is in good agreement with the observations. The underestimation of high increase of observed aeolian deposition in Greenland is likely due to the weak North American dust source in the model. Mahowald et al. (1999) suggests that only 50% of the dust deposited in Greenland is from Asia. This imples that sources in northern Siberia, Alaska, and the Canadian Arctic might have been important as well.

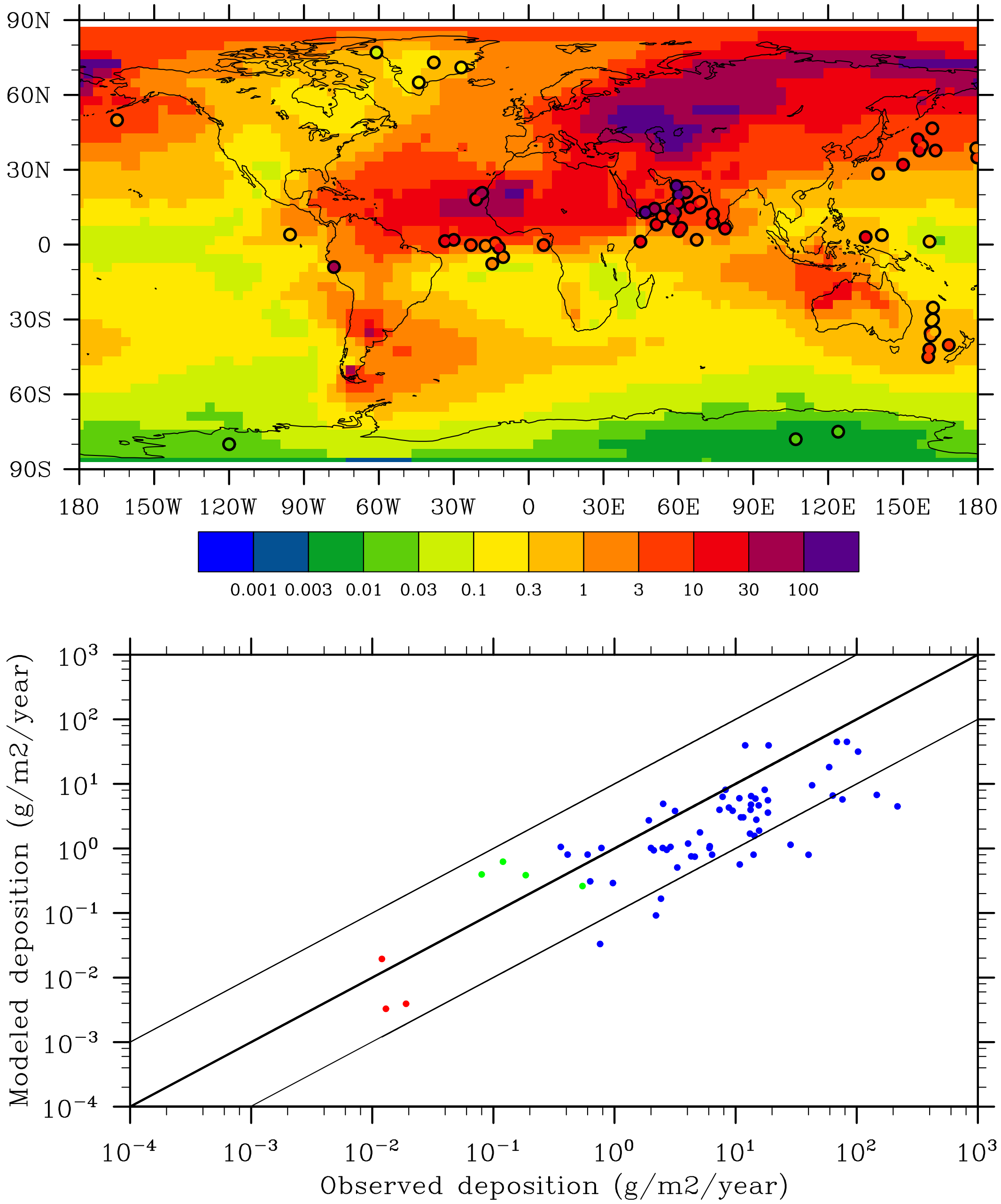

Figure 5.3— Simulated dust deposition flux ($g/m^2/yr$) for the LGM simulation compared with dust deposition data compiled from ice cores, marine sediment traps and marine sediment cores ($g/m^2/yr$) (circles) and a scatter plot between the modeled and observed dust deposition. Red color indicates data in Antarctica, green indicates data in Greenland, blue is elsewhere.

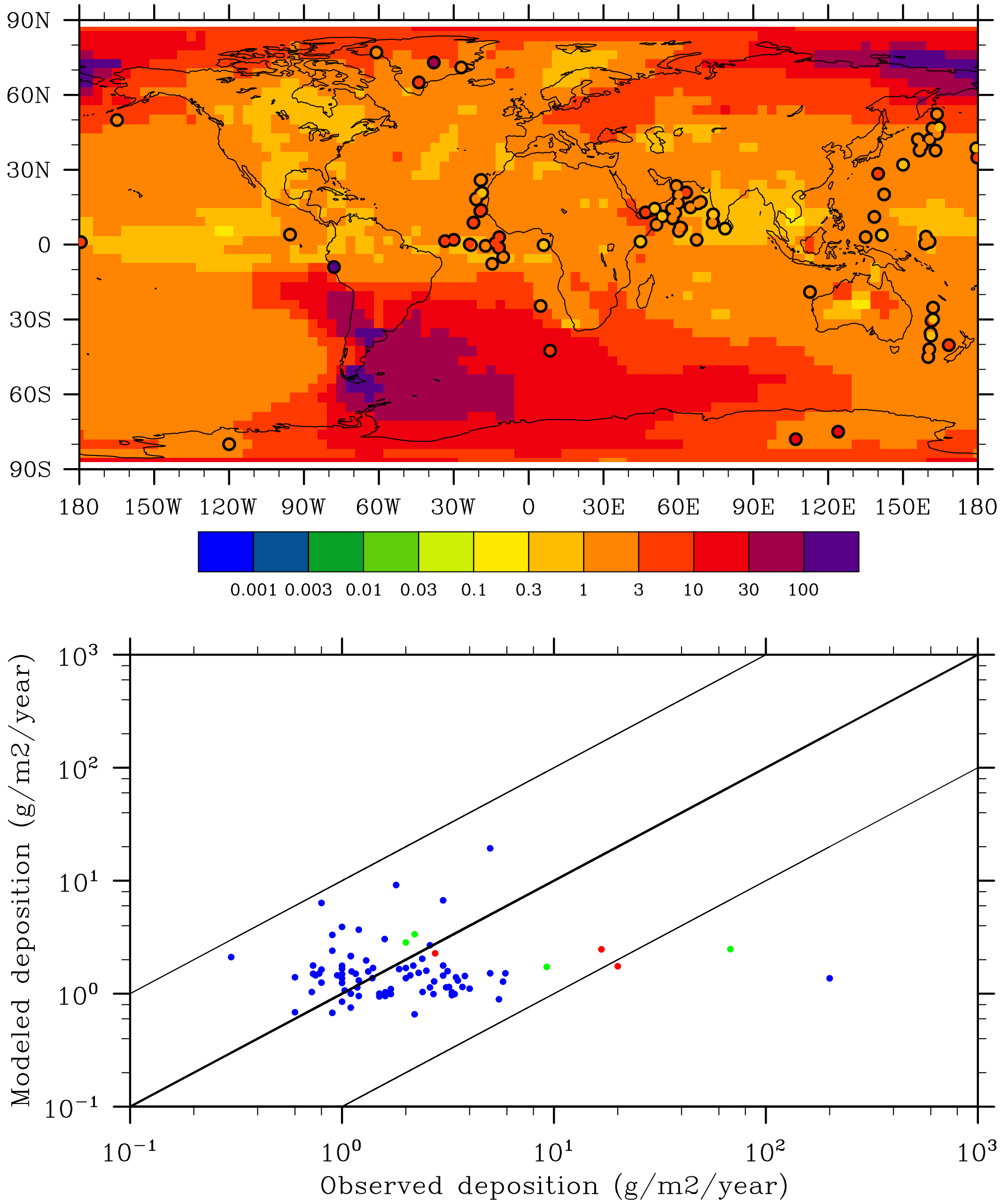

Figure 5.4— Ratio of modeled dust deposition during the LGM to the current climate compared to the ratio of dust deposition during the LGM to the current climate from ice cores and marine sediment cores and a scatter plot between the modeled and observed dust deposition. Red color indicates data in Antarctica, green indicates data in Greenland, blue is elsewhere.

5.4 Validation for the interglacial time-slices

The comparison of the model results against observations is a nontrivial task for 6 kyr because many of the available records represent the average for the Holocene (0-10 kyr) and assumed to show the current climate data. The deeper into the time the less data are available. However some measurements from ice cores and marine cores can be found in the literature for the interglacial time-slices 6 kyr, 115 kyr and 126 kyr.

The scatter plot between few marine core records in Tasman Sea (Kawahata H., 2002) and modeled dust deposition shows that the model tends to overestimate the records in 126 kyr (Fig.5.5), though it is difficult to judge due to lack of observations.

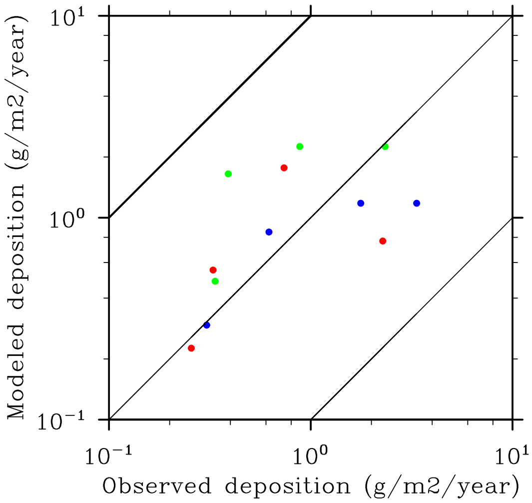

Figure 5.5— Scatter plot between the observed and modeled dust deposition [$g/m^2/yr$] in the Tasman sea for the 6 kyr (blue), 115 kyr (red) and 126 kyr (green).

Ice core records, which are shown in Fig.5.6 (left), represent three Antarctic sites, Vostok ($78°S, 106°E$) (Petit et al., 1999), EDC ($75°S, 123°E$) (Lambert et al., 2008) and EDML ($75°00S, 0°04E$)(personal communication, Anna Wegner, 2012). Location of the sites is shown in Fig.5.6 (right).

The dust mass concentration from the Vostok ice core (shown in blue) was calculated from the total volume concentration by using Coulter counter and covers the past 420 kyr (Petit et al., 1999). Dust records from EDC were obtained by using both a Coulter counter (shown in green) and laser sensor (shown in dark grey) and covers the interval from 0 to 800 kyr B.P. There are slight discrepancies between the data obtained by using this two different methods during MIS 5.5 (126 kyr) and it is possibly related to the different sampling resolution (Lambert et al., 2008). Data from EDML (shown in brown) were calculated using laser sensor.

The records of dust mass concentration from Vostok, EDC and EDML for the

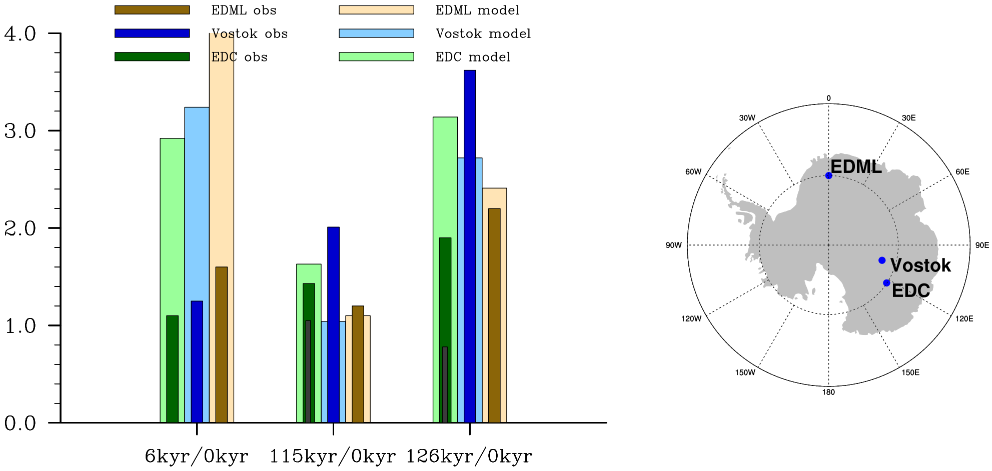

Figure 5.6— The ratio of dust concentration in the ice for the sites Vostok, EDML and EDC from model simulations (dark colors) and observations (light colors) for 6 kyr, 115 kyr and 126 kyr with respect to pre-industrial period (left). Location of the Antarctic sites (right).

intervals 6 ± 1 kyr, 115 ± 1 kyr and 126 ± 1 kyr were extracted and compared to the pre-industrial values (0-4 kyr or shorter period within this interval) from corresponding ice cores.

The ratios of dust mass concentration for interglacial time-slices relative to the pre-industrial in Antarctic ice from model simulation and observations are shown in Fig.5.6.

The plot shows an increase of observed dust concentration in the ice (calculated by using Coulter counter) at all sites for the past interglacial time-slices compared to pre-industrial values. The maximal increase in the records appears in 126 kyr. However the dust mass concentration from EDC, calculated by using laser sensor shows similar values in 115 kyr and a decrease in 126 kyr compared to pre-industrial. Model results are in general agreement with the observations, with exceptions for overestimated 6 kyr to pre-industrial ratio which is likely due to too high emissions from the South American and Australian sources (see details in chapter 6). The underestimation in Vostok in 115 kyr and 126 kyr is most likely a consequence of the underestimation of the South American dust source. A too strong simulated Australian source causes an overestimation of the dust deposition at EDC for the time slices of 6 kyr and 126 kyr.

Chapter 6

Discussion

Vegetation plays an important role in dust modeling because it determines the areas, preferential for dust mobilization. Applying different vegetation maps, obtained from various vegetation models, result in different dust emission fluxes. Furthermore, very few vegetation reconstruction data in the Southern Hemisphere for the interglacial periods are available. Thus, vegetation information is a major source of uncertainty in our dust simulations.

In the current study vegetation cover for different time-slices was obtained from dynamical vegetation model LPJ. To calculate preferential dust sources the approach described in Tegen et al. (2002) with some modification (see details in section 2.2.6, equation 2.8) was used. The preferential dust sources are defined as regions with annual maximum vegetation cover fraction less than or equal to 25%. Such method involves a large difference in dust mobilization from neighboring grid-boxes with vegetation cover of 25% and let's say 25.1%, which is not realistic. This is particularly important for simulations with low spacial resolution. Note that in Tegen et al. (2002) and Werner et al. (2002) the very high spatial model resolution of $0.5 \times 0.5°$ was used. The approach has a slope for dust emissions from areas with vegetation cover less than or equal to 25%. But when vegetation cover is more than 25%, emissions is 0. Thus, the method does not have a slope for vegetation cover more than 25%.

To check the sensitivity of such vegetation cover threshold in the determination of dust source areas the second run for the mid-Holocene is performed and named 6 kyr Pref. The preferential dust source areas for this simulation are defined as regions with annual maximum vegetation cover fraction less than 25%. In 6 kyr Pref the grid box in South America with extremely high emissions doesn't appear due to the reason that vegetation cover in this grid box is equal 25%. This reduces the mean South American dust emissions dramatically (from 47 Tg/yr for 6 kyr to 1.1 Tg/yr for 6 kyr Pref). As discussed in section 4.1.4, high dust emissions in 6 kyr result from combination of relatively high wind speed and relatively low soil wetness in one grid box. Emissions from the Australian dust sources is slightly increased in 6 kyr Pref compared to 6 kyr due to slightly different wind speed. This leads to the suggestion of adjusting the function for determination of dust sources to more reliable, for example, exponential function.

Certainly, different emissions in the 6 kyr and 6 kyr Pref simulations lead to different dust deposition over Antarctica. Though difference in mean Southern Hemisphere dust emissions between those two runs is not large due to slightly increased Australian emission in 6 kyr Pref. Dust deposition over Antarctica for 6 kyr is 0.20 Tg/yr in contrast to 0.15 Tg/yr for 6 kyr Pref. The largest difference appears in Atlantic and Indian sectors of Antarctica (Fig.6.1).

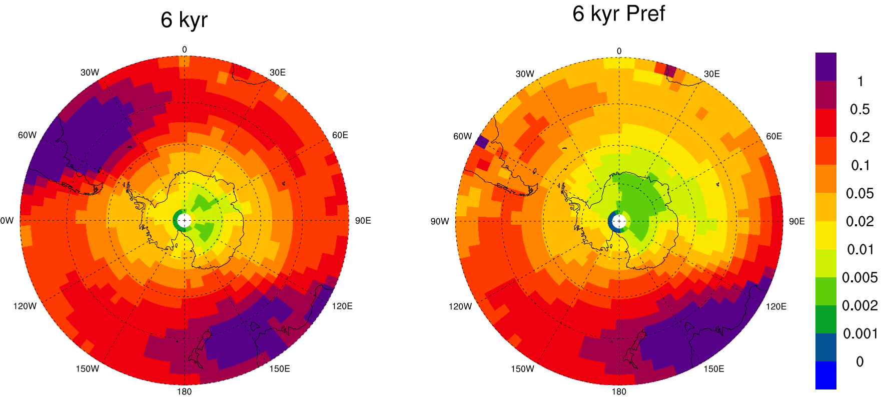

Figure 6.1— Dust deposition [$\mu g/m^2$] in the Southern Hemisphere for the 6 kyr and 6 kyr Pref simulations.

Dust concentration in the Antarctic ice for 6 kyr and 6 kyr Pref were compared with records from three polar sites (Fig.6.2). The model overestimates the mid-Holocene to pre-industrial ratio for all three sites. In 6 kyr Pref, dust concentration in the EDML site is decreased significantly compared to the 6 kyr simulation, but still overestimates observed value. Dust concentration in the Vostok site is decreased as well. Dust concentration in EDC is increased compared to 6 kyr simulation, and even more overestimates the observations. This leads to the idea that the EDML site is under the greater influence of the South American dust source, while for the EDC site the Australian source is more important. For the Vostok location the contribution of both South American and Australian sources is significant. The model overestimates 6 kyr Ref/CTRL deposition ratio due to overestimation of the Australian dust source in 6 kyr Ref and/or underestimation of the South American dust source in CTRL.

Next, mineral dust emissions, atmospheric transport towards the South Pole and dust deposition over Antarctica in the LGM with respect to current climate in this and previous modeling studies are discussed.

In the current study LGM dust emissions are higher by a factor of 2 compared to pre-industrial. Werner et al. (2002) and Mahowald et al. (1999) suggest 2.2-fold and 3.0-fold increase correspondingly. In order to simulate the dust cycle, offline chemical transport models were used in both of these studies. Vegetation information was obtained with different versions of terrestrial biosphere model BIOME. To determine

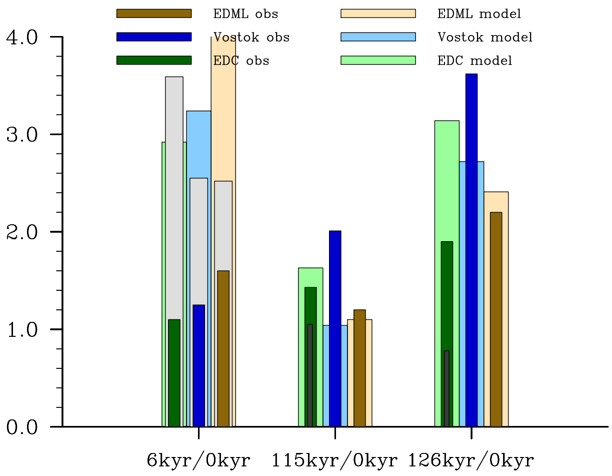

Figure 6.2— The ratio of dust concentration in the ice for the sites Vostok, EDML and EDC from model simulations (dark colors) and observations (light colors) for 6 kyr, 115 kyr and 126 kyr with respect to pre-industrial period. Modeled data from 6 kyr Pref are in light grey.

dust source areas, a similar method in Werner et al. (2002) and our study was used (see details in section 2.2.5). In Mahowald et al. (1999) dust source areas were defined as regions with a seasonal maximum leaf area index of 0.35 m^2m^{-2} or less in the tropics and subtropics and 0.2 m^2m^{-2} in the extratropics.

Smaller LGM/current dust emissions ratio (of about 2.2) is shown by using online dust model later in Mahowald et al. (2006). Dust source areas were determined following Mahowald et al. (1999) by using global vegetation model BIOME3. In that study, the increase of LGM emissions is lower compared to Mahowald et al. (1999) due to smaller source change derived from vegetation. This is highlighting how the modeled dust flux is sensitive to the climate model and/or dust model. Mahowald et al. (2006) also noticed, that satellite-based vegetation is known to underestimate the bare ground fraction for current climate (Bonan et al., 2002). This also shows our pre-industrial simulation with source areas derived from satellite data (the PreVeg run). The global mean dust emissions in PreVeg are slightly reduced compared to CTRL simulation.

During the LGM, continental ice sheets generated large amounts of fine-grained debris (Mahowald et al., 2006). Additional simulation, which besides desert arias includes glaciogenic dust sources, was performed in Mahowald et al. (2006). 6 regions with glaciogenic sources have been included: in Europe, Siberia, South America (Pampas region) and North America (Mississippi River basin, Alaska and Idaho). Including the glaciogenic sources global dust emissions in the LGM increase from 2.2 to 3.3 compared to current climate. Thus, according to Mahowald et al. (2006), approximately 1/3 of the LGM dust emissions comes from glaciogenic sources. Although it has been mentioned that this increase is likely to be sensitive to the model configuration used. Note that they didn't predict the size of these glaciogenic sources from first principles, but rather used the data to constrain the size of these sources. Nevertheless, inclusion in our LGM simulation the addition glaciogenic source in South America can increase LGM dust deposition over Antarctica and improve the agreement between modeled data and observations.

Li et al. (2010) report 2.4-fold increase of LGM global dust emissions compared to current by only change in vegetation and sea level. While applying LGM 10m wind speed, whereas other parameters are similar to current climate, yield just a moderate increase of glacial dust emissions. Vegetation maps compiled from plant fossil and other proxy data for present climate and the LGM were used. Li et al. (2010) mentioned about uncertainty which associated with present day vegetation mask. They claim that by using compiled vegetation mask a much smaller emissions from Australia was obtained (1/4) than by using satellite vegetation. This leads to underestimation of dust deposition in West Antarctica in their study. Our results from the pre-industrial PreVeg simulation with using satellite based vegetation show much higher Australian emissions compared to CTRL as well. This leads to overestimation of dust deposition in Antarctica in the PreVeg simulation. However Australian emissions from CTRL is higher (doubled) compared to Li et al. (2010), when he used compiled vegetation mask and show in general good agreement with observation in Antarctica. In study by Andersen et al. (1998), where present day vegetation data base for both the present and LGM simulations was used, just 1.4-fold increase of LGM emissions is suggested.

The simulated LGM/current ratio of Southern Hemisphere dust emissions is very diverse in various models. Southern Hemisphere dust emissions increase by a factor of 1.6 in Andersen et al. (1998) and by a factor of 2.1 in Werner et al. (2002) in LGM compared to present. While increase by a factor of 6.3 and 9.7 is reported in Albani et al. (2011) and Li et al. (2010) respectively. In our simulations emissions from the Southern Hemisphere dust source increase by a factor of 2.6 in LGM compared to CTRL. This lies in the range given by previous studies. Note, that Albani et al. (2011) included glaciogenic dust sources for the LGM simulation, similar to Mahowald et al. (2006). In Li et al. (2010) the Southern Hemisphere dust source area extent in LGM is 3.8 times the present source area extent, while in our study it is just a factor of 1.5 higher.

In the literature the question about strengthening/weakening of atmospheric dust transport towards Antarctica in the LGM remains open. This topic was investigated by Krinner et al. (2010), based on radon-like tracer concentrations by using inline Eulerian tracer modeling in a general circulation model of the atmosphere. It was suggested that atmospheric transport towards Antarctica is more frequent in the LGM via low level advection, while upper-level advection tends to be higher at present. Earlier study by Krinner and Genthon (2003) shows more frequent fast low-level tracer advection from Patagonia towards Antarctica as a consequence of the more vigorous meridional eddy transport and of the increased vertical atmospheric stability (less convection) during the LGM. However advection of tracers from Australia and southern Africa was suggested to be similar to current climate.

Li et al. (2010) report an increase of dust transport to West Antarctica due to the increase in southward winds west of the Drake Passage. This was supported by Albani et al. (2011), showing more marked transport pathway with a dust plume connecting Patagonia and the Antarctic Peninsula/West Antarctica. However Li et al. (2010) suggested no enhanced dust transport to the East Antarctica. Transport in the LGM is weaker in study by Lunt and Valdes (2001), which indicates a reduced frequency of back trajectories originating over Patagonia, implying a reduced meridional transport of mineral dust to the EDC and Vostok sites. Fischer et al. (2007) suggested only a moderate increase (by 20-30%) of atmospheric transport to Antarctica in the LGM. They reported that changes in transport and atmospheric lifetime can explain just a factor of 1-2 change in aerosol flux in Antarctica. Our study shows strengthening of atmospheric dust transport to Antarctica in the LGM by about factor of 1.5-2 compared to the pre-industrial. This results from seasonally increased cyclonic activity and modification in transport pathways from Patagonia to West Antarctica, which is more pronounced in JJA. Transport is increased in the low- and middle troposphere.

In the current study, dust deposition over Antarctica is a factor of 10.2 higher in the LGM compared to the pre-industrial. This is in broad agreement with Albani et al. (2011). Dust deposition over Antarctica in Li et al. (2010) is 6.3 times higher in the LGM compared to current. Werner et al. (2002) reported 2.7-fold increase of LGM dust deposition at high southern latitudes ($61 - 90° S$).

Chapter 7

Conclusion and Outlook

7.1 Conclusion

In this study, the global aerosol/climate model ECHAM5-HAM was used to investigate the response of the dust cycle to insolation induced climate changes. The dust cycle in the Southern Hemisphere with a particular focus on the Antarctic region has been analyzed for various time-slices. Four of the time-slices represent interglacial conditions: the pre-industrial control simulation (CTRL), the mid-Holocene at 6,000 years BP, the Eemian at 126,000 years BP, and the last glacial inception at 115,000 years BP. Additionally, the last glacial maximum (LGM) at 21,000 years BP was also simulated. Vegetation cover information was derived using a dynamical vegetation model forced with climate data from an earth system model. This study is a first attempt to simulate past interglacial dust cycles.

- *How do mineral dust emissions change in different paleo conditions?*

For all past time-slices, the simulated dust emissions are higher than for the pre-industrial CTRL simulation. Strongest emissions are simulated for the LGM, which are 2 times higher than in CTRL. In all time-slices, global dust emissions are dominated by the Northern Hemisphere sources, which account for more than 90% of total dust emissions.

Southern Hemisphere dust emissions are dominated by the Australian dust source in all interglacial time-slice simulations. In the LGM, the South American dust emissions are almost as strong as the Australian. Maximal increase of emissions in South America in the LGM is due to significantly reduced vegetation cover and lower sea level, which exposes new coastal dust source areas on the Patagonian shelf.

- *Which processes are responsible for the changes of Southern Hemisphere dust emissions?*

Southern Hemisphere dust emissions are increased by factors of 2.5 and 1.8 in the 6 kyr and 126 kyr simulations, respectively, relative to the CTRL run. The dust source area is 20% smaller in 6 kyr and 50% larger in 126 kyr compared to the pre-industrial CTRL. The main contributor to the source area extent change in both time-slices is the Australian source. In the mid-Holocene, dust emissions are enhanced because of the increased probability of high wind speeds over the Australian and parts of the South American dust source areas. Reduced soil wetness also contributes to enhanced dust mobilization. In the Eemian, however, emissions are increased mainly due to an extension of the Australian source area as a consequence of drier austral summers. The likelihood of high wind speeds is also slightly enhanced. In the last glacial inception, intensified summer monsoons over Australia and South America increase vegetation cover, thereby reducing the Southern Hemisphere dust source area by 26%. However, this is compensated by locally rather dry soil and almost unchanged probability density function of wind speed in Australia compared to CTRL. This leads to emissions, which are broadly similar to CTRL. The differences in dust emissions from the South African source are moderate for all time-slices, consistently with the frequency of high wind speed.

- *How does dust deposition over Antarctica changes in the different time-slices?*

In all time-slices simulated dust deposition over Antarctica increased relative to the pre-industrial CTRL. In the mid-Holocene, dust deposition is increased by a factor of 3.8, and in the Eemian by a factor of 2.7. Dust deposition in the last glacial inception is only slightly enhanced. The highest dust deposition in Antarctica is simulated for the LGM, showing a 10.2-fold increase compared to CTRL.

- *What is the contribution of different processes, such as emission, transport and precipitation to dust deposition in Antarctica in the different time-slices?*

Approximately two thirds of the increase in dust deposition over Antarctica for the mid-Holocene and Eemian is attributed to enhanced Southern Hemisphere dust emissions. Slightly increased transport efficiency, especially in SON and DJF, causes the remaining one third of the increase in dust deposition. In 115 kyr, dust deposition over Antarctica is increased by a factor of 1.2 compared to CTRL. This is caused by more intense transport and a slight reduction of precipitation over the Southern Ocean, which reduces the dust loss en route to Antarctica.

In the LGM simulation, dust deposition over Antarctica is increased due to 2.6 times higher Southern Hemisphere dust emissions, 2 times stronger transport and 30% weaker precipitation over the Southern Ocean.

- *How does atmospheric transport towards Antarctica changes in the different time-slices?*

Total low level and middle troposphere transport towards Antarctica are similar in CTRL and 126 kyr, are slightly higher in 6 kyr and higher in 115 kyr. The increase in atmospheric transport in 115 kyr is a consequence of enhanced cyclonic activity and stronger circulation over the Southern Ocean. The increased meridional temperature gradient during the LGM leads to more efficient low-level and middle tropospheric dust transport towards Antarctica compared to the interglacial time-slices. Seasonality of the dust transport in the LGM is less pronounced than in the interglacial periods.

The seasonal cycle of Southern Hemispher emissions is strongly pronounced and shows maximum emissions in austral spring (SON) and summer (DJF). Atmospheric transport from the Southern Hemisphere dust sources towards Antarctica for interglacial and glacial time-slices is more active in austral winter (JJA) and minimal in summer (DJF) for low- and middle troposphere. Thus, atmospheric transport to Antarctica is not in phase with Southern Hemisphere dust emissions in all considered time-slices.

For atmospheric dust transport, transport efficiency is especially important during the seasons with strong dust emissions. Our results show an increase of low- and middle troposphere transport towards Antarctica in SON and DJF in the 6 kyr and 126 kyr simulations. This is due to southward deflection of the transport pathway over the Weddell Sea in 6 kyr and over the Indian sector of the Southern Ocean in 126 kyr as well as due to increased cyclonic activity over the Pacific sector of the Southern Ocean in both time-slices in SON.

The strength and seasonality of air mass transport in the low troposphere is more pronounced than in the middle troposphere. However, in terms of dust transport, middle troposphere is more efficient because it is less affected by precipitation events than low level troposphere.

- *How does synoptic scale eddy fluxes influence transport of dust to Antarctica in different time-slices?*

The contribution of synoptic scale eddy fluxes is significant for the transport of dust towards Antarctica in all investigated time-slices.

- *Altitude of atmospheric transport of dust towards Antarctica in interglacial and glacial time-slices.*

The pressure level of most effective dust transport towards Antarctica is similar for all interglacial time-slices and is at pressure level of about 500 hPa. For the LGM the maximum dust transport to Antarctica is located on a somewhat lower level of about 600 hPa to 700 hPa. The main cause for this is the drier atmosphere and consequently less wet removal of dust from the lower troposphere.

- *What are the dust source regions for dust deposition over Antarctica in different time-slices?*

In 6 kyr and 115 kyr, the air mass trajectories that originated over the Southern Hemisphere dust sources at 800 hPa and reached Antarctica originate mainly over the Australian source, while for trajectories originated at 500 hPa the South American source is slightly stronger. This is similar to the pre-industrial simulation. In 126 kyr the trajectories originated over the Southern Hemisphere dust sources at both 500 hPa and 800 hPa are dominated by the Australian dust source.

In the LGM, the fraction of the trajectories originated at 800 hPa over the Australian and South American sources is similar, while trajectories originated at 500 hPa are fairly dominated by the South American source. In other words, our LGM simulation shows increased transport from Southern America to Antarctica compared to the interglacial time-slices.

- *Does seasonality of dust concentration in the Antarctic ice changes in different time-slices?*

In the interglacial time-slices the dust concentration in the Antarctic ice reaches a maximum in Southern Hemisphere spring (SON), whereas in the LGM simulation the patterns are more complex and dust concentration maxima depends on the region.

- *How well can the model simulate the dust cycle in different climate conditions?*

The modeled dust deposition in the pre-industrial and LGM climate conditions are in general agreement with the reconstructed dust deposition patterns. In Antarctica, the model overestimates observed values by a factor of about 2–3. This is caused by an overestimation of the Australian dust source and too high wet deposition in the Antarctica interior. In the LGM simulation, the model is able to capture the spatial distribution of low- and high deposition regions. In west Antarctica, the model is in good agreement with observations, while in eastern Antarctica the model underestimates dust deposition for the LGM by a factor of about 4–5. The latter can be attributed to an underestimation of the dust source in South America. For the validation of the modeled dust concentration in ice in 6 kyr, 115 kyr and 126 kyr the ratios of dust concentration in three Antarctic sites relative to pre-industrial values were analyzed. The model captures the relative increase in observed dust concentration in ice in 115 kyr and 126 kyr compared to the pre-industrial quite well. However, the model overestimates the 6 kyr to pre-industrial ratio by factor of 2.5 to 5. This is likely due to the overestimation of the south American and Australian sources.

7.2 Outlook

Some of the mechanisms influencing the dust cycle are dependent on the specific model setup, such as spatial resolution. Gläser et al. (2012) show that dust emissions and load are generally better represented in simulations with higher resolution models. However, they noticed that the seasonality of Northern Hemisphere dust emissions is well reproduced independently on the model resolution. To quantify the influence of model resolution on the dust cycle in different climatic conditions high resolution simulations could be performed. This is especially important for the Southern Hemisphere as dust emissions from South America are particularly strongly affected by the specific topographic features, such as the very narrow Andes chain at the West coast. The representation of this specific topography might increase dust mobilization from the Patagonian region in the LGM and could improve the simulation of dust deposition in Antarctica. Moreover, the representation of the Australian dust source could also benefit from a finer horizontal resolution.

The influence of mineral dust on the radiative balance of the Earth in different time-slices is also a subject of interest. To estimate the potential effect, a set of simulations for the same time-slices, but without inclusion of mineral dust could be performed. The subsequent comparison can provide valuable information about the impact of mineral dust on radiative balance of the Earth.

The results of this study show that the representation of dust source areas by a step-function like dependence on the vegetation cover has its drawbacks. In future studies a smoother transition should be applied. This is of particular importance for low resolution simulations.

The Southern Annual Mode (SAM) seems to have an impact on processes influencing the dust cycle. Preliminary results show a dependency of dust transport towards Antarctica on the SAM, which is different for individual time-slices. To further examine this dependency, a detailed analysis of dust concentration in Antarctic ice cores and their relation to the SAM is required. The understanding of the SAM contribution can provide additional explanation to the Antarctic dust deposition variability on different time-slices and may allow the reconstruction of a SAM index from high resolution records of dust depostion in Antarctic ice cores.

Appendix A

2m air temperature difference, global maps

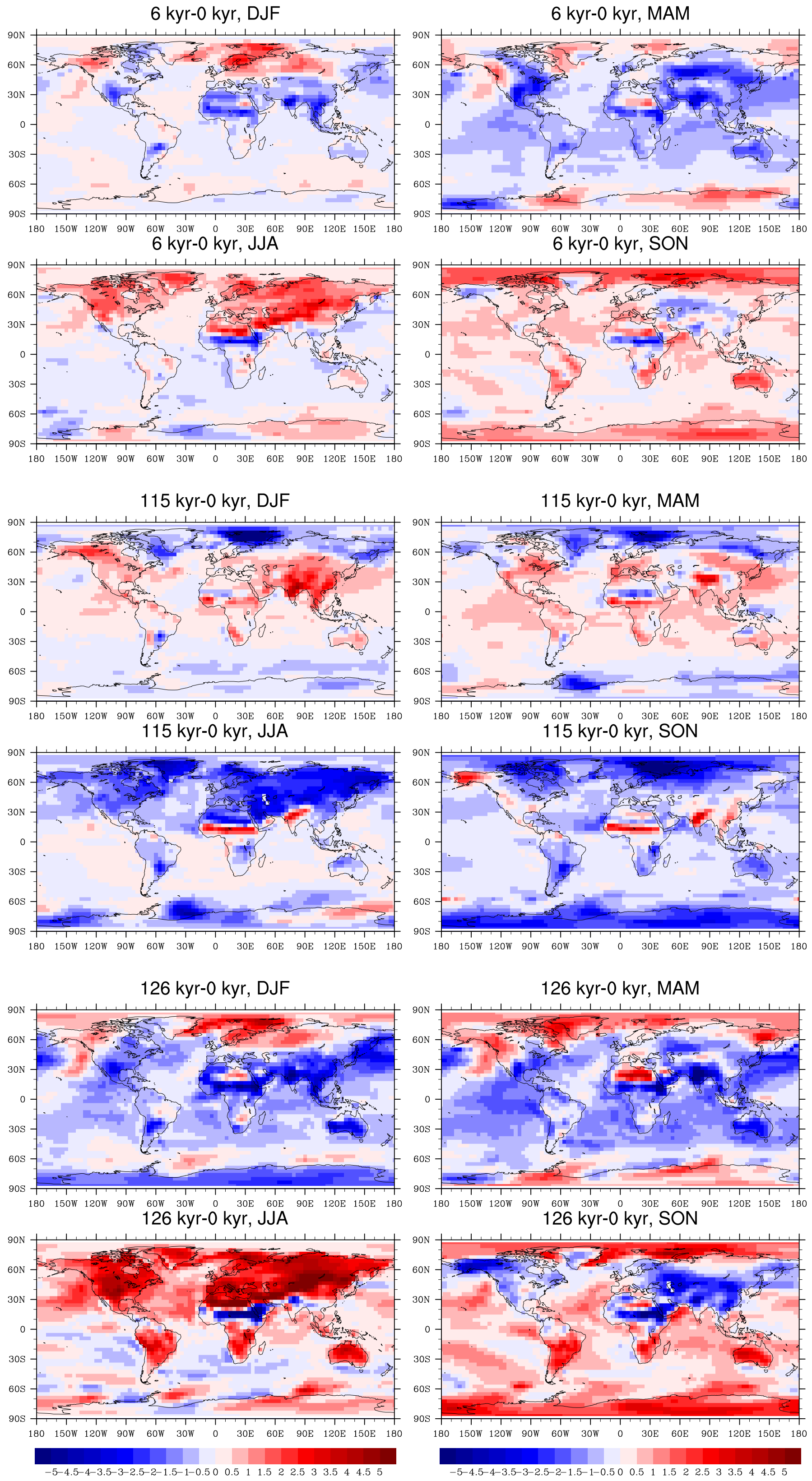

6 kyr-0 kyr, DJF

6 kyr-0 kyr, MAM

6 kyr-0 kyr, JJA

6 kyr-0 kyr, SON

115 kyr-0 kyr, DJF

115 kyr-0 kyr, MAM

115 kyr-0 kyr, JJA

115 kyr-0 kyr, SON

126 kyr-0 kyr, DJF

126 kyr-0 kyr, MAM

126 kyr-0 kyr, JJA

126 kyr-0 kyr, SON

Figure A.1— Seasonal average 2m air temperature difference between the 6 kyr, 115 kyr, 126 kyr and CTRL simulations.

Appendix B

Precipitation difference, global maps

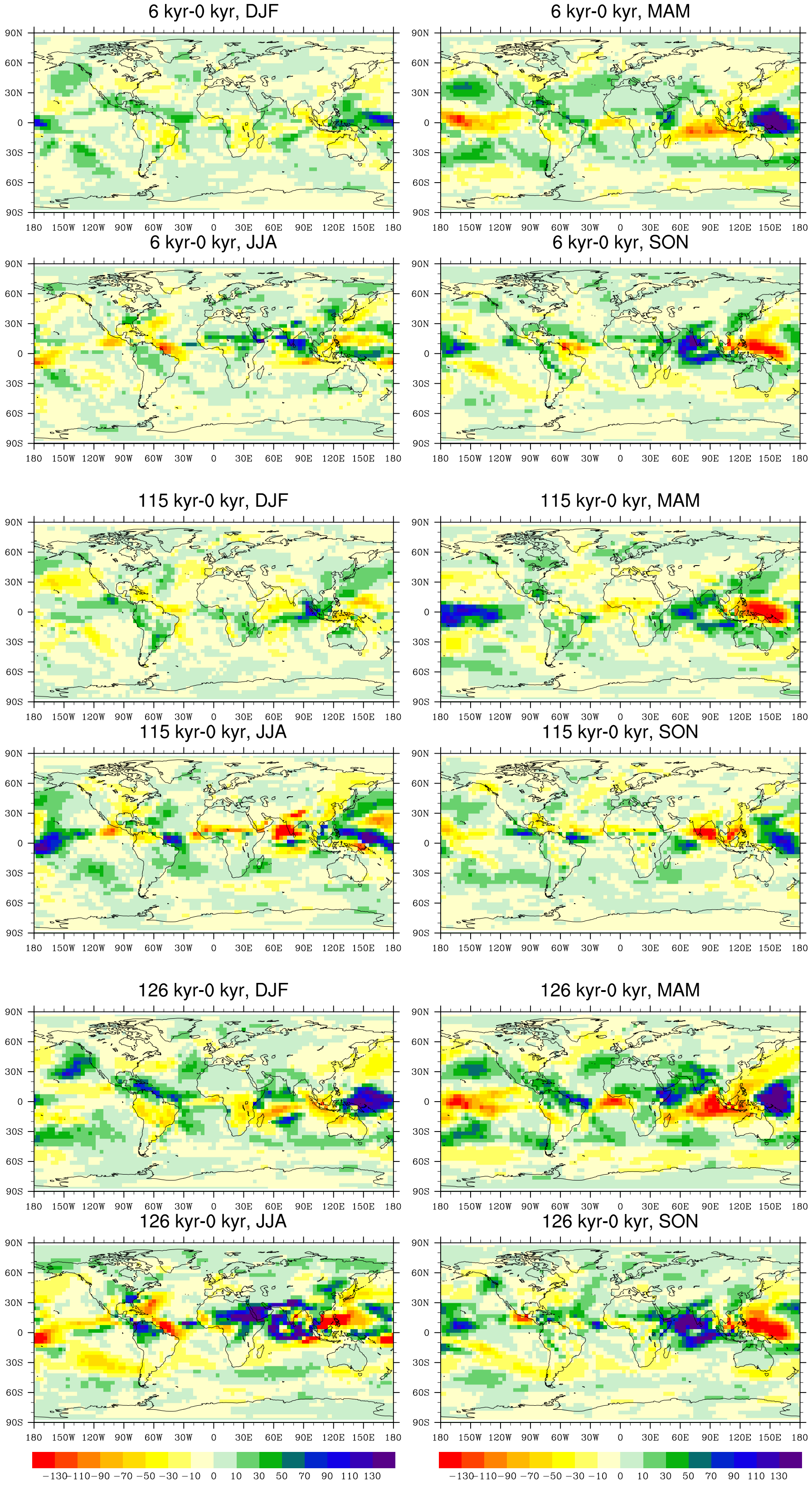

Figure B.1— Seasonal average precipitation difference between the 6 kyr, 115 kyr, 126 kyr and CTRL simulations.

Appendix C

Precipitation difference over the Antarctic region

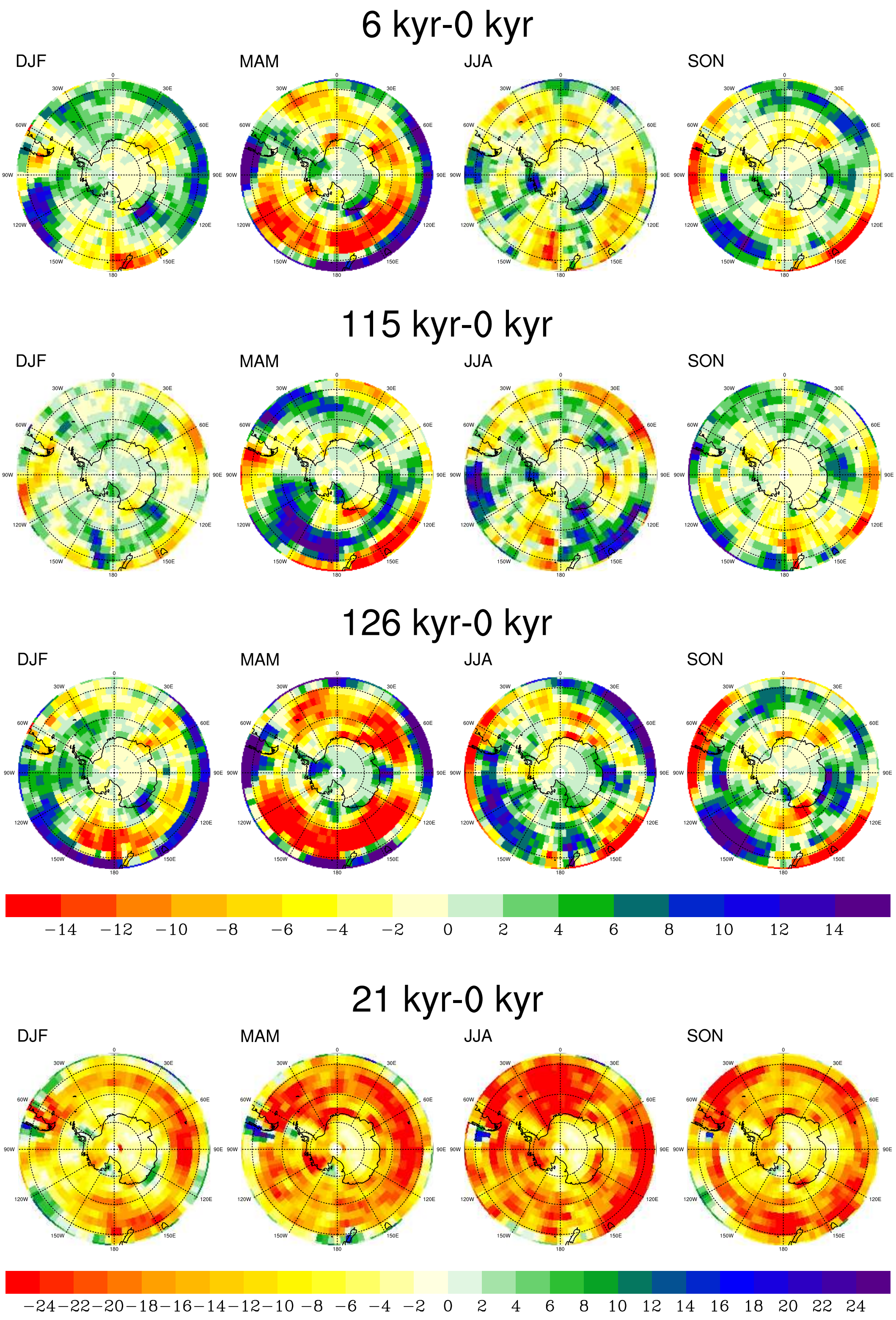

Figure C.1— Seasonal average precipitation difference over the Antarctic region [mm/month] between the 6ky, 115ky, 126ky, LGM and CTRL simulations. Note different scales.

Appendix D

STD of bandpassed 500 hPa geopotential height

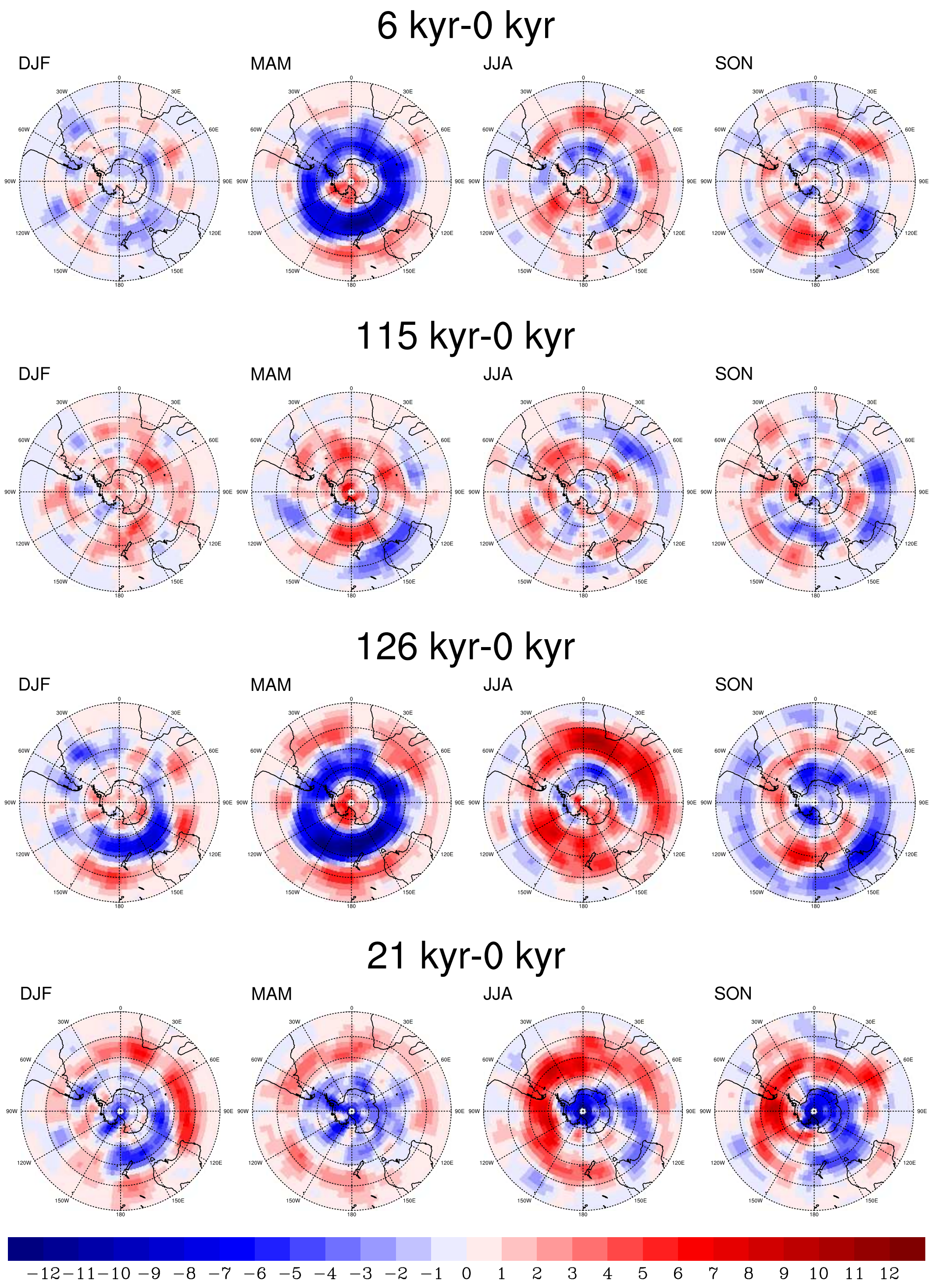

Figure D.1— Seasonal mean standard deviation of 500 hPa geopotential height [m], due to transient eddies in the bandpass regime from 2.5 to 6 days for the Southern Hemisphere shown as a difference between the 6 kyr, 115 kyr 126 kyr, LGM and CTRL simulations.

Appendix E

Dust transport

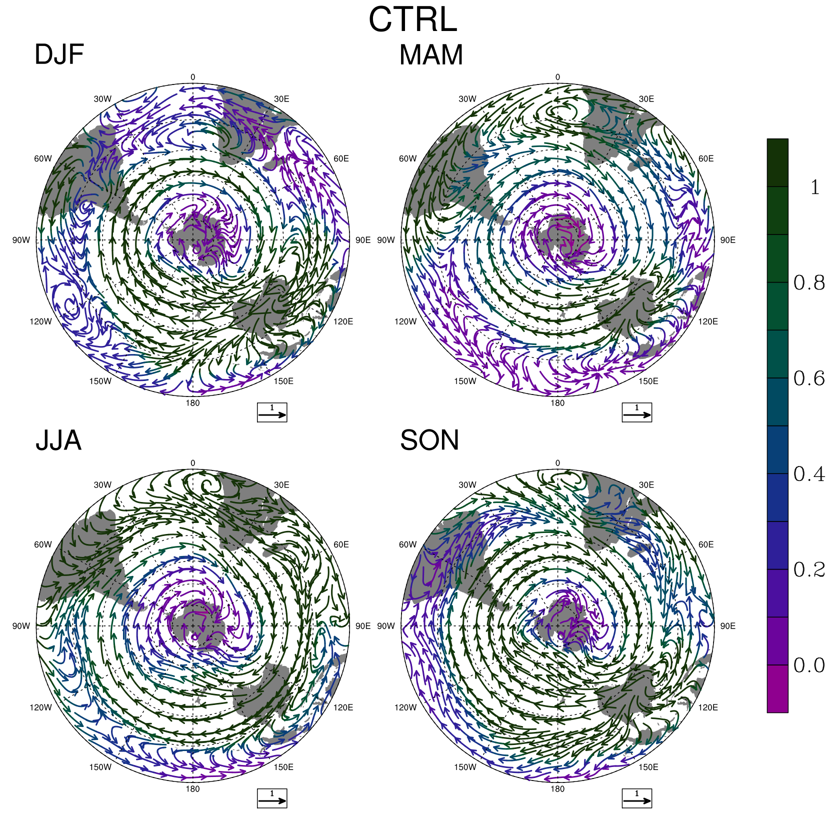
CTRL
DJF
MAM
JJA
SON
0
30E
60E
90E
120E
150E
180
150W
120W
90W
60W
30W
1
1
0.8
0.6
0.4
0.2
0.0

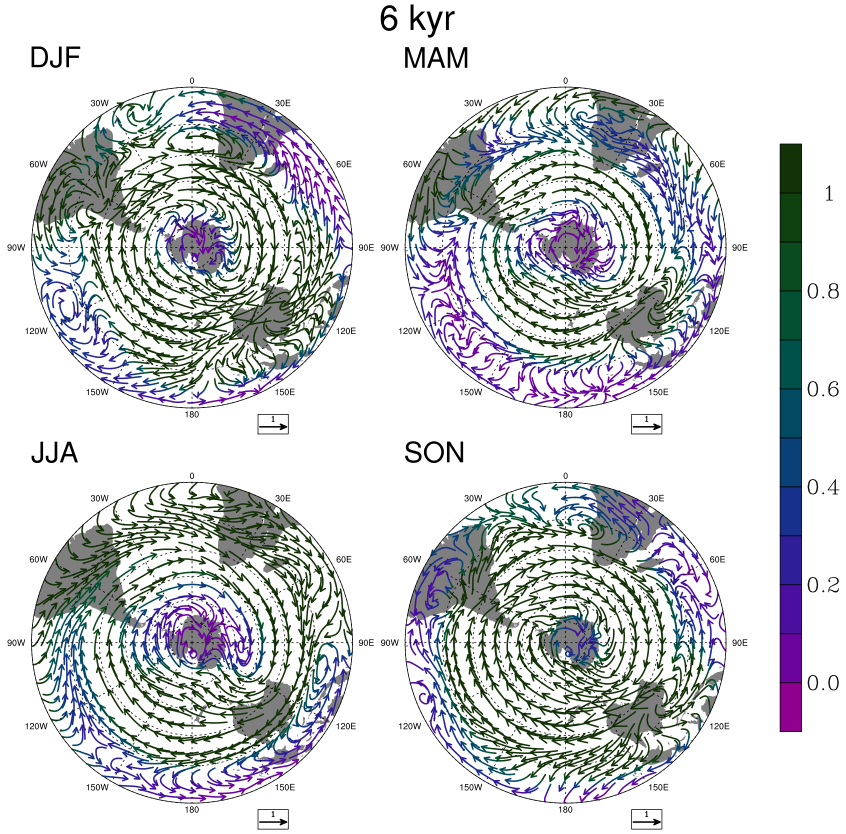
6 kyr
DJF
MAM
JJA
SON
0
30E
60E
90E
120E
150E
180
150W
120W
90W
60W
30W
1
1
0.8
0.6
0.4
0.2
0.0

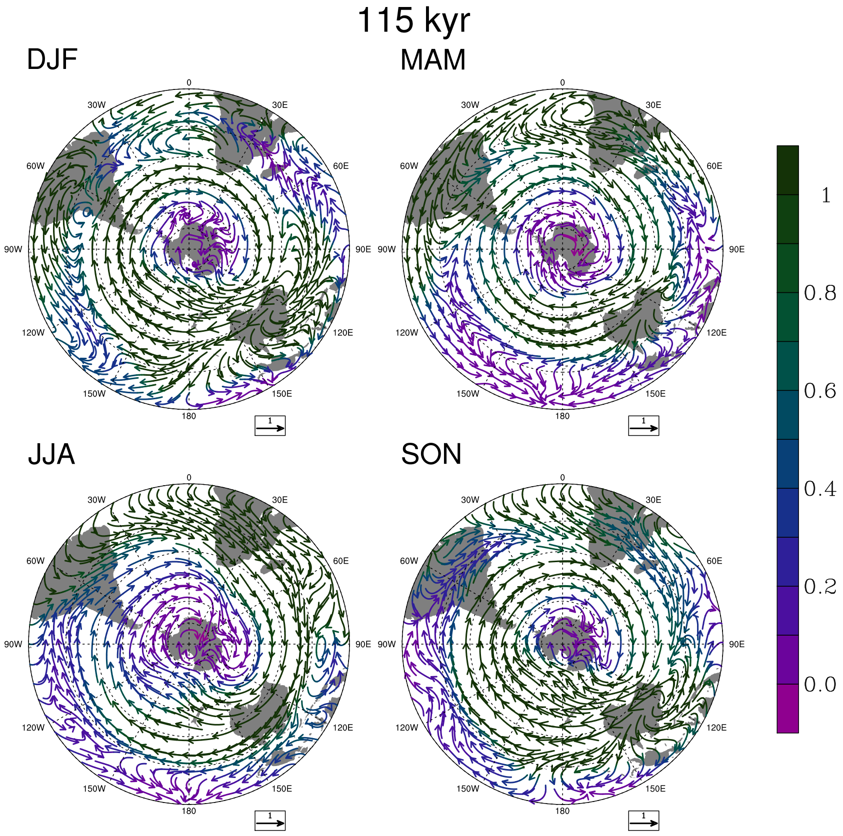

115 kyr

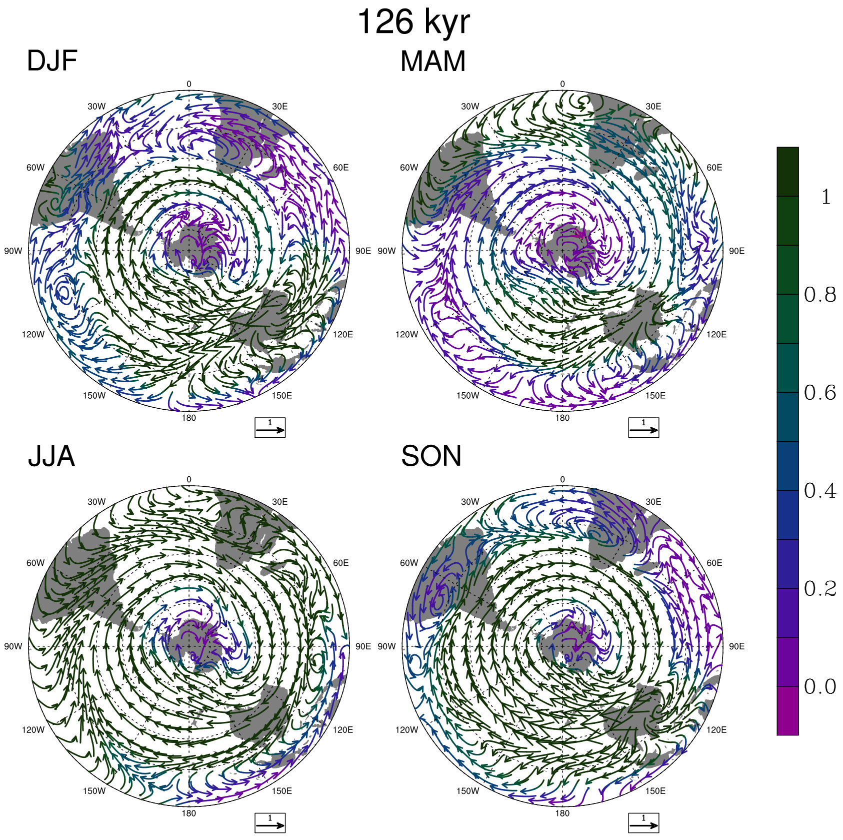

126 kyr

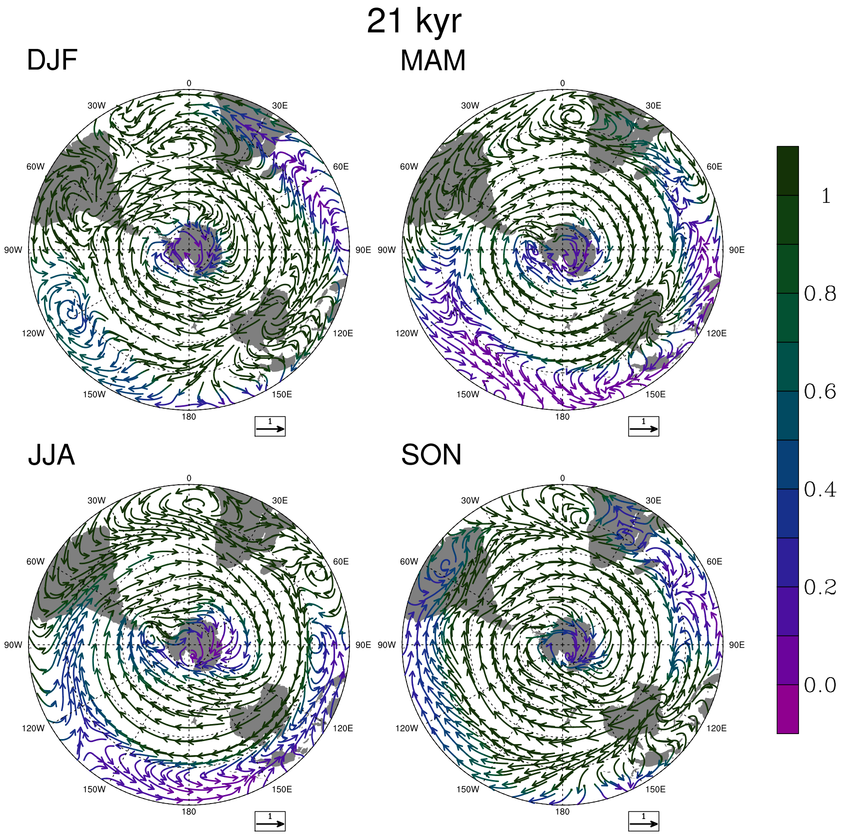

Figure E.1— Dust transport on 500 hPa calculated by using 6 hourly data for the interglacial and glacial simulations.

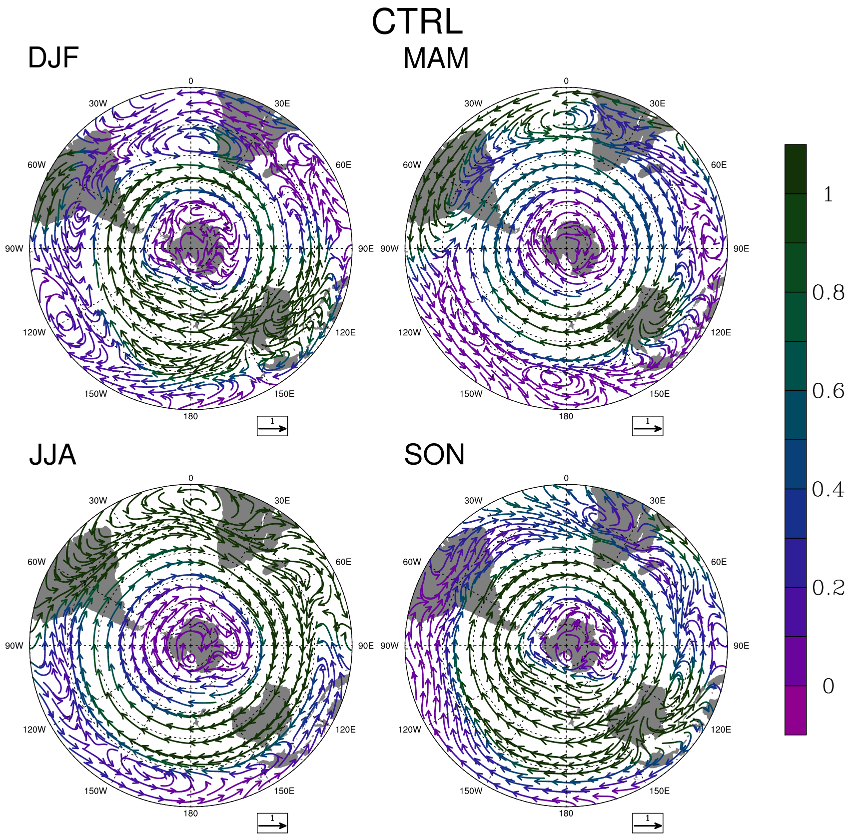
CTRL
DJF
MAM
JJA
SON
0
30E
60E
90E
120E
150E
180
150W
120W
90W
60W
30W
1
1
0.8
0.6
0.4
0.2
0

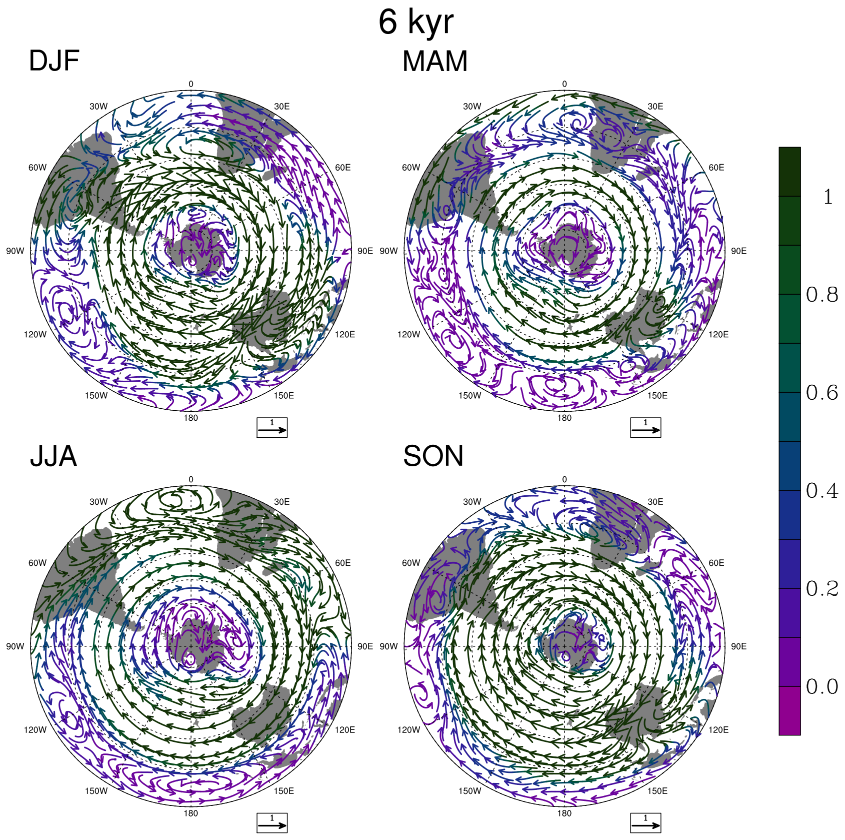
6 kyr
DJF
MAM
JJA
SON
0
30E
60E
90E
120E
150E
180
150W
120W
90W
60W
30W
1
1
0.8
0.6
0.4
0.2
0.0

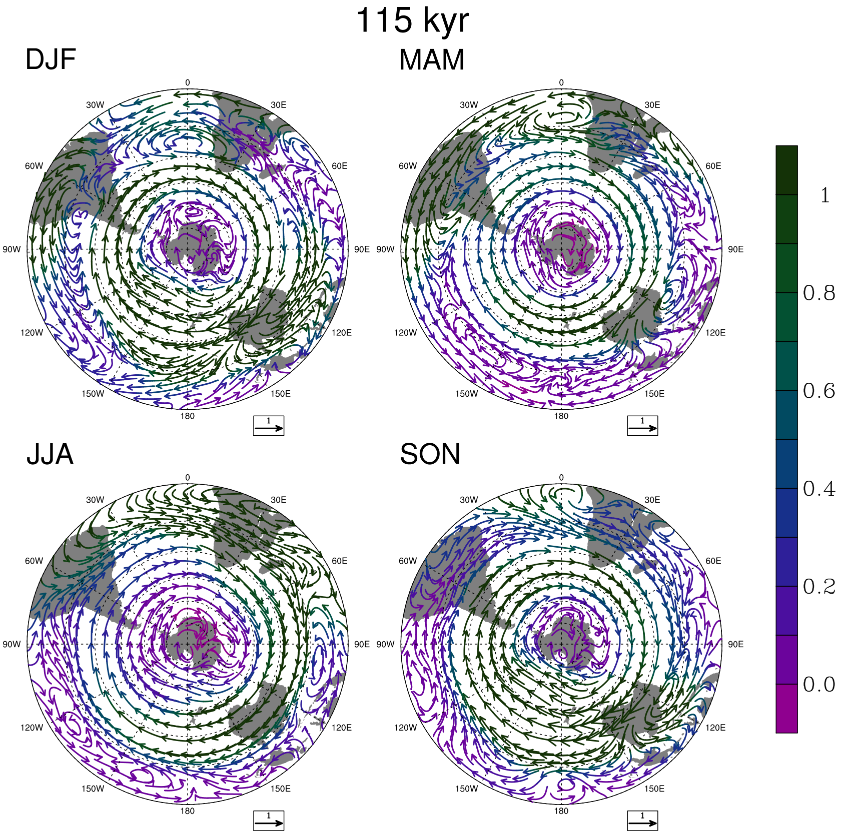
115 kyr
DJF
MAM
JJA
SON
0
30E
60E
90E
120E
150E
180
150W
120W
90W
60W
30W
1
1
0.8
0.6
0.4
0.2
0.0

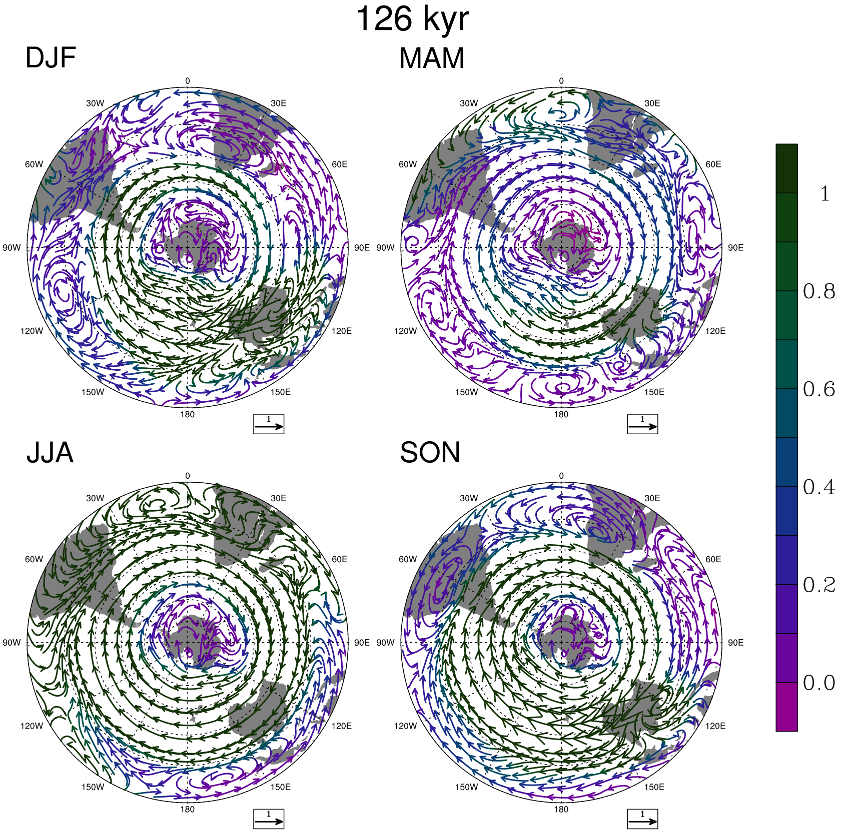
126 kyr
DJF
MAM
JJA
SON
0
30E
60E
90E
120E
150E
180
150W
120W
90W
60W
30W
1
1
0.8
0.6
0.4
0.2
0.0

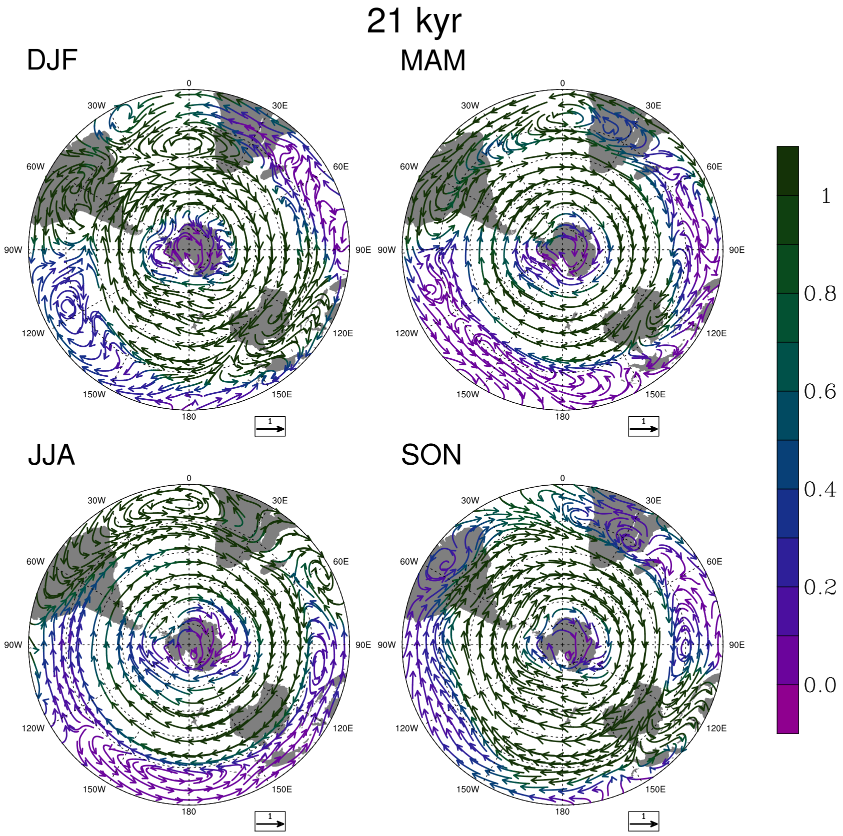

Figure E.2— Dust transport on 500 hPa calculated by using monthly mean data for the interglacial and glacial simulations.

Appendix F

Eolian fluxes from marine sediment data

Table F.1— Eolian fluxes to Sediment Traps

Sample ID	$Longitude,^{\circ} E$	$Latitude,^{\circ} N$	Average Annual Lith Fluxes, gm^2yr^-1	Reference
WS-4	-2.59	-64.93	0.52	Wefer and Fischer, 1991
$^*WS-3$	-2.56	-64.90	4.82	Wefer and Fischer, 1991
$^*WS-1$	-34.76	-62.44	0.00	Fischer et al., 1988
$^*KGIlower$	-57.53	-62.26	53.50	Wefer et al., 1988
$^*AO$	150.50	-61.50	6.50	Noriki and Tsunogai, 1986
$^*PF1$	5.77	-50.15	9.74	Wefer and Fischer, 1991
Site13shallow	161.00	-35.52	1.24	Kawahata and Ohta,2000
WR1	9.17	-20.07	5.80	Wefer and Fischer, 1993
WR2 lower	9.16	-20.05	2.50	Wefer and Fischer, 1993
WR2 upper	9.16	-20.05	3.80	Wefer and Fischer, 1993
$^*Site12deep$	154.83	-17.76	0.29	Kawahata and Ohta,2000
Site12shallow	154.83	-17.76	0.40	Kawahata and Ohta,2000
Site11shallow	155.99	-12.99	0.73	Kawahata and Ohta,2000
GBZ4	-9.90	-2.18	1.20	Wefer and Fischer, 1993
$^*SEPS-03lower$	175.00	0.00	1.68	Harada et al., 2001
SEPS-03 upper	175.00	0.00	0.92	Harada et al., 2001
$^*Site3lower$	175.16	0.00	0.58	Kawahata et al., 1998a
Site3upper	175.16	0.00	0.73	Kawahata et al., 1998a
Site10	160.57	1.22	0.84	Kawahata et al., 2000
$^*GBN3lower$	-11.13	1.79	8.10	Wefer and Fischer, 1993
GBN3 upper	-11.13	1.79	4.30	Wefer and Fischer, 1993
$^*Site1lower$	135.03	3.00	12.67	Kawahata et al., 1998b
$^*Site1upper$	135.03	3.00	11.41	Kawahata et al., 1998b
$^*Site2shallow$	136.28	4.13	3.36	Kawahata et al., 2000
$^*Site2deep$	136.28	4.13	5.92	Kawahata et al., 2000
$^*ECC-B$	138.83	5.01	0.31	Krempe and Knaack, 1996
ECC-T	138.83	5.01	0.57	Krempe and Knaack, 1996
PB2	-85.58	5.37	4.80	Honjo, 1982
$^*Site4lower$	175.01	7.93	0.29	Kawahata et al., 1998a
$^*Site4upper$	175.01	7.93	0.37	Kawahata et al., 1998a
M5	65.00	10.00	1.50	Clemens, 1998
CV 1 upper	-21.02	11.48	22.62	Ratmeyer et al., 1998
$^*CV1lower$	-21.02	11.48	10.37	Ratmeyer et al., 1998
$^*NEC-B$	134.29	12.02	0.52	Krempe and Knaack, 1996
NEC-T	134.29	12.02	0.11	Krempe and Knaack, 1996
Cast	64.77	14.48	4.30	Ramaswamy et al., 1991 Haake et al., 1993
East	68.75	15.47	7.40	Ramaswamy et al., 1991 Haake et al., 1993
M4	61.50	15.98	4.50	Clemens, 1998
Wast	60.47	16.25	6.10	Ramaswamy et al., 1991 Haake et al., 1993
M2/M3	58.80	17.40	12.40	Clemens, 1998
$^*EP11$	-117.00	17.50	0.90	Noriki and Tsunogai, 1986
Eumeli mesotrophic	-21.08	18.50	18.74	Bory and Newton (2000)
BOFS-1	-20.17	19.00	21.55	Bory and Newton (2000)
$^*BOFS-1$	-20.18	19.00	27.40	ickells et al., 1996
CB1-1	-19.75	20.92	21.92	Fischer et al., 1996
CB1-2	-19.74	20.92	27.20	Jickells et al., 1996 Wefer and Fischer, 1993
CB1-3	-19.74	20.92	11.39	Ratmeyer et al., 1999

Table F.2— (continued)

Sample ID	$Longitude, ^\circ E$	$Latitude, ^\circ N$	Average Annual Lith Fluxes, gm^2yr^-1	Reference
Eumeli oligotrophic	-31.17	21.05	3.73	Bory and Newton (2000)
CB2-1	-20.68	21.15	19.70	Fischer et al., 1996
CB2-2	-20.69	21.15	20.48	Ratmeyer et al., 1998
22N25W	-25.23	21.93	6.70	Kremling and Streu, 1993 Jickells et al., 1996
25N23W	-22.83	24.55	5.21	Jickells et al., 1996
28N22W	-21.98	28.00	2.40	Jickells et al., 1996
CI 1 upper	-15.45	29.11	4.15	Ratmeyer et al., 1998
$^*CI1lower$	-15.45	29.11	7.75	Ratmeyer et al., 1998
Site6	175.00	30.00	3.00	Kawahata et al., 1998a
$^*EP5$	-127.60	31.00	0.80	Noriki and Tsunogai, 1986
$^*SB-1$	137.08	31.53	21.40	Saito et al., 1992
ST	-24.67	31.55	2.36	Lampitt, 1992
$^*EP7$	-124.60	31.70	1.10	Noriki and Tsunogai, 1986
SARGASSO	-64.25	32.08	1.90	Jickells et al., 1998
L1-93	-21.98	33.15	1.17	Kuss and Kremling, 1999
L1-93	-21.98	33.15	2.34	Kuss and Kremling, 1999
34N21W	-21.02	33.82	4.75	Honjo and Manganini, 1993 Jickells et al., 1996
$^*Site5lower$	177.74	34.42	6.79	Kawahata et al., 1998a
Site5upper	177.74	34.42	3.25	Kawahata et al., 1998a
$^*Site7lower$	174.95	37.40	7.93	Kawahata et al., 1998a
Site7upper	174.95	37.40	8.77	Kawahata et al., 1998a
WP-3	145.43	40.00	7.32	Saito et al., 1992
$^*WP-1$	146.47	40.52	16.10	Saito et al., 1992
$^*JS$	138.70	40.83	4.90	Saito et al., 1992
$^*WP$	146.50	41.50	21.70	Noriki and Tsunogai, 1986
$^*WP-2$	150.23	43.00	1.80	Saito et al., 1992
Site8	175.03	46.12	4.09	Kawahata et al., 1998a
NP-B	162.12	46.82	0.86	Saito et al., 1992
48N21W-1	-20.87	47.72	3.10	Honjo and Manganini, 1993 Jickells et al., 1996
48N21W-2	-19.50	47.83	2.80	Jickells et al., 1996
P	-144.98	50.00	0.30	Fischer et al., 1988 Honjo, 1982
$^*L3-92$	-21.15	54.58	1.02	Kuss and Kremling, 1999
$^*L3-93$	-21.15	54.58	1.83	Kuss and Kremling, 1999
$^*75N7W$	-6.72	74.58	3.10	Fischer et al., 1988
$^*79N1E$	1.37	78.87	4.00	Fischer et al., 1988

The asterisk (*) indicates site not used.

Table F.3— Eolian fluxes to Marine Sediment

Site	*Longitude*,° *E*	*Latitude*,° *N*	"Modern" flux, gm^2yr^-1	LGM/ Modern ratio	Reference
RC27-61	59.9	16.6	4.8	3.3	Clemens and Prell, 1990
ODP 722B	59.8	16.6	12.9	1.4	Clemens and Prell, 1991
V21-146	163.0	37.7	1.9	1.1	Hovan et al., 1991
KK75-02	179.3	38.6	2.4	0.8	Janacek and Rea, 1985
DSDP 578	150.0	32.0	17.9	0.8	Janacek, 1984
DSDP 578	150.0	32.0	17.9	0.8	Janacek, 1984
V19-188	60.7	6.9		2.7	Kolla and Biscaye, 1977
RC11-147	112.7	-19.0		2.6	Kolla and Biscaye, 1977
V21-148	160.6	42.1		1.1	Leinen, 1989
V21-151	163.6	52.3		1.8	Leinen, 1989
V21-171	-164.9	49.9	2.1	1.2	Leinen, 1989
V21-172	164.4	47.0		0.9	Leinen, 1989
V21-173	163.6	44.4		1.1	Leinen, 1989
V24-109	158.8	0.4		1.2	Leinen, 1989
V28-203	-179.4	1.0		3.3	Leinen, 1989
V28-238	160.5	1.0		2.4	Leinen, 1989
V28-239	159.2	3.2		1.6	Leinen, 1989
V28-243	138.5	11.1		1.0	Leinen, 1989
V28-255	142.4	20.1		1.0	Leinen, 1989
RC14-105	157.6	39.7	6.6	1.1	Rea and Leinen, 1988
RC10-167	150.4	33.4	4.2		Rea and Leinen, 1988
V20-122	161.7	46.6	4.9	1.3	Rea and Leinen, 1988
V20-126	155.9	42.2	5.6	2.4	Rea and Leinen, 1988
V20-129	156.6	37.7	10.1	1.1	Rea and Leinen, 1988
V28-294	140.0	28.4	0.6	3.8	Rea and Leinen, 1988
503B	-95.6	4.0	0.3	1.2	Rea et al., 1986
ODP 663	-11.9	-1.2	2.0	3.0	Ruddiman and Janacek, 1989
ODP 663	-11.9	-1.2	2.0	3.4	Ruddiman and Janacek, 1989
V25-59	-33.5	1.4	4.7	3.1	Ruddiman, 1997
RC13-189	-30.0	1.9	4.7	3.3	Ruddiman, 1997
V30-40	-23.2	-0.2	2.5	2.0	Ruddiman, 1997
V30-41K	-23.1	-0.2	3.1	1.0	Ruddiman, 1997
V30-49	-21.1	18.4	6.0	2.0	Ruddiman, 1997
V30-51K	-19.9	19.9	6.2	0.8	Ruddiman, 1997
V22-182	-17.3	-0.5	2.9	1.6	Ruddiman, 1997
V22-177	-14.6	-7.7	2.2	1.0	Ruddiman, 1997
RC24-01	-13.4	0.6	2.2	4.0	Ruddiman, 1997
RC24-07	-11.9	-1.3	3.8	3.7	Ruddiman, 1997
RC24-16	-10.2	-5.0	2.2	1.1	Ruddiman, 1997
V29-144	6.0	-0.2	10.2	0.6	Ruddiman, 1997
76125	75.3	8.6	20.5		Sirocko et al., 1991
76127	73.9	12.1	17.9	0.6	Sirocko et al., 1991
76128	73.3	13.1	63.1		Sirocko et al., 1991
76135	50.5	14.4	74.0	0.8	Sirocko et al., 1991
76136	46.8	12.9	34.2	3.0	Sirocko et al., 1991
77191	76.7	7.5	141.6		Sirocko et al., 1991
77194	75.2	10.5	116.0		Sirocko et al., 1991
77200	67.9	16.5	15.8	1.1	Sirocko et al., 1991
77202	60.7	19.2	45.7	2.3	Sirocko et al., 1991
77203	59.6	20.7	121.8	2.7	Sirocko et al., 1991
114KK	51.2	8.0	14.2	1.1	Sirocko et al., 1991

Table F.4— (continued)

Site	*Longitude,° E*	*Latitude,° N*	"Modern" flux, gm^2yr^-1	LGM/ Modern ratio	Reference
11KL	60.2	5.4	6.5	1.7	Sirocko et al., 1991
143KK	44.8	1.2	94.7	0.3	Sirocko et al., 1991
162KK	40.5	-4.1	2.6		Sirocko et al., 1991
169SK	53.6	-3.6	4.1		Sirocko et al., 1991
181SK	71.1	7.5	20.3		Sirocko et al., 1991
182SK	73.7	8.8	8.4	2.2	Sirocko et al., 1991
18KL	67.3	1.9	2.7	1.0	Sirocko et al., 1991
232SK	64.6	21.8	33.6		Sirocko et al., 1991
26KL	68.8	15.5			Sirocko et al., 1991
36KL	69.0	17.1	5.5	1.5	Sirocko et al., 1991
43GB	69.0	17.9	8.7		Sirocko et al., 1991
51KL	65.6	21.0	20.0	3.6	Sirocko et al., 1991
57KL	63.1	20.9	23.1	3.3	Sirocko et al., 1991
64KL	64.7	19.1			Sirocko et al., 1991
70KL	61.7	17.5			Sirocko et al., 1991
71KL	60.3	16.2	16.9		Sirocko et al., 1991
74KL	57.4	14.3	24.4	2.6	Sirocko et al., 1991
79KL	58.3	13.6			Sirocko et al., 1991
82KL	58.7	12.7	18.6	2.3	Sirocko et al., 1991
87KL	57.7	10.5	11.4	1.3	Sirocko et al., 1991
IOE 105KK	53.5	11.3	10.5	0.9	Sirocko et al., 1991
Meteor 5 422-6	59.0	24.4	118.6		Sirocko et al., 1991
ORGON 4 KS8	59.2	23.5	133.1	1.1	Sirocko et al., 1991
OSIRIS 76123	78.7	6.4	14.6	0.9	Sirocko et al., 1991
SO 28 5KL	61.1	6.7	3.4	3.4	Sirocko et al., 1991
SO 42 15KL	64.8	14.9	7.9	1.7	Sirocko et al., 1991
ODP 658	-18.6	20.7	104.9	1.4	Tiedemann et al., 1989
ODP 659	-21.0	18.1	14.7	1.6	Tiedemann et al., 1989
V22-196	-19.0	13.8		5.9	Kolla et al., 1979
V22-195	-19.4	13.4		5.0	Kolla et al., 1979
A180-73	-23.0	0.2		6.0	Kolla et al., 1979
A180-74	-24.2	0.0		5.0	Kolla et al., 1979
V27-248	-11.8	3.0		3.0	Kolla et al., 1979
V27-175	-22.1	8.8		3.8	Kolla et al., 1979
V180-39	-19.3	25.8		2.0	Kolla et al., 1979
R5-54	-19.0	25.9		1.4	Kolla et al., 1979
V19-248	4.8	-24.6		1.0	Kolla et al., 1979
E39.75	161.2	-36.5	3.0	2.7	Hesse, 1994
SO36-61	161.4	-30.6	0.2	3.0	Hesse, 1994
E26.1	168.3	-40.3	0.8	7.5	Hesse, 1994

Bibliography

Adhemar J.A., Revolutions de la mer, deluges periodiques, Carilian-Goeury et V.Dalmont, Paris, 184 pp., 1842.

Albani S., Mahowald N.M., Delmonte B., Maggi V., Winckler G.: Comparing modeled and observed changes in mineral dust transport and deposition to Antarctica between the Last Glacial Maximum and current climate, Clim. Dym., DOI 10.1007/s00382-011-1139-5, 2011.

Andersen K.K., Armengaud A. and Genthon C.: Atmospheric dust under glacial and interglacial conditions, Geoph. Res. Letters, 25, 13, 2281-2284, 1998.

Arimoto R.: Eolian dust and climate: relationships to sources, tropospheric chemistry, transport and deposition, Earth-Science Reviews, 54 (1-3), 29-42, 2001.

Arpe K., Leroy S.A.G. and Mikolajewicz U.:The last glacial maximum locations of summer-green tree refugia using simulations with ECHAM3 T42 uncoupled, ECHAM5 T31 coupled and ECHAM5 T106 uncoupled models, Clim. Past Discuss., 6, 537584, 2010.

Balkanski Y., Schulz M., Claquin T., Moulin C. and Ginoux P.: Emission of atmospheric trace compounds, chap. Global emissions of mineral aerosol: formulation and validation using satellite imagery, 239-267, Ed. Kluwer, 2004.

Balkanski Y., Schulz M., Claquin T. and Guibert S.: Reevaluation of mineral aerosol radiative forcings suggests a better agreement with satellite and AERONET data, Atmos. Chem. Phys., 7, 81-95, 2007.

Bauer E., Ganopolski A.: Aeolian dust modeling over the past four glacial cycles with CLIMBER-2, Global and Planetary Ghange, 74, 49-60, 2010.

Berger, A.: Long-Term Variations Of Daily Insolation And Quaternary Climatic Changes. Journal of the Atmospheric Sciences, 35 (12), 23622367, 1978.

Berger A. (1987), Long-term variations of earth's orbital elements. Celestial Mechanics, 15(1), 53-74

Berger A.: Milankovitch theory and climate, Reviews of geophysics, vol. 26, no. 4, 624-657, 1988.

Berthelot B., Dedieu G., Cabot F. and Adam S.: Estimation of surface reflectance and vegetation index using NOAA/AVHRR: Methods and results at global scale, ISPRS, Wal d'Isere, France, 1994.

Bonan G.B., Levis S., Kergoat L., Oleson K.: Landscapes as patches of plant functional types: An integrating concept for climate and ecosystem models, Global Biogeochim. Cycles, 16(2), 2002.

Bory A., Wolff E., Mulvaney R., Jagoutz R., Wegner A., Ruth U., Elderfield H.: Multiple sources supply eolian mineral dust to the Atlantic sector of coastal Antarctica: Evidence from recent snow layers at the top of Berkner Island ice sheet, Earth and Planetary Science Letters, 291(1-4), 138-148, 2010.

Braconnot P., Otto-Bliesner B., Harrison S., Joussaume S., Peterchmitt J.Y., Abe-Ouchi A., Crucifix M., Driesschaert E., Fichefet Th., Hewitt C. D., Kageyama M., Kitoh A., Lan A., Loutre M.F., Marti O., Merkel U., Ramstein G., Valdes P., Weber S.L., Yu Y. and Zhao Y.: Results of PMIP2 coupled simulations of the Mid-Holocene and Last Glacial Maximum Part 1: experiments and large-scale features, Clim. Past. 3, 261-277, 2007.

Braswell B.H., Schimel D.S., Linder E. and Moore B.: The response of global terrestrial ecosystems to interannual temperature variability, Science, 278, 870-872, 1997.

Broccoli A.J., Dahl K.A., Stouffer R.J.: Response of the ITCZ to Northern Hemisphere cooling, Geoph. Res. Letters, 33, L01702, 2006.

Broecker W.S. and Henderson G.M.: The sequence of events surrounding Termination II and their implications for the cause of glacial-interglacial CO2 changes, Paleoceanography, 13(4), 352-364, 1998.

Burn-Nunes L.J., Vallelonga P., Loss R.D., Burton G.R., Moy A., Curran M., Hong S., Smith A.M., Edwards R., Morgan V.I., Rosman K.J.R.: Seasonal variability in the input of lead, barium and indium to Law Dome, Antarctica, Geochimica et Cosmochimica Acta 75:1-20, 2011.

Claquin T., Schulz M. and Balkanski Y.: Modeling the minerlaogy of atmospheric dust sources, J. Geophys. Res., 104, 22243-22256, 1999.

Clemens S.C. and Prell W.L.: Late Pleistocene variability of Arabian Sea summer monsoon winds and continental aridity: Eolian records from the lithogenic component of deep-sea sediments, Paleoceanography, 5, 109-145, 1990.

Coe M.T.: A linked global model of terrestrial hydrologic processes: Simulation of modern rivers, lakes, and wetlands, J. Geophys. Res., 103, 8885-8899, 1998.

Croll J.: Climate and Time, in their Geological Relations: A Theory of Secular Changes of the Earth's Climate, D.Appleton & Co., New York, 577 pp., 1875.

Delmonte B., Baroni C., Andersson P.S., Schoberg H., Hansson M., Aciego S., Petit L.-R., Albany S., Mazzola C., Maggi V. and Frezzotti M.: Aeolian dust in the Talos Dome ice core (East Antarctica, Pacific/Ross Sea sector): Victoria Land versus remote sources over the last two climate cycles, J. quaternary science, 25(8), 1327-1337, 2010.

Dentener F.J., Carmichael G.R., Zhang Y., Lelieveld J. and Crutzen P.J.: Role of mineral aerosol as a reactive surface in the global troposphere, J. Geophys. Res., 101, 22,869-22,889, 1996.

Dentener F., Kinne S., Bond T., Boucher O., Cofala J., Generoso S., Ginoux P., Gong S., Hoelzemann J., Ito A., Marelli L., Penner J., Putaud J.-P., Textor C., Schulz M., Werf G.v.d. and Wilson J.: Emissions of primary aerosol and precursor gases in the years 2000 and 1750 -prescribed data-sets for AeroCom, Atmos. Chem. Phys., 6, 4321-4344, 2006.

Dong B. and Valdes P.J.: Simulations of the Last Glacial Maximum climates using a general circulation model: prescribed versus computed sea surface temperatures, Clymate Dynamics, 14(7-8), 571-591, 1998.

Edwards R., Sedwick P. N., Morgan V., Boutron C. F. and Hong S.: Iron in ice cores from Law Dome, East Antarctica: implications for past deposition of aerosol iron, Ann. Glaciol, 27, 365370, 1998.

Eidenshink, J.C. and Faundeen, J.L.: The 1 km AVHRR global land data set: first stages in implementation, Int. J. Remote Sensing , 15 (17), 3443-3462, 1994.

EPICA Community Members, One-to-one coupling of glacial climate variability in Greenland and Antarctica, Nature, 444, 195-198, 2006.

Fischer H., Siggaard-Andersen M.-L., Ruth U., Rthlisberger R. and Wolff E.: Glacial/interglacial changes in mineral dust and sea-salt records in polar ice cores: sources, transport, and deposition, Rewiews of Geophys., RG1002, 2007.

Gaiero D.M., Probst J.-L., Depetris P. J., Bidart S.M., and Leleyter L.: Iron and other transition metals in Patagonian riverborne and windborne materials: Geochemical control and transport to the southern South Atlantic Ocean, Geochimica et Cosmochimica Acta, 67 (19), 3603-3623, 2003.

Gallagher M.W., Nemitz E., Dorsey J.R., Fowler D., Sutton M.A. and J. Duyzer M.F.: Measurements and parameterizations of small aerosol deposition velocities to grassland, arable crops, and forest: Influence of surface roughness length on deposition, J. Geophys. Res., 107, 4154, doi:10.1029/2001JD000817, 2002.

Ganzeveld L. and Lelieveld J.: Dry deposition parameterization in a chemistry general circulation model and its influence on the distribution of reactive trace gases, J. Geophys. Res., 100, 20999-21012, 1995.

Ganzeveld L., Lelieveld J. and Roefols G.-J. : Dry deposition parameterization of sulfide oxides in a chemistry and general circulation model, J. Geophys. Res., 103, 5679-5694, 1998.

Gasso S., Stein A., Marino F., Castellano E., Udisti R. and Ceratto J.: A combined observational and modeling approach to study modern dust transport from Patagonia desert to East Antarctica, Atmos. Chem. Phys., 10, 8287-8303, 2010.

Ginoux P., Chin M., Tegen I., Prospero J. M., Holben B., Dubovik O. and Lin S.-J.: Sources and distributions of dust aerosols simulated with the GOCART model, J. Geoph. Res. 106, D17, 20,255-20,273, 2001.

Glser G., Kerkweg A. and Wernli H.: The mineral dust cycle in EMAC 2.40: sensitivity to the spectral resolution and the dust emission scheme, Atmos. Chem. Phys., 12, 1611-1627, 2012.

Greeley R. and Iversen J.D.: Wind as a Geological Process on Earth, Mars, Venus and Titan, 333 pp., Cambridge University Press, New York, 1985.

Hagemann S., Botzet M., Dmenil L. and Machenhauer B.: Derivation of global GCM boundary conditions from 1 km land use satellite data, MPI report No.289, 1999.

Harrison S.P., Kohfeld K.E., Roelandt C., Claquin T.: The role of dust in climate changes today, at the last glacial maximum and in the future, Earth-Science Reviews, 54, 43-80, 2001.

Hovan S.A., Rea D.K. and Pisias N.G.: Late Pleistocene continental climate and oceanic variability recorded in Northwest Pacific sediments, Paleoceanography, 6, 349-370, 1991.

Hummelshoj P., Jensen N.O. and Larsen S.E.: Particle dry deposition to a sea surface, pp. 829-840, Precipitation scavenging and atmosphere-surface exchange, Hemisphere Publishing Corporation, Washington, 1992.

Huneeus et al.: Global dust model intercomparison in AeroCom phase 1, Atmos. Chem. Phys., 11, 7781-7816, 2011.

Iglesias A.N.: Wind erosion,desertification and productivity crisis in the livestock economy of Patagonia: The case of the province of Santa Cruz, Estud. Geograf., 53, 4470-4479, 1992.

Imbrie J., Hays J.D., Martinson D.G., McIntyre A., Mix A.C., Morley J.J., Pisias N.G., Prell W.L. and Shackleton N.J. : The orbital theory of Pleistocene climate: support from a revised chronology of the marine δ^18O record, in Milankovitch and Climate, Part 1, edited by A. Berger et al., pp. 269-305, D. Reidel, Norwell, Mass., 1984.

Jickells T.D., An Z.S., Andersen K.K., Baker A.R., Bergametti G. et al.: Global iron connections between desert dust, ocean biogeochemistry, and climate, Science 308 (67), doi:10.1126/science.1105959.

Joussaume S., Taylor K.E., Braconnot P., Mitchell J.F.B., Kutzbach J.E., Harrison S.P. et al.: Monsoon changes for 6000 years ago: Results of 18 simulations from the Paleoclimate Modeling Intercomparison Project (PMIP), Geophys. Res. Letters, 26(7), 859-862, 1999.

Kawahata H.: Shifts in oceanic and atmospheric boundaries in the Tasman Sea (Southwest Pasific) during the Late Pleistocene: evidence from organic carbon and lithogenic fluxes, Palaeogeography, 184, 225-249, 2002.

Knorr W.: Satellitengestützte Fernerkundung and Modellierung des globalen CO_2-Austauschs der Landvegetation: Eine Synthese, Examensarbeit 49, Max-Planck-Institute for Meteorology, Hamburg, Germany, 1997.

Knorr W.: Constraining a global mechanistic vegetation model with satellite data, IEEE International Geoscience and Remote Sensing Symposium, Seattle, WA, 1998.

Knorr W. and Heimann M.: Impact of drought stress and other factors on seasonal land biosphere CO2 exchange studied through an atmosperic tracer transport model, Tellus, Ser. B., 47, 471-489, 1995.

Kohfeld K.E. and Harrison S.P., DIRTMAP: the geological record of dust, Earth Sci. Rev., 54, 81 114, 2001

Kohfeld K.E. and Tegen I.: Record of mineral aerosol and their role in the earth system, Treatise Geochem. 4, 1-26, 2007.

Krinner G. and Genthon C.: Tropospheric transport of the continental tracers towards Antarctica under varying climatic conditions, Tellus, 55B, 54-70, 2003.

Krinner G., Petit J.-R., Delmonte B.: Altitude of atmospheric tracer transport towards Antarctica in present and glacial climate, Quaternary Science Reviews, 29, 274-284, 2010.

Lambert F., Delmonte B., Petit J.R., Bigler M., Kaufmann P.R., Hutterli M.A., Stocker T.F., Ruth U., Steffensen J.P. and Maggi V.: Dust - climate couplings over the past 800,000 years from the EPICA Dome C ice core, Letters, 452, 616-619, 2008.

Legrand M. and Mayewski, P.: Glaciochemistry of polar ice cores: a review, Rewiews of Geophys., 35, 3, 219-243, 1997.

Li F., Ginoux P., Ramaswamy V.: Distribution, transport, and deposition of mineral dust in the Southern Ocean and Antarctica: Contribution of major sources, J. Geoph. Res., 113, D10207, 2008.

Li F., Ramaswamy V., Ginoux P., Broccoli A.J., Delworth T. and Zeng F.: Toward understanding the dust deposition in Antarctica during the Last Glacial Maximum: Sensitivity studies on plausible causes, J. Geoph. Res., 115, 2010.

Lin S.-J. and Rood R.B.: Multidimensional flux-form semi-Lagrangian transport schemes, Mon. Wea. Rev., 124, 2046-2068, 1996.

Lunt D.J. and Valdes P.J.: Dust transport to Dome C, Antarctica, at the Last Glacial Maximum and present day, Geoph. Res. Letters, 28 (2), 295-298, 2001.

Maher B.A., Prospero J.M., Mackie D., Gaiero D., Hesse P.P., Balkanski Y.: Global connections between aeolian dust, climate and ocean biogeochemistry at the present day and at the last glacial maximum, Earth-Science Reviews 99, 61-97, 2010.

Mahowald N., Kohfeld K., Hansson M., Balkanski Y., Harrison S.P., Prentice I.C., Schulz M., and Rodhe H.: Dust soutces and deposition during the last glacial maximum and current climate: A comparison of model results with paleodata from ice cores and marine sediments, J. Geophys. Res.-Atmos., 104(D13), 15895-15916, 1999.

Mahowald N., Muhs D.R., Levis S., Rasch P.J., Yoshioka M., Zender C.S. and Luo C.: Change in atmospheric mineral aerosols in response to climate: Last glacial period, preindustrial, modern, and doubled carbon dioxide climates, J. Geophis. Res., 111, D10202, 2006.

Mahowald N.M., Jickells T.D., Baker A.R., Artaxo P., Benitez-Nelson C. et al.: Global distribution of atmospheric phosphorus sources, concentration and deposition rates, and anthropogenic impacts, Global Biogeochemical Cycles 22:GB4026, doi:10.1029/2008GB003240, 2008.

Mahowald N., Engelstaedter S., Luo C., Sealy A., Artaxo P., Benitez-Nelson C., Bonnet S., Chen Y., Chuang P.Y., Cohen D.D., Dulac F., Herut B., Johansen A.M., Kubilay N., Losno R., Maenhaut W., Paytan A., Prospero J.M., Shank L.M. and Siefert R.L.: Atmospheric Iron Deposition: Global Distribution, Variability, and Human Perturbations, Annu. Rev. Marine. Sci, 1:245-278, 2009.

Mahowald N., Ward D.S., Kloster S., Flanner M.G., Heald C.L., Heavens N.G., Hess P.G., Lamarque J.-F., Chuang P.Y.: Aerosol Impact on Climate and Biogeochemistry, Annu. Rev. Environ. Resourc., 45-74, 2011.

Marticorena B. and Bergametti G.: Modeling the atmospheric dust cycle: 1. Design of a soil-derived dust emission scheme, J. Geophys. Res., 100(D8), 16,415-16,430, 1995.

Martin J.H., Gordon R.M. and Fitzwater S.E.: Iron in Antarctic waters, Nature, 353(6340):123.

McConnell J.R., Aristarain A.J., Banta J.R., Edwards P.R., Simes J.C.: 20th-Century doubling in dust archived in an Antarctic Peninsula ice core parallels climate change and desertification in South America, PNAS 104(14), 5743-5748, 2007.

McGee D., Marcantonio F., Lynch-Stieglitz J.: Deglacial changes in dust flux in the eastern equatorial Pacific, Earth and Planetary Science Letters, 257, 215-230, 2007.

Noriki S. and Tsunogai S.: Particulate fluxes and major components of settling particles from sediment trap experiments in the Pacific Ocean, Deep Sea Res., Part A, 33, 903-912, 1986.

Okin G., Mahowald N., Chadwick O. and Artaxo P.: The impact of desert dust on the biogeochemistry of phosphorus in terrestrial ecosystems, Global Biogeochem. Cycles, 18, GB2005, doi:10.1029/2003GB002145, 2004.

Otto-Bliesner B.L. and Brady E.C.: Last Glacial Maximum and Holocene Climate in CCSM3, J. Climate, 19, 2526-2544, 2005.

Parish T.R. and Cassano J.J.: The role of katabatic winds on the Antarctic surface wind regime, American Meteorological Society, 317-333, 2003.

Parish T.R. and Bromwich D.H.: Reexamination of the near-surface airflow over the Antarctic continent and implications on atmospheric circulations at high southern latitudes, American Meteorological Society, 1961-1973, 2007.

Peltier W.R.: Global glacial isostasy and the surface of the ice-age Earth: the ICE-5G (VM2) model and GRACE, Annu. Rev. Earth Planet. Sci., 32, 111149, 2004.

Petit J.R., Mounier L., Jouzel J., Korotkevich Y.S., Kotlyakov V.I., Lorius C.:Paleoclimatological and chronological implications of the Vostok core dust record, Nature, 343, 56-58, 1990.

Petit J.R., Jouzel J., Raynaud D., Barkov N.I., Barnola J.M., Basile I., Bender M., Chappellz J., Davis M., Delaygue G., Delmotte M., Kotlyakov V.M., Legrand M., Lipenkov V.Y., Lorius C., Pepin L., Ritz C., Saltzman E. and Stievenard M.: Climate and atmospheric history of the past 420,000 years from the Vostok ice core, Antarctica, Nature, 399, 429-436, 1999.

Prospero J.M., Glaccum R.A., Nees R.T.: Atmosperic transport of soil dust from Africa to South America, Nature, 289, 570-572, 1981.

Prospero J.M., Ginoux P., Torres O., Nicholson S.E. and Gill T.E.: Environmental characterization of global sources of atmospheric soil dust identified with the Nimbus 7 Total Ozone Mapping Spectrometer (TOMS) absorbing aerosol product, Rev. Geophys., 40(1), 2(1-31), 2002

Rea D.K.: The paleoclimatic record provided by eolian deposition in the deep sea: The geologic history of wind, Rev. Geophys., 32, 159-195, 1994.

Roeckner E., Buml G., Bonaventura L., Brokopf R., Esch M., Giorgetta M., Hagemann S., Kirchner I., Kornblueh L., Manzini E., Rhodin A., Schlese U., Schulzweida U., Tompkins A.: The atmospheric general circulation model ECHAM5. Part 1: Model description, Report No. 349, Max Planck Institute for Meteorology, Hamburg, Germany (available at http://www.mpimet.mpg.de), 2003.

Ruddiman W.F.: Tropical Atlantic terrigenous fluxes since 25,000 yrs B.P., Mar. Geol., 136, 189-207, 1997.

Sassen K., DeMott P.J., Prospero J.M. and Poellot M.R.: Saharan dust storms and indirect aerosol effect on clouds: CRYSTAL-FACE results, Geophysical Reserch Letters, 30 (12), 2003.

Satio C., Noriki S. and Tsunogai S.: Particulate flux of AI, a component of land origin, in the western Pacific, Deep Sea Res., Part A, 39, 1315-1327, 1992.

Schwerdtfeger W.: Weather and Climate of the Antarctic, Developments in Atmospheric Science, 15, 1984.

Seinfeld J.H. and Pandis S.N.: Atmospheric chemistry and physics: from air pollution to climate change, Wiley-Interscience, 1998.

Shao Y., Raupach M.R. and Findlater P.A.: Effect of saltation bombardment on the entrainment of dust by wind, J. Geophys. Res., 98, 12,719-12,726, 1993.

Sirocko F., Sarnthein M., Lange H. and Erlenkeuser H.: Atmospheric summer circulation and coastal upwelling in the Arabian Sea during the Holocene and the Last Glaciation, Quat. Res., 36, 72-93, 1991.

Slinn W.G.N.: Atmosphere-surface exchange of particulate and gaseous pollutants, chap. Dry deposition and resuspension of aerosol particles- a new look at some old problems, pp. 1-40, U.S. DOE Tech. Info. Center, Oak Ridge, TN, USA, 1976.

Slinn S. A. and Slinn W.G.N.: Predictions for particle deposition on natural waters, Atmos. Environ., 14, 1013-1016, 1980.

Slinn W.G.N.: Predictions for particle deposition to vegetative canopies, Atmos. Environ., 16, 1785-1794, 1982.

Smith B., Prentice C. and Sykes M.T.: Representation of vegetation dynamics in the modelling of terrestrial ecosystems: comparing two contrasting approaches within European climate space, Global Ecology & Biogeography, 10, 621-637, 2001.

Sokolik I.N.,Toon O.B., Incorporation of mineralogical composition into models of the radiative properties of mineral aerosol from UV to IR wavelengths, J. Geophys. Res., 104, 9423-9444, 1999.

Sokolik I.N., Winker D.M., Bergametti G., Gillette D.A., Carmichael G., Kaufman Y.J., Gomes L., Schuetz L., and Penner J.E.: Introduction to special section: Outstanding problems in quantifying the radiative impacts of mineral dust, J. Geophys. Res.-Atmos., 106(D16), 1801518027, 2001.

Stier P., Feichter J., Kinne S., Kloster S., Vignati E., Wilson J., Ganzeveld L., Tegen I., Werner M., Balkanski Y., Schulz M., Boucher O., Minikin A., and Petzold A.: The aerosol-climate model ECHAM5-HAM, Atmos. Chem. Phys., 5, 11251156, 2005.

Stull R.B.: An introduction to boundary layer meteorology, Kluwer Academic Publishers, Dordrecht, The Netherlands, ISBN 90-277-2769-4, 1988

Tegen I., Lacis A. and Fung I.: The influence on climate forcing of mineral aerosols from disturbed soils, Nature, 380, 419-422.

Tegen I., Harrison S.P., Kohfeld K., and Prentice I.C.:Impact of vegetation and preferential source areas on global dust aerosol: Results from a model study, J. Geophys. Res.-Atmos., 107(D21),14(1-21), 2002.

Tegen I.: Modeling the mineral dust aerosol cycle in the climate system, Quaternary Sci. Rev. 22(1819), 18211834, 2003.

Textor C., Schulz M., Guibert S., Kinne S., Balkanski Y., Bauer S., Berntsen T., Berglen T., Boucher O., Chin M., Dentener F., Diehl T., Easter R., Feichter H., Fillmore D., Ghan S., Ginoux P., Gong S.,. Grini A., Hendricks J., Horowitz L., Huang P., Isaksen I., Iversen T., Kloster S., Koch D., Kirkevag A., Kristjansson J. E., Krol M., Lauer A., Lamarque J. F., Liu X., Montanaro V., Myhre G., Penner J., Pitari G., Reddy S., Seland ., Stier P., Takemura T., and Tie X.: Analysis and quantification of the diversities of aerosol life cycles within AeroCom, Atmos. Chem. Phys, 6, 1777-1813, 2006.

Textor C., Schulz M., Guibert S., Kinne S.: The effect of harmonized emissions on aerosol properties in global models - an AeroCom experiment, Atmos. Chem. Phys. 7, 4489-4501, 2007.

Verheggen B., Cozic J., Weingartner E., Bower K., Mertes S., Connolly P., Gallagher M., Flynn M., Choularton T. and Baltensperger U.: Aerosol partitioning between the interstitial and condensed phase in mixed-phase clouds, J. Geoph. Res, 112, 2007.

Watson A.J., Bakker D.C.E., Ridgwell A.J., Boyd P.W. and Law C.S.: Effect of iron supply on Southern Ocean CO2 uptake and implications for glacial atmospheric CO2, Nature, 407, 730-733.

Wefer G. and Fischer G.: Seasonal patterns of vertical particle flux in equatorial and coastal upwelling areas of the eastern Atlantic, Deep Sea Res., Part I, 40, 1613-1645, 1993.

Werner M., Tegen I., Harrison S.P., Kohfeld K.E., Prentice I.C., Balkanski Y., Rodhe H., Roelandt C.: Seasonal and interannual variability of the mineral dust cycle under present and glacial climate conditions, J. Geophys. Res.-Atmos., 107(D24), 2(1-19), 2002.

Wolff E.W., Hall J.S., Mulvaney R., Pasteur E.C., Wagenbach D., Legrand M.: Relationship between chemistry of air, fresh snow and firn cores for aerosol species in coastal Antarctica, J. Geophys. Res.-Atmos., 103(D9), 11,057-11,070, 1998.

Wolff E.W., Fischer H., Fundel F., Ruth U., Twarloh B. et al.: Southern Ocean sea-ice extent, productivity and iron flux over the past eight glacial cycles, Nature, 440 (23), doi:10.1038/nature04614.

Acknowledgements

I would like to acknowledge the people who have supported me throughout my PhD study.

My sincerest thanks go to my supervisors Dr. Uwe Mikolajewicz and Dr. Claudia Timmreck for the valuable scientific discussions, sharing their deep knowledge and their support. Whenever I needed help their doors were always open for me. I am especially grateful to Prof. Hartmut Grassl for the fruitful panel meetings, useful advise and for the interesting stories of his life experiences. I am grateful to my former advisers Johann Feichter and Kai Zhang for their encouragement and helping me to begin my journey. I would like to thank all my former Russian colleagues and especially Boris Belan, my former adviser who taught me and gave me essential support.

A special thanks to my project colleague, Anna Wegner who explained a lot to me about Antarctic dust records, told me about polar expedition experiences and provided me with the necessary observational data. Thank you Anna for sharing the responsibility especially in our project meetings. I also thank Guy Schurgers for providing my vegetation data, without which my study would have been very difficult.

I very much appreciate the help and the timely discussions with Dmitry Sein, Declan O'Donnell, and Irina Fast whenever I needed it. These people gave me very helpful ideas in the time when I "could not see the light at the end of the tunnel".

I am very thankful to my friends: Armelle Remedio who shared all the ups and downs, Seethala Chellappan and Evgenia Bazhenova for their help and support, Thomas Krismer (you are really lucky if he is your officemate), Rosina Grimm for her always positive mood, Julia Polkova and Norman, Swati Gehlot, Freja Vamborg, Swantje Preuschmann, Vadim and Natalia and to all my friends and colleagues whom I have not mentioned here, but also contributed a lot. I also appreciate the people who helped me with English language correction of my thesis.

A very special thanks to Antje Weitz and Cornelia Kampmann for their help in organizing my PhD life (especially the warm and excellent outings), for their ever-ready support, and care to make my PhD life bearable.

Above all, I am grateful to my husband Dmitry Vergeles, my parents and relatives for the unconditional support and love.

Finally, I thank God for the great opportunity in my life to study here at the Max Planck Institute for Meteorology, to live in beautiful Hamburg and to meet such wonderful and talented people. Our future depends on our dreams. And one of my dreams has come true.

With deep appreciation, yours Natalia Sudarchikova.

ISSN 1614-1199